

The Influence of Water-Rock Interaction on Trace Element Mobilization during Shale Gas Production

by

Wenjia Fan

A dissertation submitted in partial fulfillment
of the requirements for the degree of
Doctor of Philosophy
(Environmental Engineering)
in the University of Michigan
2018

Doctoral Committee:

Assistant Professor Brian Ellis, Co-Chair
Professor Kim Hayes, Co-Chair
Associate Professor Christian Lastoskie
Professor Youxue Zhang

Wenjia Fan

fwenjia@umich.edu

ORCID Id: 0000-0002-4130-3636

©Wenjia 2018

To
my husband, Ruidong and our families

ACKNOWLEDGMENTS

First, I would like to express my appreciation for my two advisors, Brian and Kim, who always convince me that at the end of the day only hard work and good science matters. Every time when I struggled with my research, they always provide helpful suggestions with great patience. Without the support from my advisors, I won't be able to successfully finish my dissertation work. I also would like to acknowledge my other committee members, Youxue and Christian. Christian was assigned to be my adviser when I first enrolled as a master's student in our program. He offered me valuable suggestions to help me positively accept and embrace the challenge when switching from a Chemical Engineering background to Environmental Engineering program. I still remember the first time attending Youxue's Thermodynamics and Kinetics class, EARTH 554, he asked whether I plan to just audit the class and called me as friend from north campus. Thanks for Youxue's great patience and help, all my struggles for the class turned to provide a window to my geology world.

Also, I would like to thank for my current and previous lab mates in our research group especially Anne, who shared discussion with me about solving experimental problems and modelling issues. I also want to thank my friend, Peng Ni, from Earth and Environmental Science for all the technical support about my silly geology questions. My acknowledge also goes to William Harrison from Michigan Basin Core Research Laboratory for providing my experiment shale samples, Philip Simpson from Phoenix Memorial Lab for helping with radium analysis using gamma-ray spectroscopy, Thomas Yavaraski for all the laboratory support, Hang Wen from Pennsylvania State University as my CrunchFlow modelling consultant, and all the faculty members, friends and fellow graduate students in CEE department who helped make it enjoyable to study and work here.

Last but not the least, I would like to demonstrate my deepest gratefulness for my families. Thanks to my parents for offering financial help to support my master study in U.S. Also, I want to thank my grandmother for her deepest love and continuously feeding me with delicious food to help me survive through hard times. Thanks to my husband Ruidong for his love, tolerance, understanding, and accompany; all of which means everything to me.

Table of Contents

DEDICATION	ii
ACKNOWLEDGMENTS	iii
LIST OF TABLES	vii
LIST OF FIGURES	ix
LIST OF APPENDICES	xiv
ABSTRACT	xvi

CHAPTER:

1. Introduction	1
1.1 Background and motivation	1
1.1.1 Unconventional shale gas production	1
1.1.2 Environmental impacts	2
1.1.3 Research motivation	4
1.2 Research questions	7
1.3 Chapter summaries	8
1.4 References	12
2. Role of Water-Rock Interactions in Controlling Shale Gas Produced Brine Composition	20
2.1 Introduction	20
2.2 Materials and methods	22
2.2.1 Shale samples	22
2.2.2 Acid digestions and sequential extraction experiments	23
2.2.3 Batch experiments	24
2.2.4 Flowback water sampling	25
2.2.5 Chemical analysis	26
2.3 Results and discussion	26
2.3.1 Acid digestion and sequential extraction	27
2.3.2 Influence of in situ T, P, and shale mineralogy on element mobilization	29
2.3.3 Influence of HF fluids on element mobilization	31
2.3.3.1 pH as a key factor for trace element mobilization	32
2.3.3.2 Carbonates as a source of pH buffering and trace element release	33
2.3.3.3 Influence of redox potential on pyrite dissolution	33
2.3.4 Comparison of flowback water with batch experiments results	35
2.3.5 Environmental implication	38
3.4 References	40
3. Impact of Carbonate Dissolution on Arsenic Release during Shale Gas Extraction	45
3.1 Introduction	45
3.2 Materials and methods	48
3.2.1 Shale sample and injected hydraulic fracturing fluid	48

3.2.2	Flow-through experimental setup	48
3.2.3	2D reactive transport modeling.....	50
3.3	Results and discussion	57
3.3.1	Flow-through experiment effluent chemistry	59
3.3.2	Image analysis results	60
3.3.3	CrunchFlow reactive transport model calibration.....	61
3.3.4	Model results and discussion	63
3.3.5	Model sensitivity analysis	71
3.4	Conclusion	79
3.5	References.....	81
4.	Estimating Radium Activity in Shale Gas Produced Brine	85
4.1	Introduction.....	85
4.2	Materials and methods	89
4.2.1	Shale samples.....	89
4.2.2	Flowback and produced water samples	90
4.2.3	Shale digestion and chemical analyses	90
4.2.4	Ba adsorption/desorption experiments.....	91
4.3	Results and discussion	92
4.3.1	Validating U, Th estimates from spectral gamma-ray well logs	92
4.3.2	Rapid analysis of Ra activity via ICP-MS	93
4.3.3	Ra activity in produced brine.....	95
4.3.3.1	Influence of shale cation exchange capacity	97
4.3.3.2	Influence of formation water salinity.....	99
4.3.3.3	Influence of sulfate	102
4.4	Environmental implications	103
4.5	References.....	105
5.	Concluding Remarks	111
	Appendices.....	115

LIST OF TABLES

Table	Page
2.1 Shale composition as determined by X-ray diffraction	23
2.2 Hydraulic fracturing fluid chemical additives examined in this study	25
3.1 CrunchFlow model parameters	53
3.2: Summary of pyrite mineral surface area	65
3.3: Ranges of Da_I , Da_{II} , and Pe numbers in layers i and ii for calcite and pyrite	67
A2-1 Extraction percentages of sequential extraction results	117
A3-1 Batch experiments conducted in this study	118
A5-1 Reactions and equilibrium constants of mineral dissolution reaction	121
A5-2 Parameters used in equilibrium constant calculation.....	121
A7-1 Buffering capacity	123
A9-1 Input water chemistry	125
A9-2 Model simulation parameters	127
A11-1 Flowback water characterization	131
A12-1 Radium level estimation	132
B1: Averaged Da for pyrite in layer ii	149
C1: Estimation of rock: water ratio for three shale formations	152
C2: Errors of the uranium and thorium content from the Antrim formation	154
C3: XRD results of four shale samples used in this study.....	160
C4: Calculated CEC results	161
C5: Measured and reported U, Th, and Ba contents, and total organic content for shales	161

C6: Antrim produced water analysis..... 162

LIST OF FIGURES

Figure	Page
1.1 Map of Utica-Collingwood formation and the producing trend of the Antrim shale	7
2.1 Sequential extraction percentages results of different elements (U, Ba, Sr, As, Fe, Ca, K, Mg, Na) for three shale samples (Collingwood, Utica, Antrim)	28
2.2 Leaching of calcium from a Utica-Collingwood 1:1 mixture in contact with DI water (open symbols) and the model hydraulic fracturing fluid chemical mixture (full composition shown in Table 2.2) (closed symbols. Three different T, P conditions were investigated: 25°C, 1 atm (circle); 34°C, 100 atm (triangle); 43°C, 150 atm (square)	31
2.3 pH evolution (a) and extraction percentages (U/U_{total}) of uranium (b) from Utica, Collingwood and Antrim shale after contact with model HF fluids (full composition shown in Table 2) at 1.0 km T, P conditions and a rock–water ratio of 10 g/L	32
2.4 Arsenic (solid symbols) and Iron (open symbols) leaching profile of Antrim in contact with different chemical additives	34
2.5 Evolution of barium, sulfate, and radium concentration in flowback water sample.	36
3.1 Simplified schematic of flow-through experimental setup	50
3.2 Reactive transport model domain	51
3.3 Effluent pH, calcium, iron and arsenic concentration as a function of time for flow-through experiment CW#2. Red, blue, and green symbols represent experimental data for flowrates of 10 ml/hr, 5 ml/hr, and 2.5 ml/hr, respectively	57

3.4 Combined XCT (a) and SEM image analysis (b1 and b2) of dissolving fracture pathway cross section. Energy dispersive spectroscopy was used for element mapping	60
3.5 Altered layer formation schematics: a) Initial domain condition with no altered layers at 0 hr. b) Final domain condition with altered layers adjacent to flow path at 100 hr. The blue area indicates the fracture channel, while grey circles represent calcite and orange circles represent pyrite. Blue arrows symbolize fluid flow through the domain. c) Thickness of altered layer <i>i</i> and layer <i>ii</i> as a function of time.....	64
3.6 Averaged Péclet number of cells inside altered layer <i>i</i> and <i>ii</i>	66
3.7 (a). Damköhler numbers for pyrite dissolution in altered layer <i>i</i> and layer <i>ii</i> ; (b) Damköhler number for calcite dissolution in altered layer <i>i</i>	67
3.8 Surface-controlled reaction rate constant k_{surf} and diffusion-controlled reaction rate constant k_{diff} for calcite dissolution at 500 hr	68
3.9 Model effluent pH and Ca, Fe and As concentration as a function of time at a flowrate of 10 ml/hr.....	70
3.10 Model results (effluent pH, calcium, iron and arsenic concentrations) at a flowrate of 10 mL/hr and variable calcite content (5%, 10%, 15%, 30%, 60%)	72
3.11 Model averaged Péclet number of cells inside altered layers <i>i</i> and <i>ii</i> at variable calcite content: a) 5%, b) 30%, c) 60%	73
3.12 Thickness of altered layers <i>i</i> and <i>ii</i> as a function of time at variable calcite content (5%, 30%, 60%)	75
3.13 Model results of effluent arsenic concentration at a flowrate of 10 mL/hr and variable pyrite content (1%, 2%, 3%).....	76
3.14 Model results (of effluent pH, and calcium, iron and arsenic concentrations) at a flowrate of 10 mL/hr and variable injected fluids pH (1.9, 3, 4, 5, 6).....	77

3.15 Model results (effluent pH, calcium, iron and arsenic concentration) at variable flowrate (10 mL/hr, 5 mL/hr, 2.5 mL/hr)	78
3.16 Averaged Péclet number of cells inside altered layers <i>i</i> and <i>ii</i> at two different flowrates (2.5 mL/hr, 10 mL/hr)	79
4.1 Ra-226 activity in Collingwood (a) and Antrim (b) produced water measured by ICP-MS and HPGe-GS. Error bars represent standard deviation of three measurements	94
4.2 Predicted Ra-226 activity as a function of potential total Ra present in the shale for a given shale U content. Symbols represent produced water sample data from the Utica-Collingwood (triangle), Antrim (diamond), and Marcellus (square).....	96
4.3 Estimated shale cation exchange capacity based on Ba adsorption titration	99
4.4 Ba desorbed from four different shales as a function of increasing NaCl concentration.	100
4.5 Correlation of Ra-226 activity with TDS for produced water samples from the (a) Antrim, (b) Collingwood, and (c) Marcellus formations	101
A4-1 Scanning electron micrograph and selective elemental maps of Utica thin sections ...	119
A4-2 Scanning electron micrograph and selective elemental maps of Collingwood thin sections.....	120
A4-3 Scanning electron micrograph of Antrim powder sample and Energy dispersive X-ray spectroscopy (EDS) spectrum of pyrite grain	120
A6 Extraction percentages (Me/Me_{total}) of Ba, Fe, Mg, As from Utica, Collingwood and Antrim shale after contact with synthetic HF fluids (composition shown in Table 2) at 1.0 km T, P conditions and a rock: water ratio of 10 g/L	122
A8-1 Eh profile for Utica-Collingwood mixtures experiments	124
A8-2 Eh profile for Antrim experiments	124
A8-3 pH profile for Utica-Collingwood mixtures experiments.....	124

A8-4 pH profile for Antrim experiments	124
A9-1 Fe stability diagram for Antrim 1.0 km HF fluids.....	125
A9-2 Scanning electron micrograph of pyrite framboids in Antrim powder samples.....	126
A9-3 Comparison of [Fe ²⁺] in batch experiment vs simulation.....	127
A9-4 Pyrite dissolution	128
A9-5 Carbonate dissolution	128
A9-6 Fe speciation diagram.....	128
A9-7 Simulated [Fe ²⁺] under different surface areas	128
A9-8 Simulated [Fe ²⁺] assuming different initial pyrite amount	129
A10-1 [As] vs. [Fe] for Antrim in contact with acid solution (Acid only) and all four chemical additives solutions (HF fluids)	130
B1 Sequential extraction results for proportioning of elements between exchangeable sites, water-soluble, carbonate and sulfide or organic phases for Collingwood	134
B2 Averaged mineral fraction results	135
B3 Core intersection (1) images and close-up of pyrite grains	136
B4 SEM images and EDS results in core fracture section (1).....	136
B5 SEM images of core section (2)	137
B6 Formation of an altered layer (L)	138
B7 CW#1 experimental results	139
B8 Effluent pH, and calcium, iron and arsenic concentrations and modeling results as a function of time for the two flow-through experiments. Black points are experimental results from CW#1 at 2.5 ml/hr. Blue, orange, and green dots represent experimental data from CW#2 at 10 ml/hr, 5 ml/hr, and 2.5 ml/hr, respectively	140
B9 Pe number for individual grid	142
B10 Da number for individual grid.....	145

B11 Model results (mineral saturation index, mineral volume, pH, and porosity) at 500 hr	147
B12 Model Damköhler numbers for calcite dissolution at variable calcite content (5%, 30%, 60%) in altered layer <i>i</i> at 500 hr simulation time.....	148
B13 Model results of penetration depth of altered layers <i>i</i> and <i>ii</i> into core.....	148
B14 Reconstruction of the XCT scan before and after experiment CW#1.....	150
C1 Predicted Ra-226 activity vs. U content for different rock/water ratios for field sample data from three formations.....	153
C2 Average calibration curve for Ra at 100 g/L Cl ⁻	155
C3 Ra-226 and total Ra activity in 11 Collingwood flowback water samples measured by HP-Ge gamma spectroscopy	155
C4 Decay chains of U-238 and Th-232	158
C5 Ra-228/Ra-226 activity ratio of Collingwood flowback and Antrim produced waters ...	159
C6 Ra-226 activity vs. TDS for Antrim produced water samples	163

LIST OF APPENDICES

Appendix	Page
A. Supplemental data and figures for Chapter 2.....	115
A-1. Estimation of rock: water ratio	115
A-2. Procedure and results of sequential extraction	116
A-3. Batch experiment list	118
A-4. Images of presence of pyrite framboid in three shale samples	119
A-5. Adjusted equilibrium constants at different P and T	121
A-6. Extraction percentages of Ba, Fe, Mg, As	122
A-7. Buffering capacity of shale	123
A-8. Eh and pH profiles	124
A-9. Pyrite dissolution discussion.....	125
A-10. As vs. Fe correlation	130
A-11. Flowback water.....	131
A-12. Ra estimation for batch experiments	132
Reference	133
B. Supplemental data and figures for Chapter 3	134
B-1. Sequential extraction results of Collingwood	134
B-2. Core characterization	135
B-3. Effluent pH, and Ca, Fe, and As concentration profiles for CW#1	139
B-4. Model calibration results.....	140

B-5. Pe number	141
B-6. Da number.....	143
B-7. Model results under a flowrate of 10 ml/hr at 500 hr	146
B-8. Model results for different calcite content	148
B-9. Model results for different pyrite content	149
B-10. Heterogeneity and fractures	150
C. Supplemental data and figures for Chapter 4	151
C-1. Well logging information and rock/ water ratio estimation.....	151
C-2. Comparison of spectral gamma-ray well logs and extraction digestion data for U and Th content	154
C-3. Ra measurements	155
C-4. Secular equilibrium theory.....	156
C-5. Shale XRD analysis results	160
C-6. Antrim produced water analysis	162
Reference	164

ABSTRACT

The extraction of natural gas from shale reservoirs has generated a substantial increase in the volume of produced brine. In addition to being highly saline, these brines often contain elevated concentrations of naturally-occurring radionuclides and toxic metals. These characteristics present many challenges with regard to effective treatment and disposal. This dissertation investigated the mobilization of Ba, As, U, and Ra from shale in contact with hydraulic fracturing fluids under typical reservoir pressure and temperature conditions through a series of batch and flow-through experiments as well as geochemical simulations. Comparison of experimental data with flowback samples collected from a shale gas well in Michigan demonstrated that a majority of toxic elements present in production wastewaters likely originate from connate brines and are not substantially enhanced by well completion activities. X-ray computed tomography and scanning electron microscopy analysis demonstrated the co-occurrence of calcite-depleted regions and exposed pyrite at the fracture face in the core-flooding experiments. Following this observation, a 2D reactive transport model was developed to further study the effect of fast calcite depletion on pyrite dissolution and associated arsenic leaching. The relative importance of advection, diffusion, and reaction rate in controlling mineral dissolution was evaluated through analysis of model domain Péclet (Pe) and Damköhler (Da) numbers. Calcite dissolution was shown to be mass transport rate limited, while the dissolution of pyrite embedded within the calcite-depleted shale matrix was controlled by a combination of surface reaction and mass transport. Additionally, the mechanism and controls for Ra mobilization in produced brines were investigated and used to develop an empirical relationship for predicting Ra activity in shale gas wastewaters. It was

shown that adsorption/desorption is the primary process controlling Ra mobilization. Ra activity can be estimated prior to drilling activity if the U and Th content of the shale and the TDS of produced water is known. This knowledge can be used to guide optimal wastewater treatment and disposal strategies prior to any drilling activity, thereby reducing hazards associated with elevated Ra activity in shale gas wastewaters.

Chapter 1

Introduction

1.1 Background and motivation

1.1.1 Unconventional shale gas production

A reliable supply of natural gas along with its high energy content have led energy developers to pursue natural gas as an energy source.¹ Natural gas is well known as an efficient, bridge energy source between existing carbon-intensive fuels, like coal, and future renewable energy sources because it emits less carbon dioxide (CO₂) than coal for equivalent amounts of power generation.² In addition, the switch from coal to natural gas for power generation can largely reduce sulfur, nitrogen, mercury, and particulate air pollution.³ A study by Chen et al. found that the human toxicity impact of electricity produced from shale gas is much lower than from coal.⁴ In early 2018, the U.S. Energy Information Administration (EIA) predicted natural gas will remain the primary energy source for electricity generation, partially due to the relatively low cost of natural gas.⁵

Increased natural gas production in U.S. is the result of continued development of shale gas, which is expected to account for more than three-quarters of natural gas production by 2050.⁶ Unlike conventional reservoirs that have sufficient permeability to pump gas resources through vertical drilling, unconventional reservoirs have low permeability and must be stimulated via hydraulic fracturing to generate flow pathways and increase surface area prior to production. In 2016, hydraulically fractured horizontal wells accounted for 69% of all oil and natural gas wells drilled in the United States and 83% of the total linear footage

drilled.⁷

Because they are longer, and the drilling process is more complex, a horizontal well is generally more expensive to drill than a vertical well.⁷ The combination of horizontal drilling and hydraulic fracturing has made the production of shale gas economically viable, which resulted in substantial growth in U.S. natural gas production through the early 2000s and has generated global interest in developing shale gas reservoirs.⁸

1.1.2 Environmental impacts

Different environmental impacts associated with unconventional shale gas development. Unconventional wells are typically drilled up to 3 km of depth and the length of the horizontal section (lateral) can range from less than a hundred meters to several kilometers, targeting formations as thin as 30 m thick.³ This process can generate about 1,000 tons of drill cuttings depending on the depth of the formation and the length of the horizontal tail.⁹ Also, during the hydraulic fracturing process, a significant amount of water-based hydraulic fracturing (HF) fluids are pumped at high pressure into the reservoir to initiate fractures and subsequently release the entrapped natural gas. Each production usually consumes 8,000 to 80,000 m³ (2-20 million gallons) water³ which, though substantial, is far less than the amount of water used in agriculture, manufacturing, and municipal water supply.¹⁰ Water footprint analysis has shown that the hydraulic fracturing revolution has increased overall water usage and wastewater production in the United States, but the consumed and produced water intensities of hydraulic fracturing are still lower than other energy extraction methods and represent only a fraction of total industrial water use nationwide.¹¹ The specific water quantity needed to fracture a well depends on the formation basin, recoverable amount of gas, and the number of fracture stages.¹² Risk associated with these large amount of water withdrawal in a short period can be large in particular place and particular time. Furthermore, this part of water

can also be obtained from recycled production brines other than on-site water wells, municipal water resources, and surface waters. In most locations, the water quantity is then not believed to be a significant issue.

In addition to water, a range of chemicals are added to synthesize HF fluids in order to enhance the hydraulic fracturing process as well as shale gas production. The chemicals contain proppant (hold fractures open for releasing gas), friction reducer (reduce friction effect), surfactants (to increase recovery), scale inhibitors (prevent formation of calcium carbonate and calcium, barium, strontium sulfates), gelation chemicals (iron control), acid (aid in fracturing and dissolving the rock), biocide (control bacterial growth), and corrosion inhibitors.^{13,14} The specific chemical composition used to complete a given well depends on many site-specific factors. Although chemical recipes are still kept secret due to proprietary concerns, many operators are choosing to voluntarily disclose the chemical make-up of their completion fluids through the website Fracfocus.org, which now has chemical disclosures for over 127,781 hydraulically fractured wells completed in the U.S.

After the fracturing process, the wells are then sometimes shut-in to enhance hydrocarbon production. The injected HF fluid then returns to the surface as ‘flowback’ water prior to production of natural gas. The exact percentage of injected fluid that returns as flowback is quite variable and can depend on many factors such as the duration of well shut-in and the initial saturation state of the reservoir.¹⁵ Typical flowback volumes range from 9-53% of the total volume of HF fluid injected for Marcellus shale.¹⁶ The well will also produce water as produced water throughout its production lifetime.

The main wastes associated with this hydrocarbon extraction process consist of drill cuttings, flowback/produced water and other by-products associated with this process.¹⁷ Most drill cuttings (98.4%) are disposed of in landfills.¹⁷ Flowback and produced water are mostly either treated for reuse in another hydraulic fracturing job or disposed of in deep injection wells.

However, earthquakes have been linked directly to deep well injection disposal of produced waste water.¹⁸ Environmental issues include air quality impacts from emissions of greenhouse gases and ozone precursors (volatile organic compounds and nitrogen oxides), which have associated health effects that are difficult to quantify.¹⁹ Natural gas production actually emits less air particles compared to other fossil fuels.²⁰ The most contentious area is still risk that shale gas operations pose to water resources, such as the contamination of shallow aquifers by fugitive gas, or spilled HF fluids; disposal of inadequately treated shale gas wastewater; and drinking water contamination because of poor well integrity.^{1,3,16,21–27} There are also water quality concerns over the disinfection byproducts²⁸, biocides²⁹, bromide, iodide and ammonium³⁰ in shale gas wastewater, which might add special challenges to water treatment.

1.1.3 Research motivation

As the largest waste stream associated with shale gas production, flowback/produced water consists of the injected HF fluids and formation water that have been in close contact with reservoir rock and is therefore expected to contain elements both from the formation and introduced chemicals. The targeted organic-rich shales have generally been associated with low-level water contamination due to natural weathering processes, causing the release of trace metals to groundwater.^{31–35} In order to recognize specific contaminants of concern, the EPA has identified a list of target chemicals to monitor when assessing the adequacy of flowback water treatment. This list includes monitoring of As, Ra, Sr, Ba, and U, among other inorganic and organic components.³⁶ The flowback and produced waters that return to the surface during production are high in volatile organic compounds, total dissolved solids (TDS, 60,000–350,000 mg/L) and contain halides (e.g., chloride, bromide), strontium, barium, and often naturally occurring radioactive materials (NORMs) as well as organics.^{15,37–46} The wastewater may be recycled, treated, or disposed of through deep well injection. Several studies have

characterized flowback waters associated with unconventional reservoir drilling and field data shows that the water chemistry of flowback water is different from that of injected water.^{38,47–52} The specific chemical composition of flowback/produced water varies greatly and depends on geological conditions such as formation mineralogy, geographic location and depositional age of the reservoirs.⁵³

Although characterization of flowback water has been widely investigated, the source is still a matter of debate. The origin of the salts within the brine is important in understanding the total volume of saline fluid within the reservoir and its behavior over the life cycle of gas production.⁵⁴ It has been proposed high TDS in produced brines could have originated from subsurface dissolution of evaporates; the micro fracture matrix sequence of diagenesis of minerals inside formation rock;⁵⁴ the mixing between injected fracturing fluid and accessible mobile brine;^{49,55,56} or mobilization of immobile connate pore fluids held by capillarity.^{38,51} Considering differences in formation mineralogy and geological conditions, it is plausible that the salts originate from multiple sources.

One important area that has received limited attention is the contribution of water-rock interactions to flowback fluid chemistry. Several experimental and modeling studies have examined the influence of water-rock interaction.^{57–61} Dieterich et al.⁵⁷ demonstrated the *in situ* pressure can promote fracture growth and observed mineral dissolution/precipitation on shale surface when in contact with synthetic HF fluids. Phan et al.⁵⁸ studied the potential mobilization of trace metals in drilling cuts under certain storage and disposal conditions. Renock et al.⁵⁹ investigated the reductive weathering that release barium during hydraulic fracturing. Wang et al. varied the fluids properties including pH, oxidant level, and solid:water ratio to study the mobilization of elements (Ca, Mg, Fe, Ba, As, SO₄²⁻) from Eagle Ford shale. The pH was demonstrated to be the main controlling factor. A comprehensive study in the area of a more complete set of fracking fluid parameters on toxic element release is still needed. The ability

to predict the chemical evolution of remnant HF fluids or the chemistry of flowback water returning to the surface will be improved if the HF fluid-shale geochemical reactions occurring in the subsurface can be better characterized. In order to develop efficient and innovative treatment strategies for these emerging wastewater streams, a more complete understanding of their composition and the controlling factors that determine the chemical evolution of these waters is needed. Understanding the source of flowback/produced water and the factors controlling water chemistry is important for guiding hydraulic fracturing development and management.

To help address this knowledge gap, this study investigated the degree to which water-rock interactions between simulated HF fluids and fractured shales contribute to the impaired water quality observed in water that returns to the surface during shale gas production. In addition to analyzing samples of flowback/produced water and shale, both batch and flow-through experiments were applied to study the mobilization of trace metals and radionuclides from two shale gas reservoirs in the Michigan Basin: the Collingwood-Utica and Antrim formations (Figure 1.1). The Utica-Collingwood is an emerging shale gas reservoir in the northern half of Michigan's lower-peninsula. It is comprised of both the Utica shale and the organic-rich Collingwood limestone. The Antrim shale has been active since the 1980's, but drilling in this reservoir is on the decline. To further investigate the effects of different shale and chemicals as well as contact time on trace elements mobilization, geochemical simulations were performed in addition to experiments. The objectives of this research were to evaluate the potential mobilization mechanisms of different elements of interest during the water-rock interaction.

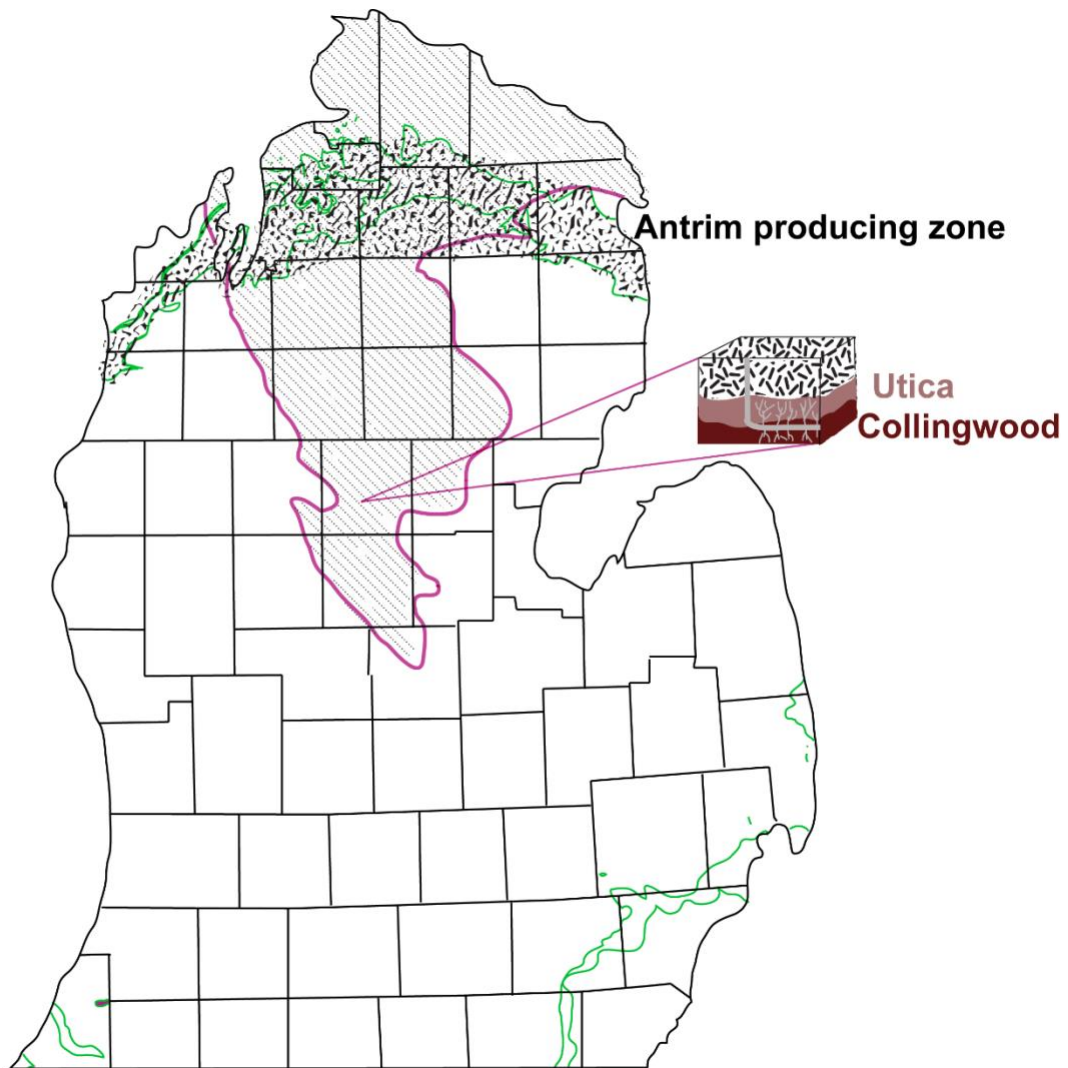


Figure 1.1: Map of Utica-Collingwood formation and the producing trend of the Antrim shale.

1.2 Research questions

The goal of this thesis is to build a comprehensive understanding of the factors controlling the trace metals and radionuclides (mainly U, As, Ba, Ra) leaching in shale gas produced brine. Formation heterogeneity has great influence on element mobilization and was investigated using scanning electron microscopy (SEM), x-ray computed tomography, x-ray diffraction (XRD), sequential extraction, hot acid digestion, and whole digestion. Through this thesis, the rate and extent of trace element and radionuclide leaching have been investigated

using two Michigan shale gas reservoirs in contact with synthetic HF fluids under ranges of system conditions (P, T, pe, pH) expected in the shale formations. Research questions addressed will include:

***R1.** Which elements are mobilized from shale through interactions between shale and HF fluids? Which shale phases control trace element leaching and mobility? How do the different chemical additives in HF fluids impact trace element mobilization? Among all chemical additives, which chemical has the largest effect?*

***R2.** How do the system conditions (P, T, pH, pe) affect trace element mobilization?*

***R3.** How do the chemical additives affect the trace metal leaching rate? How does different mineral accessibility affect the leaching rate?*

***R4.** How do experimental results compare with field samples? Do shale/HF fluid interactions measured in the laboratory leaching studies account for the trace element mobility observed in flowback/produced water?*

***R5.** What factors control radionuclide (mainly radium-226) mobilization and activity levels in produced brine?*

These research questions are addressed as described in Chapters 2-4 through a combination of bench-scale batch experiments, flow-through experiments, and geochemical modeling simulations.

1.3 Chapter Summaries

Chapter 2 presents the results of a series of *in situ* batch trace element leaching experiments of shale in contact with HF fluids, and by comparing these results to actual trace element concentrations in flowback water from field samples. This work was performed to evaluate the role of common HF chemical additives in promoting the mobilization of toxic

elements from two shale gas reservoirs in the Michigan Basin, which addresses research questions **R1**, **R2** and **R4** noted above. In addition to X-ray diffraction analysis, a sequential extraction approach is used to apportion the origin of elements among various mineral phases present in shale and to better understand the mechanisms promoting the release of these phases. Batch experiments were conducted over a range of coupled T/P conditions relevant to shale gas extraction depths and were focused on specific elements of interest including Ba, As, U, and Ra when powdered shale samples in contact with synthetic hydraulic fracturing fluids. In addition, batch geochemical modelling together with Eh-pH stability analysis were applied to better understand acid oxidative pyrite dissolution and the release of trace elements bounded to pyrite.

Chapter 3 addresses questions under R3 and demonstrates how carbonate dissolution influences As release from shale in contact with HF fluids through core flow-through experiments at different flowrates. As an organic-rich limestone, the Collingwood formation shale contains a small amount of pyrite. Batch experiments as well as sequential extraction results indicate that both Fe and As are mostly bound to reduced phases, possibly arseno-pyrite or arsenian-pyrite. Previous well-mixed batch reactor studies of powdered shale samples were implemented to maximize the accessibility of pyrite for As leaching compared to actual core samples. Two core flooding experiments where synthetic HF fluids flowed through proppant-packed fractured shale cores were also conducted under the same coupled T and P reservoir conditions (as described in the batch experiments of Chapter 2). Compared to batch studies of powdered shale samples, flowing HF fluids through a fractured core sample can reduce accessibility of As and minimize pH buffering provides less hydraulic contact time for the relatively fast carbonate and slower pyrite dissolution. A combination of X-ray computed tomography and SEM was applied to explain flow-through experimental observations. In addition, a 2D reactive transport model using CrunchFlow was included to study the

importance of mineral surface-controlled dissolution and transport-limited process for both calcite and pyrite dissolution, which better demonstrates As leaching mechanisms. Non-dimensional parameters including the Péclet number (Pe) and Damköhler numbers (Da) were applied to evaluate the relative importance of advection, diffusion, and reaction terms in controlling element leaching, in general, and particularly the impact of carbonate dissolution on As leaching from pyrite.

Chapter 4 develops an empirical approach to predict radium release in shale gas produced brines as a function of fluid solution conditions, which addresses Questions under **R5**. Even though measurable in flowback water per Chapter 2, Ra activity was below detection counts in all laboratory-scale batch and flow-through experiments under realistic water/rock ratios. Because of the short half-lives of 1600 yr and 5.75 yr for Ra-226 and Ra-228, respectively, the elevated Ra level in flowback/produced water has to come from continuous decay of parent radionuclides U-238 and Th-232, which are both naturally inherent to most organic-rich shales. Water/rock interactions must play an important role in the Ra mobilization process. This chapter presents an analysis of the role of shale composition (U, Th content and cation exchange capacity) and formation water composition (cation concentration and sulfate level) in influencing Ra activity in shale gas produced brines. Three different shale gas reservoirs were analyzed in this study, including the Antrim and Utica-Collingwood formation in Michigan and the Marcellus formation in Pennsylvania. Spectral gamma ray well logs and full mineral digestions together illustrate that spectral gamma ray well logs can be used to reasonably determine approximate U and Th concentrations within the shale in a given reservoir. The correspondent decay products of Ra isotopes in source rock can then be estimated. Two Ra measurements, inductively coupled plasma mass spectrometry (ICP-MS) and gamma-ray spectroscopy techniques, were compared. The rapid ICP-MS results were in agreement with gamma-ray spectroscopy for Antrim produced water samples with lower

salinity and higher Ra activity, but not for Collingwood flowback samples. Barium adsorption/desorption experiments were conducted to obtain shale cation exchange capacity (CEC). By correlating shale reservoir U content and TDS to the expected Ra activity in Antrim produced brines, an empirical equation could be obtained for Ra activity prediction. Based on this correlation, it may be possible to identify *a priori* if a given well from other shale formation may be expected to result in flowback water with high concentrations of Ra. By following the approach flowback water that is likely to have high Ra concentrations can be targeted for effective wastewater treatment processes and disposal strategies to better manage the risks associated with shale gas produced NORM.

Chapter 5 summarizes the conclusions of the work presented in this dissertation and discusses the impact of these findings.

1.4 References:

- (1) Kargbo, D. M.; Wilhelm, R. G.; Campbell, D. J. Natural Gas Plays in the Marcellus Shale: Challenges and Potential Opportunities. *Environ. Sci. Technol.* **2010**, *44* (15), 5679–5684.
- (2) Jaramillo, P.; Griffin, W. M.; Matthews, H. S. Comparative Life-Cycle Air Emissions of Coal, Domestic Natural Gas, LNG, and SNG for Electricity Generation. *Environ. Sci. Technol.* **2007**, *41* (17), 6290–6296.
- (3) Jackson, R. B.; Vengosh, A.; Carey, J. W.; Davies, R. J.; Darrah, T. H.; O’Sullivan, F.; Pétron, G. The Environmental Costs and Benefits of Fracking. *Annu. Rev. Environ. Resour.* **2014**, *39* (1), 327–362.
- (4) Chen, L.; Miller, S. A.; Ellis, B. R. Comparative Human Toxicity Impact of Electricity Produced from Shale Gas and Coal. *Environ. Sci. Technol.* **2017**, *51* (21), 13018–13027.
- (5) EIA forecasts natural gas to remain primary energy source for electricity generation - Today in Energy - U.S. Energy Information Administration (EIA)
<https://www.eia.gov/todayinenergy/detail.php?id=34612>.
- (6) EIA - Annual Energy Outlook 2018 <https://www.eia.gov/outlooks/aeo/>.
- (7) Hydraulically fractured horizontal wells account for most new oil and natural gas wells - Today in Energy - U.S. Energy Information Administration (EIA)
<https://www.eia.gov/todayinenergy/detail.php?id=34732>.
- (8) Daniel J. Soeder; William M. Kappel. *Water Resources and Natural Gas Production from the Marcellus Shale*; Geological Survey Fact Sheet 2009–3032; 2009.
- (9) Lampe, D. J.; Stolz, J. F. Current Perspectives on Unconventional Shale Gas Extraction in the Appalachian Basin. *J. Environ. Sci. Health Part A* **2015**, *50* (5), 434–446.
- (10) Hydraulic Fracturing Water Usage | FracFocus Chemical Disclosure Registry
<https://fracfocus.org/water-protection/hydraulic-fracturing-usage>.

- (11) Kondash, A.; Vengosh, A. Water Footprint of Hydraulic Fracturing. *Environ. Sci. Technol. Lett.* **2015**, 2 (10), 276–280.
- (12) *Modern Shale Gas Development in the United States: A Primer*; Ground Water Protection Council, 2009.
- (13) George E. King. *Hydraulic Fracturing 101: What Every Representative, Environmentalist, Regulator, Reporter, Investor, University Researcher, Neighbor and Engineer Should Know About Estimating Frac Risk and Improving Frac Performance in Unconventional Gas and Oil Wells*.
- (14) Johnson, B. M.; Kanagy, L. E.; Rodgers, J. H.; Castle, J. W. Chemical, Physical, and Risk Characterization of Natural Gas Storage Produced Waters. *Water. Air. Soil Pollut.* **2008**, 191 (1–4), 33–54.
- (15) Gregory, K. B.; Vidic, R. D.; Dzombak, D. A. Water Management Challenges Associated with the Production of Shale Gas by Hydraulic Fracturing. *Elements* **2011**, 7 (3), 181–186.
- (16) Vidic, R. D.; Brantley, S. L.; Vandenbossche, J. M.; Yoxtheimer, D.; Abad, J. D. Impact of Shale Gas Development on Regional Water Quality. *Science* **2013**, 340 (6134), 1235009.
- (17) Maloney, K. O.; Yoxtheimer, D. A. Production and Disposal of Waste Materials from Gas and Oil Extraction from the Marcellus Shale Play in Pennsylvania. *Environ. Pract.* **2012**, 14 (4), 10.
- (18) Elst, N. J. van der; Savage, H. M.; Keranen, K. M.; Abers, G. A. Enhanced Remote Earthquake Triggering at Fluid-Injection Sites in the Midwestern United States. *Science* **2013**, 341 (6142), 164–167.

- (19) Adgate, J. L.; Goldstein, B. D.; McKenzie, L. M. Potential Public Health Hazards, Exposures and Health Effects from Unconventional Natural Gas Development. *Environ. Sci. Technol.* **2014**, *48* (15), 8307–8320.
- (20) Moore, C. W.; Zielinska, B.; Pétron, G.; Jackson, R. B. Air Impacts of Increased Natural Gas Acquisition, Processing, and Use: A Critical Review. *Environ. Sci. Technol.* **2014**, *48* (15), 8349–8359.
- (21) Vengosh, A.; Jackson, R. B.; Warner, N.; Darrah, T. H.; Kondash, A. A Critical Review of the Risks to Water Resources from Unconventional Shale Gas Development and Hydraulic Fracturing in the United States. *Environ. Sci. Technol.* **2014**, *48* (15), 8334–8348.
- (22) Torres, L.; Yadav, O. P.; Khan, E. A Review on Risk Assessment Techniques for Hydraulic Fracturing Water and Produced Water Management Implemented in Onshore Unconventional Oil and Gas Production. *Sci. Total Environ.* **2016**, *539*, 478–493.
- (23) Olmstead, S. M.; Muehlenbachs, L. A.; Shih, J.-S.; Chu, Z.; Krupnick, A. J. Shale Gas Development Impacts on Surface Water Quality in Pennsylvania. *Proc. Natl. Acad. Sci.* **2013**, *110* (13), 4962–4967.
- (24) Jackson, R. e.; Gorody, A. w.; Mayer, B.; Roy, J. w.; Ryan, M. c.; Van Stempvoort, D. r. Groundwater Protection and Unconventional Gas Extraction: The Critical Need for Field-Based Hydrogeological Research. *Groundwater* **2013**, *51* (4), 488–510.
- (25) Brantley, S. L.; Yoxheimer, D.; Arjmand, S.; Grieve, P.; Vidic, R.; Pollak, J.; Llewellyn, G. T.; Abad, J.; Simon, C. Water Resource Impacts during Unconventional Shale Gas Development: The Pennsylvania Experience. *Int. J. Coal Geol.* **2014**, *126*, 140–156.

- (26) Warner, N. R.; Christie, C. A.; Jackson, R. B.; Vengosh, A. Impacts of Shale Gas Wastewater Disposal on Water Quality in Western Pennsylvania. *Environ. Sci. Technol.* **2013**, *47* (20), 11849–11857.
- (27) Warner, N. R.; Jackson, R. B.; Darrah, T. H.; Osborn, S. G.; Down, A.; Zhao, K.; White, A.; Vengosh, A. Geochemical Evidence for Possible Natural Migration of Marcellus Formation Brine to Shallow Aquifers in Pennsylvania. *Proc. Natl. Acad. Sci.* **2012**, *109* (30), 11961–11966.
- (28) Parker, K. M.; Zeng, T.; Harkness, J.; Vengosh, A.; Mitch, W. A. Enhanced Formation of Disinfection Byproducts in Shale Gas Wastewater-Impacted Drinking Water Supplies. *Environ. Sci. Technol.* **2014**, *48* (19), 11161–11169.
- (29) Kahrilas, G. A.; Blotevogel, J.; Stewart, P. S.; Borch, T. Biocides in Hydraulic Fracturing Fluids: A Critical Review of Their Usage, Mobility, Degradation, and Toxicity. *Environ. Sci. Technol.* **2014**, *49* (1), 16–32.
- (30) Harkness, J. S.; Dwyer, G. S.; Warner, N. R.; Parker, K. M.; Mitch, W. A.; Vengosh, A. Iodide, Bromide, and Ammonium in Hydraulic Fracturing and Oil and Gas Wastewaters: Environmental Implications. *Environ. Sci. Technol.* **2015**, *49* (3), 1955–1963.
- (31) Smedley, P. L.; Kinniburgh, D. G. A Review of the Source, Behaviour and Distribution of Arsenic in Natural Waters. *Appl. Geochem.* **2002**, *17* (5), 517–568.
- (32) Peng, B.; Song, Z.; Tu, X.; Xiao, M.; Wu, F.; Lv, H. Release of Heavy Metals during Weathering of the Lower Cambrian Black Shales in Western Hunan, China. *Environ. Geol.* **2004**, *45* (8), 1137–1147.
- (33) Woo, N. C.; Choi, M. J.; Lee, K. S. Assessment of Groundwater Quality and Contamination from Uranium-Bearing Black Shale in Goesan–Boeun Areas, Korea. *Environ. Geochem. Health* **24** (3), 264–273.

- (34) Loukola-Ruskeeniemi, K.; Kantola, M.; Halonen, T.; Seppänen, K.; Henttonen, P.; Kallio, E.; Kurki, P.; Savolainen, H. Mercury-Bearing Black Shales and Human Hg Intake in Eastern Finland: Impact and Mechanisms. *Environ. Geol.* **43** (3), 283–297.
- (35) Lee, J.-S.; Chon, H.-T.; Kim, K.-W. Migration and Dispersion of Trace Elements in the Rock–soil–plant System in Areas Underlain by Black Shales and Slates of the Okchon Zone, Korea. *J. Geochem. Explor.* **1998**, *65* (1), 61–78.
- (36) US EPA, O. Study of the Potential Impacts of Hydraulic Fracturing on Drinking Water Resources: Progress Report <https://www.epa.gov/hfstudy/study-potential-impacts-hydraulic-fracturing-drinking-water-resources-progress-report-0>.
- (37) Smith, K.; Blunt, D.; Williams, G.; Tebes, C. *Radiological Dose Assessment Related to Management of Naturally Occurring Radioactive Materials Generated by the Petroleum Industry*; DTIC Document, 1996.
- (38) Blauch, M. E.; Myers, R. R.; Moore, T. R.; Lipinski, B. A. Marcellus Shale Post-Frac Flowback Waters - Where Is All the Salt Coming from and What Are the Implications? *Soc Pet. Eng* **2009**, 1–20.
- (39) Osborn, S. G.; Vengosh, A.; Warner, N. R.; Jackson, R. B. Methane Contamination of Drinking Water Accompanying Gas-Well Drilling and Hydraulic Fracturing. *Proc. Natl. Acad. Sci.* **2011**, *108* (20), 8172–8176.
- (40) Pritz, M. E.; Kirby, C. Geochemical Investigation of Marcellus Shale Natural Gas Hydrofracturing Waters; 2010; Vol. 42, p 121.
- (41) Fisher, R. S. Geologic and Geochemical Controls on Naturally Occurring Radioactive Materials (NORM) in Produced Water from Oil, Gas, and Geothermal Operations. *Environ. Geosci.* **1998**, *5* (3), 139–150.

- (42) Brumsack, H.-J. The Trace Metal Content of Recent Organic Carbon-Rich Sediments: Implications for Cretaceous Black Shale Formation. *Palaeogeogr. Palaeoclimatol. Palaeoecol.* **2006**, 232 (2–4), 344–361.
- (43) Vine, J. D.; Tourtelot, E. B. Geochemistry of Black Shale Deposits—a Summary Report. *Econ. Geol.* **1970**, 65 (3), 253–272.
- (44) Cluff, M. A.; Hartsock, A.; MacRae, J. D.; Carter, K.; Mouser, P. J. Temporal Changes in Microbial Ecology and Geochemistry in Produced Water from Hydraulically Fractured Marcellus Shale Gas Wells. *Environ. Sci. Technol.* **2014**, 48 (11), 6508–6517.
- (45) Fakhru'l-Razi, A.; Pendashteh, A.; Abdullah, L. C.; Biak, D. R. A.; Madaeni, S. S.; Abidin, Z. Z. Review of Technologies for Oil and Gas Produced Water Treatment. *J. Hazard. Mater.* **2009**, 170 (2–3), 530–551.
- (46) Lutz, B. D.; Lewis, A. N.; Doyle, M. W. Generation, Transport, and Disposal of Wastewater Associated with Marcellus Shale Gas Development. *Water Resour. Res.* **2013**, 49 (2), 647–656.
- (47) Barbot, E.; Vidic, N. S.; Gregory, K. B.; Vidic, R. D. Spatial and Temporal Correlation of Water Quality Parameters of Produced Waters from Devonian-Age Shale Following Hydraulic Fracturing. *Environ. Sci. Technol.* **2013**, 47 (6), 2562–2569.
- (48) Ferrar, K. J.; Michanowicz, D. R.; Christen, C. L.; Mulcahy, N.; Malone, S. L.; Sharma, R. K. Assessment of Effluent Contaminants from Three Facilities Discharging Marcellus Shale Wastewater to Surface Waters in Pennsylvania. *Environ. Sci. Technol.* **2013**, 47 (7), 3472–3481.
- (49) Haluszczak, L. O.; Rose, A. W.; Kump, L. R. Geochemical Evaluation of Flowback Brine from Marcellus Gas Wells in Pennsylvania, USA. *Appl. Geochem.* **2013**, 28, 55–61.

- (50) Stringfellow, W. T.; Domen, J. K.; Camarillo, M. K.; Sandelin, W. L.; Borglin, S. Physical, Chemical, and Biological Characteristics of Compounds Used in Hydraulic Fracturing. *J. Hazard. Mater.* **2014**, *275*, 37–54.
- (51) Balashov, V. N.; Engelder, T.; Gu, X.; Fantle, M. S.; Brantley, S. L. A Model Describing Flowback Chemistry Changes with Time after Marcellus Shale Hydraulic Fracturing. *AAPG Bull.* **2015**, *99* (1), 143–154.
- (52) Abualfaraj, N.; Gurian, P. L.; Olson, M. S. Characterization of Marcellus Shale Flowback Water. *Environ. Eng. Sci.* **2014**, *31* (9), 514–524.
- (53) John Duda; Deborah Elcock; Markus G. Puder; Robert J. Redweik; John A. Veil. *A White Paper Describing Produced Water from Production of Crude Oil, Natural Gas, and Coal Bed Methane*; United States Department of Energy, National Energy Technology Laboratory, 2004.
- (54) Bagheri, R.; Nadri, A.; Raeisi, E.; Kazemi, G. A.; Eggenkamp, H. G. M.; Montaseri, A. Origin of Brine in the Kangan Gasfield: Isotopic and Hydrogeochemical Approaches. *Environ. Earth Sci.* **2013**, *72* (4), 1055–1072.
- (55) Capo, R. C.; Stewart, B. W.; Rowan, E. L.; Kolesar Kohl, C. A.; Wall, A. J.; Chapman, E. C.; Hammack, R. W.; Schroeder, K. T. The Strontium Isotopic Evolution of Marcellus Formation Produced Waters, Southwestern Pennsylvania. *Int. J. Coal Geol.* **2014**, *126*, 57–63.
- (56) Stewart, B. W.; Chapman, E. C.; Capo, R. C.; Johnson, J. D.; Graney, J. R.; Kirby, C. S.; Schroeder, K. T. Origin of Brines, Salts and Carbonate from Shales of the Marcellus Formation: Evidence from Geochemical and Sr Isotope Study of Sequentially Extracted Fluids. *Appl. Geochem.*
- (57) Dieterich, M.; Kutchko, B.; Goodman, A. Characterization of Marcellus Shale and Huntersville Chert before and after Exposure to Hydraulic Fracturing Fluid via Feature

- Relocation Using Field-Emission Scanning Electron Microscopy. *Fuel* **2016**, *182*, 227–235.
- (58) Phan, T. T.; Capo, R. C.; Stewart, B. W.; Graney, J. R.; Johnson, J. D.; Sharma, S.; Toro, J. Trace Metal Distribution and Mobility in Drill Cuttings and Produced Waters from Marcellus Shale Gas Extraction: Uranium, Arsenic, Barium. *Appl. Geochem.* **2015**, *60*, 89–103.
- (59) Renock, D.; Landis, J. D.; Sharma, M. Reductive Weathering of Black Shale and Release of Barium during Hydraulic Fracturing. *Appl. Geochem.* **2016**, *65*, 73–86.
- (60) Wang, L.; Fortner, J. D.; Giammar, D. E. Impact of Water Chemistry on Element Mobilization from Eagle Ford Shale. *Environ. Eng. Sci.* **2014**.
- (61) Wang, L.; Burns, S.; Giammar, D. E.; Fortner, J. D. Element Mobilization from Bakken Shales as a Function of Water Chemistry. *Chemosphere* **2016**, *149*, 286–293.

Chapter 2

Role of Water-Rock Interactions in Controlling Shale Gas Produced Brine Composition

2.1 Introduction

In recent years, the oil and gas industry has been targeting organic-rich shales for natural gas production through a combination of horizontal drilling and hydraulic fracturing. Hydraulic fracturing (HF) fluids are composed primarily of water (>95%) but also contain a variety of chemical additives to enhance well stimulation and subsequent well productivity. These often include friction reducers, biocides, surfactants, scale inhibitors, gelling agents, acids, and corrosion inhibitors.^{1,2} Proppants, such as quartz sand, are also added to keep fractures open after the pressure is released to allow continued gas flow in the stimulated area. The particular chemical composition HF fluid depends on site-specific factors such as local geology, drilling and well construction plans and operator preferences. While most chemical HF Fluid recipes are proprietary, many operators now voluntarily disclose their chemical makeup through the website Fracfocus.org.

A portion of injected HF fluid returns to the surface as flowback water prior to the onset of gas production, but the exact percentage depends on factors such as duration of well shut-in and the initial saturation state of the reservoir.³ Typical flowback volumes for Marcellus shale gas wells range from 9-53% of the volume of HF fluid injected.⁴ The well will also produce brine water throughout its production lifetime. A side effect of hydraulic fracturing is the exposure of previously hydraulically isolated minerals that may contain

naturally occurring radioactive material and toxic metal elements.⁵⁻⁸ For example, radionuclides present in the shale, including U, Th, and their daughter products ²²⁶Ra and ²²⁸Ra, may be released into the HF fluids and produced water.^{5,9} In addition, flowback fluids may contain elevated concentrations of naturally-occurring salts, metals, and organics.^{3,4,10,11} Collectively, flowback and produced water represent the largest volume of waste associated with shale gas production. The EPA's targeted a list of chemicals for flowback water treatment include As, Ra, Sr, Ba, and U, among other inorganic and organic components.¹²

Many recent studies have characterized flowback waters associated with unconventional reservoir drilling to determine chemical signatures unique to shale reservoirs.^{10,11,13-19} Barbot et al.¹⁴ observed that Ba concentrations exhibited a strong dependence on geological provenance and location, while Haluszczak et al.¹⁵ reported that flowback water composition resembles formation brines formed by seawater evaporation. Isotopic analyses of Sr, Li, and B was used to determine produced brine origin.^{11,18} These studies also demonstrated that flowback water salinity and trace inorganic contaminants (*e.g.*, Ba, Ra) concentrations increase during early collection time periods and represent a mixture of injected water and native brines.

An area that has not yet received adequate attention is the contribution of water-rock reactions in controlling major inorganic, trace metal, and radionuclide concentrations in flowback water. Through a series of batch experiments examining the role of water chemistry in promoting element mobilization, Wang et al.^{20,21} demonstrated that fluid pH and redox conditions played a strong role in mobilizing trace elements from Eagle Ford and Bakken shales, while temperature and water:rock ratio were of secondary importance. They also concluded that sulfate (and As) leaching was largely driven by pyrite oxidation, and the low aqueous Ba concentration due to the low solubility of barite ($\text{BaSO}_{4(s)}$). In another study, Dieterich et al.²² observed calcite dissolution, fracture propagation, gypsum precipitation, and

also barite precipitation for shale samples interacting with synthetic HF fluids or recycled fracturing fluids Ali et al.²³ discussed possible mechanisms for sulfate, calcium, magnesium mobilization between deionized water and different types of shales including mineral dissolution, precipitation and cation exchange with shale.

To develop a more complete understanding of the factors controlling the chemical composition and evolution of HF flowback water, this study investigated the leaching of selected elements (U, Ba, As, Sr, Fe, Ca, K, Mg, Na) as a function of varying shale mineralogy, HF chemical additives, and system pressure and temperature. Batch leaching experiments were conducted on powdered shale rock samples from two Michigan basins under typical *in situ* temperature and pressure conditions. Sequential leaching experiments were performed to explore the release mechanisms and host phases responsible for leached elements of interest. To evaluate the applicability of the leaching experiments to the field, the results were compared to flowback water chemistry from a recently completed Utica-Collingwood shale gas well.

2.2 Materials and Methods

2.2.1 Shale samples

This study examined two shale gas reservoirs in Michigan: Utica-Collingwood and Antrim shales. Utica-Collingwood is an emerging shale gas reservoir being targeted for production at depths of approximately 3 km in the northern half of Michigan's lower-peninsula. It is comprised of both the Utica shale and the organic-rich Collingwood limestone. Antrim shale has been actively produced since the 1980's but drilling in this reservoir is on the decline. Collectively, these three formations provide a cross-section in time of deposition (Middle Ordovician to Upper Devonian), reservoir production strategy (high volume slickwater vs. nitrogen foam fracturing), and mineralogical composition (typical shale to organic-rich

limestone) for studying the influence of HF fluid-shale interaction on flowback water and produced brine composition.

The Collingwood and Utica shale samples were collected at the Michigan Geological Repository for Research and Education from drill core material from the JEM Brugger #3-7 well. The Collingwood samples were taken from depths between 2948-2954 m and Utica shale samples from depths between 2940-2944 m. Antrim shale samples were gathered from the Thompson 1-27 well at depths ranging between 127-151 m. All shale samples were ground to a powder and sieve-separated to achieve an approximately uniform grain size of 425 μm . All of the powdered shale samples had an initial specific surface area in the range of 1-2 m^2/g as estimated by the BET method²⁴ with N_2 adsorption. Shale mineralogy was determined via X-ray diffraction, with mineral weight percentages (Table 2.1).

Table 2.1: Shale composition as determined by X-ray diffraction.

Shale	Mineral (wt.%)	
Utica	Calcite (3%)	Quartz (19%)
	Ankerite (8%)	Feldspar (19%)
	Illite (38%)	Pyrite (2%)
	Chlorite (8%)	Muscovite (3%)
Collingwood	Calcite (44%)	Pyrite (1%)
	Dolomite (5%)	Muscovite (2%)
	Ankerite (4%)	Illite (26%)
	Quartz (11%)	Chlorite (2%)
	Feldspar (5%)	
Antrim	Ankerite (3%)	Muscovite (2%)
	Quartz (30%)	Feldspar (10%)
	Illite (38%)	Pyrite (3%)
	Chlorite (14%)	

2.2.2 Acid digestions and sequential extraction experiments

Hot nitric acid digestions, complete mineral digestions, and sequential extraction experiments were conducted to determine the elemental content of the shale samples used in this study. The hot nitric acid digestions were performed using trace metal grade concentrated

nitric acid following EPA Method 3050B to determine the maximum amount of environmentally available elements from the shale samples. Though this procedure does not completely digest the shale sample, it does provide a reasonable assessment of the maximum leaching that could occur after hydraulic fracturing. Complete sample digestions were also carried out by Activation Laboratories, Ltd using the 4B2-STD method modified from standard ASTM D4506 method. A four-step sequential chemical extraction was completed following the procedure described by Tessier et al.²⁵ The sequential extraction was designed to assess the nature of the trace metals association in five fractions as: water soluble, exchangeable, bound to carbonates, bound to sulfide and organic matter, and residual. This procedure was used to assign the origin of leached elements of interest to the various accessible mineral phases in the shale samples. A full discussion of sequential extraction procedures and results can be found in Appendix A section A-2.

2.2.3 Batch experiments

Shale leaching experiments were conducted with powdered shale material from the Antrim, Collingwood, and Utica formations. A 1:1 mix of the Utica and Collingwood was also studied, as these formations are targeted simultaneously for shale gas extraction in Michigan. The powdered shale samples were brought into contact with various fluid mixtures in a high-pressure batch reactor apparatus under a range of temperature and pressure conditions. The reactor system includes a 600 ml stainless steel high-pressure vessel (Parr Instrument) with specialized high-pressure functioning pH, Eh, and reference electrodes (Corr Instruments). A fluid sampling port allows for sampling the water phase under pressure and is fitted with a sintered metal filter inside the reactor to ensure minimal solids loss when taking samples. Each batch experiment was conducted under a nitrogen head space with a shale:water loading ratio of 10 g shale to 1 L fluid (estimation of rock/water ratio shown in Appendix A section A-1).

The batch reactor was continuously stirred via a magnetic stir bar throughout the duration of each ~3-day long experiment. Two grouped temperature and pressure conditions of 10 MPa / 34°C and 15 MPa / 43°C were evaluated, representing depths of approximately 1 km and 1.5 km, respectively. Ambient conditions (0.1 MPa / 23°C) were also studied.

Typical hydraulic fracturing fluids often contain more than 10 different chemical additives that serve various functions. This study examined the influence of an acid, gel breaker, clay stabilizer, and metal chelator on the release of selected metals and radionuclides from Michigan Basin shales. The four chemical additives and corresponding concentrations for the simplified synthetic HF fluid are given in Table 2.2. The concentrations used represent upper-end usage values for Michigan shale gas wells (data from fracfocus.org). These particular additives were expected to have the greatest potential influence on metal ion or radionuclide release from shale by either enhancing shale mineral dissolution (e.g., HCl by changing pH or ammonium persulfate by changing redox conditions) or by changing adsorption or ion exchange properties of targeted elements (e.g., citric acid or choline chloride).

Table 2.2: Hydraulic fracturing fluid chemical additives examined in this study

Chemical additive	Function in HF fluid	Conc. (mM)
HCl (hydrochloric acid)	Acid	30
(NH ₄) ₂ S ₂ O ₈ (ammonium persulfate)	Gel breaker	1
C ₆ H ₈ O ₇ (citric acid)	Iron control	0.64
C ₅ H ₁₄ ClNO (choline chloride)	Clay stabilizer	10

2.2.4 Flowback water sampling

Flowback water was sampled from a recently completed Utica-Collingwood well (State Beaver Creek 1-23 HD-1) from the Utica-Collingwood formation at an approximate depth of

3 km. Samples were taken 2 hours after the initial flowback was initiated from a port downstream of the wellhead but upstream of the storage tank. After the onset of gas production, water samples were collected from the separator.

2.2.5 Chemical analysis

Dissolved metals analysis was conducted on an Agilent 7900 inductively coupled plasma mass spectrometer (ICP-MS). For ICP-MS analysis, all samples were filtered through a 0.22 μm (batch experiments, digestions) or a 0.45 μm (flowback field samples) PTFE filter and acidified to a pH of 2 using nitric acid. High-purity germanium (HPGe) gamma spectroscopy was used to directly measure long half-life radium isotopes in flowback water samples. A mixed multiple isotope standard (Eckert & Ziegler 7501) with a density of 1.2 g/cm^3 was used for HPGe calibration. Flowback samples were decanted into 500 ml HDPE bottles, with NaCl added as needed to achieve a uniform density of 1.2 g/cm^3 . The samples were then amended with 5% Bacto agar to achieve a uniform suspension. Samples were allowed to sit for 21 days in a closed container to ensure ^{222}Rn , the short-lived daughter product of ^{226}Ra decay, reached secular equilibrium. Subsequently, the daughter decay products ^{214}Bi and ^{228}Ac were used to measure ^{226}Ra and ^{228}Ra activities, respectively.

2.3 Results and Discussion

This study monitored the release of major cations, trace metals, and radionuclides from shale samples in contact with simulated hydraulic fracturing (HF) fluids under *in situ* reservoir conditions. In 51 batch reactor experiments, the extent of element leaching was measured for three representative shale mineralogical compositions and three temperature and pressure conditions in simulated HF fluids containing various mixtures of four commonly used chemical

additives (see Appendix A Table A3-1 for complete list of experiments). The following sections discuss the relative impact of the experimental system conditions on the release of metals and radionuclides from the shale rocks examined in this study.

2.3.1 Acid digestion and sequential extraction

Results from the sequential extraction are presented in Figure 2.1 as an extraction percentage (mass/mass) compared to the total extractable from the hot nitric acid digestions. The colored bars in Figure 2.1 indicate the relative extractability of selected inorganic elements (U, Ba, As, Sr, Fe, Ca, K, Mg, Na) from different phases designated as: (1) water soluble phases (orange), (2) phases with exchangeable sites (blue), (3) carbonates phases (red), and (4) reduced mineral and organic phases (green).

Per Figure 2.1, As and Fe are bound primarily in reduced mineral and organic phases in the shales tested. SEM observations confirm the presence of framboidal pyrite (FeS_2) in all shales (see Appendix A section A-4). Arsenic is typically found in As-bearing pyrite (arsenian pyrite: $\text{Fe}(\text{As},\text{S})_2$)^{26,27} and when As-bearing pyrite is present in shale, the leaching of Fe and As by HF fluids should correlate with one another, and with pyrite dissolution, if a low pH is maintained, and no other insoluble Fe phases can precipitate.

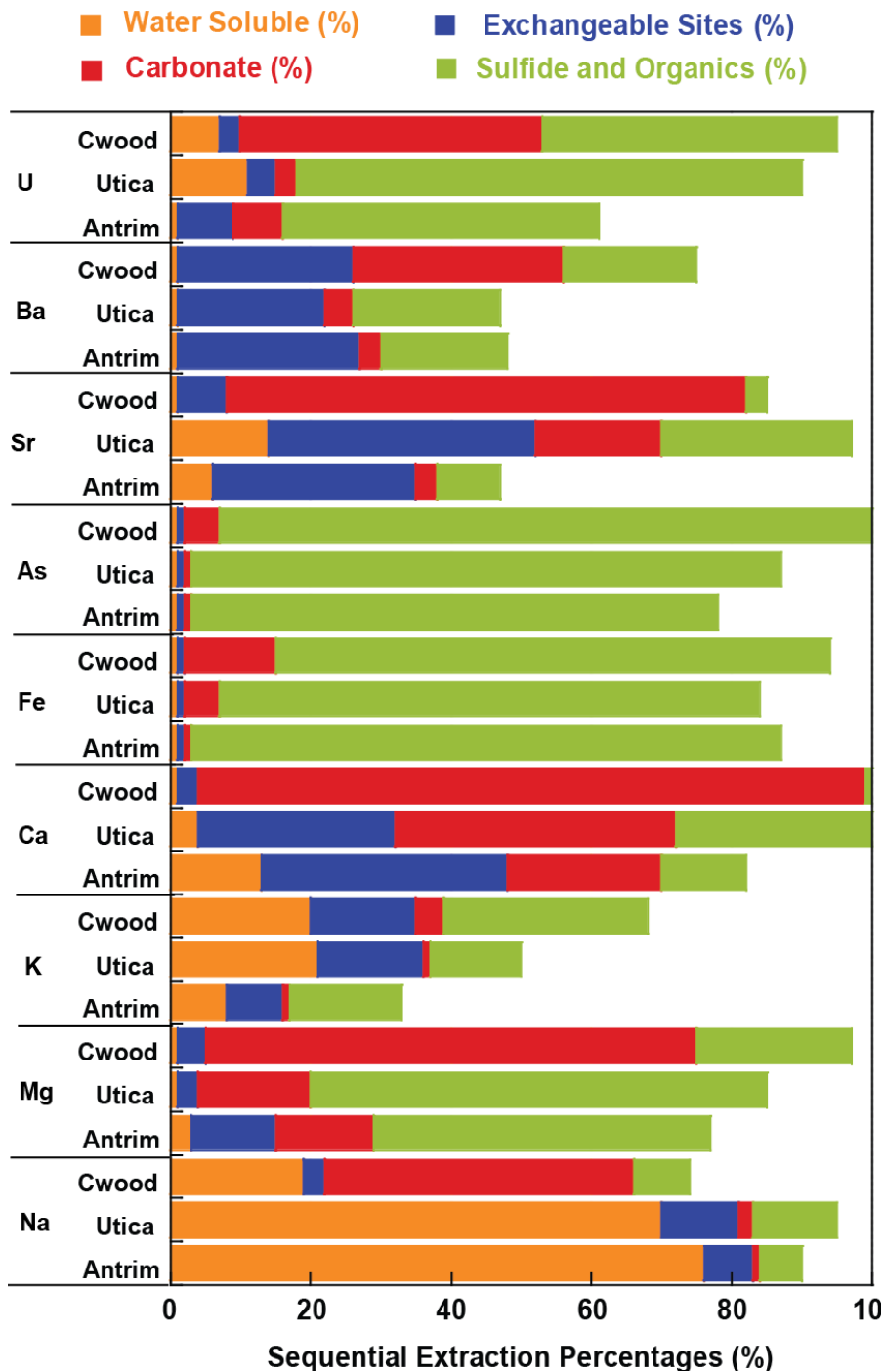


Figure 2.1: Sequential extraction percentages results of different elements (U, Ba, Sr, As, Fe, Ca, K, Mg, Na) for three shale samples (Collingwood, Utica, Antrim).

Uranium is also commonly present in shales in reduced mineral phases (*e.g.*, uraninite: $\text{UO}_2(\text{s})$). Since U(IV) is much less soluble than U(VI) and organic-rich shales reflect long-standing reducing conditions, the presence of U(IV) is not surprising.²⁸ Given this, U leaching

behavior is expected to be similar to that of Fe and As, which was the case for the Antrim and Utica shales (Figure 2.1). However, U was also found to be distributed equally between the carbonate minerals and reduced phases in the Collingwood (Figure 2.1). Given the high content of calcite (CaCO_3) in the Collingwood (Table 2.1), and that $(\text{UO}_2)^{2+}$ can substitute for Ca^{2+} within the calcite crystal lattice,²⁹ this too is reasonable.

The leaching of two major (Ca and Mg) and two minor alkaline earth cations (Sr and Ba) was also measured. Each of these showed extraction percentages in the carbonate phases in rough proportion to the presence of the carbonate minerals (Collingwood > Utica > Antrim: Figure 2.1). The alkali elements Na and K were found in a high percentage in the water soluble fractions, consistent with their presence in highly soluble phases like chloride or sulfate evaporites. Na, K, Ca, Sr, Ba, and Mg were also found in the clay exchangeable fraction, consistent with their favorable and reversible exchange with fixed-charge sites of clay minerals.

2.3.2 Influence of *in situ* T, P, and shale mineralogy on element mobilization

Element leaching experiments were conducted at three different temperature (T) and pressure (P) conditions, two encompassing the range expected for *in situ* geologic depths of 1 to 1.5 km (34°C /10 MPa and 43°C /15 MPa), and one at ambient conditions (25°C / 0.1 MPa) for comparison. Four different shale compositions were investigated, including a 1:1 mixture of Utica-Collingwood (UC), Collingwood-only (C), Utica-only (U), and Antrim (A). The 1:1 mixture of Utica-Collingwood and Utica- or Collingwood-only compositions were chosen to illustrate the impact of the Collingwood limestone in dominating the leaching behavior in the Utica-Collingwood formation. The Antrim shale is representative of a shale reservoir with low calcite content and stands in contrast to the carbonate-rich Utica-Collingwood shale gas play. The Utica, comprised primarily of clay and quartz, is a common shale type, whereas the Collingwood limestone represents shale with a relatively high fraction of carbonate minerals

(~50%, Table 2.1). As carbonates provide buffering against the potential pH change from the presence of strong acids present in HF fluids, the relative carbonate mineral concentration in the rock could have a significant impact on the extent of mineral dissolution and element leaching. Since carbonates also dissolve more easily and rapidly compared to clay or quartz, carbonate mineral dissolution was expected to be an important variable in controlling the extent of element leaching.

Figure 2.2 shows Ca dissolution from a UC 1:1 mixture in contact with deionized (DI) water and a synthetic HF fluid with the four chemical additives (Table 2.2) for three different T and P combinations. As shown in Figure 2.2, elevated T and P conditions in comparison to ambient conditions do not promote calcium dissolution for the UC shale mixture. Although elevated T, P conditions can influence solubility and dissolution rates of minerals, calcite solubility does not vary significantly under the examined experimental conditions investigated (see Appendix A, Table A5-1). Therefore, when carbonate minerals are an important source of trace elements, elevated T and P, may not be a controlling factor for trace element leaching. Consistent with this, T and P had little impact on the leaching from UC shale of the other elements investigated (not shown).

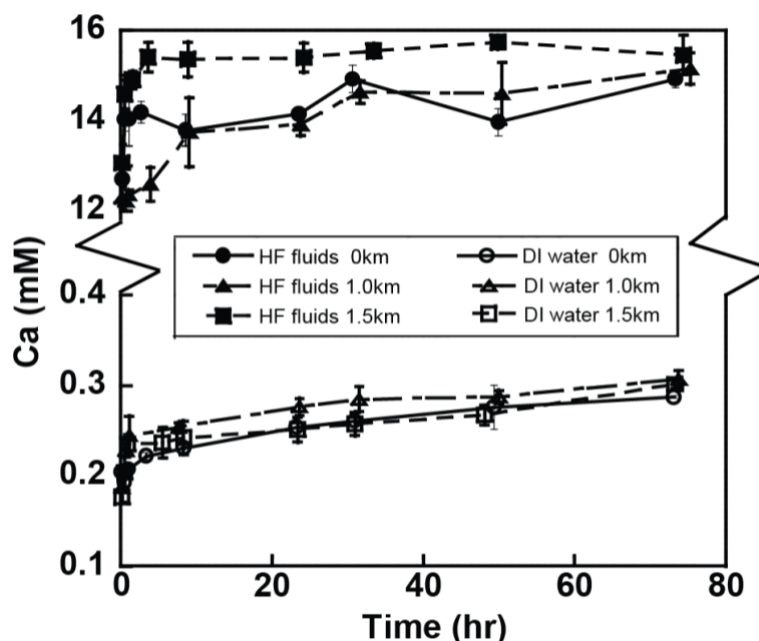


Figure 2.2: Leaching of calcium from a Utica-Collingwood 1:1 mixture in contact with DI water (open symbols) and the model hydraulic fracturing fluid chemical mixture (full composition shown in Table 2.2) (closed symbols. Three different T, P conditions were investigated: 25°C, 1 atm (circle); 34°C, 100 atm (triangle); 43°C, 150 atm (square).

2.3.3 Influence of HF fluids on element mobilization

The HF fluid constituents investigated in this study included an acid, oxidizer, chelator, and clay stabilizer. Four different chemical compositions (ultrapure DI water; ammonium persulfate and choline chloride; HCl and citric acid, and all four chemical additives) were evaluated to assess the impact of different chemical additives individually and collectively on element leaching from the different MI shales. For these experiments, the system T and P were fixed at 34°C and 10 MPa. The key variables investigated in this leaching study included pH (presence or absence of strong acid), redox condition (presence or absence of the oxidizer), and buffering capacity (based on differing amounts of carbonates in each shale composition studied).

2.3.3.1 pH as a key factor for trace element mobilization

The pH profiles as a function of leaching time for model HF fluid with all four additives (Table 2.2) and three shales, respectively, are shown in Figure 2.3a. For the Collingwood shale, the pH quickly increased to ~6.5 within the first half hour. For the Utica and Antrim shale experiments, the pH stayed quite low (~2) for the duration of the experiment leading to higher U extraction efficiencies compared to the carbonate-rich Collingwood limestone, which quickly obtained a neutral pH (Figure 2.3b). Approximately 45% of the U in Antrim and Utica shale was released after contact with the model HF fluid compared to only in ~20% for the Collingwood. Similar leaching behavior of the other elements investigated in this study was observed (Appendix A section A-6), in which a lower pH enhanced element leaching by promoting mineral dissolution. As confirm in this study, and reported recently by others^{20,21}, pH is a major factor controlling the release of the trace metal cations.

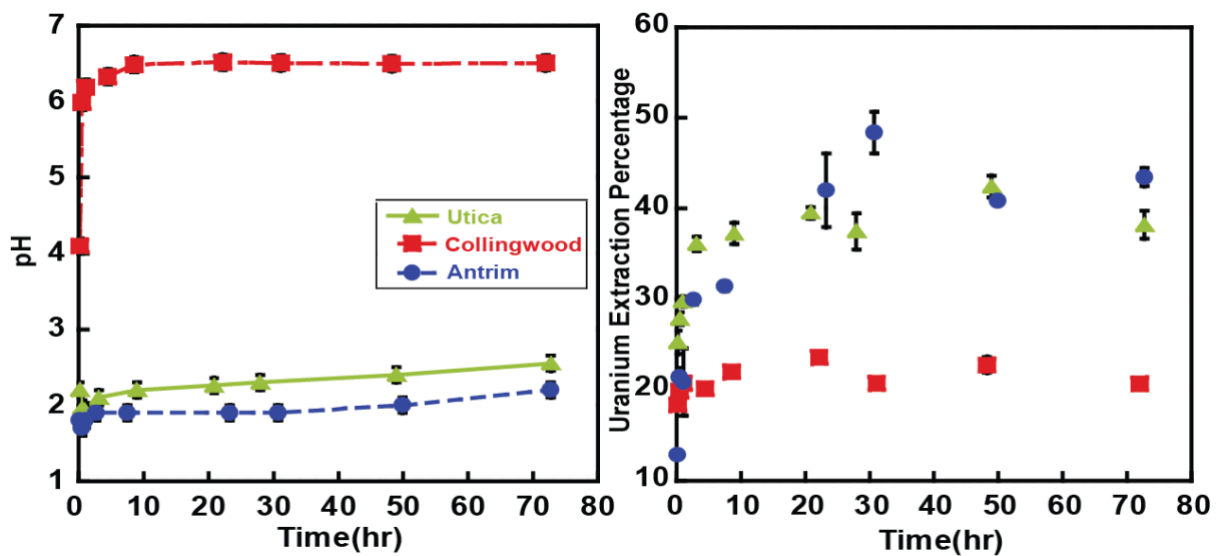


Figure 2.3: pH evolution (a) and extraction percentages (U/U_{total}) of uranium (b) from Utica, Collingwood and Antrim shale after contact with model HF fluids (full composition shown in Table 2) at 1.0 km T, P conditions and a rock–water ratio of 10 g/L.

2.3.3.2 Carbonates as a source of pH buffering and trace element release

The weight fraction of carbonates and other acid neutralizing phases in shale will impact its ability to buffer against pH change when strong acid HF fluids are injected into shale formations. To evaluate this influence, the buffer capacity for the shales used in this study was estimated. Defining buffer capacity as the effective amount of strong acid that can be neutralized³⁰, the buffer capacities of the Collingwood, Utica, and Antrim samples were estimated to be 10, 0.4, and 0.1 (mmol-H⁺/g shale), respectively, assuming calcite in the shale is the primary buffering source (Appendix A section A-7). Figure 2.3a shows the carbonate-rich Collingwood quickly neutralized the strong acidic HF fluid (pH ~1.2) to a pH of 6.5. When the shale lacks sufficient carbonate mineral abundance to effectively neutralize the addition of strong acid, such as for the Utica and Antrim shales, the low pH persists and leads to significant element leaching (as noted in Figure 2.3b for U; and in section A-6 in Appendix A for the other elements monitored).

In addition to providing pH buffering, carbonate minerals in shale can also be a source of trace elements. Many cations (*e.g.*, Ba, Sr, U) or oxyacids (As) can form solid solution with calcite or other carbonate minerals.³¹ As shown by the sequential extraction experiments in this study, 74% of Sr, 43% of U, 30% of Ba, and 5% of As were present in carbonate mineral phases in the Collingwood (Figure 2.1, Table A-2). Hence acid-driven carbonate mineral dissolution can be a significant source of trace elements in flowback water if strong acidic conditions prevail.

2.3.3.3 Influence of redox potential on pyrite dissolution

Redox potential may also affect the leaching of elements from mineral phases associated with shale. Shales created under reducing conditions are typically comprised of reduced mineral phases. When exposed to the strong acids and oxidants present in HF fluids,

the reduced mineral phases in shale may undergo acid-driven dissolution or acid-assisted oxidative dissolution. Different leaching behavior of Fe and As occurs when exposing Antrim shale to various synthetic HF fluid chemical mixtures (Figure 2.4). In the presence of water only, no Fe or As leaching occurs. When acid is present, both Fe and As dissolve and increase in similar fashion with time. This is consistent with acid dissolution of a reduced arsenic bearing Fe(II) mineral such as arsenian pyrite. Similar trends (Appendix A section A-10), but with enhanced dissolution, occurred when an oxidizer (*e.g.*, ammonium persulfate) was present in the HF fluid. In the case of pyrite dissolution in the presence of oxygen, an experimental redox potential of 593 ± 5 mV at $\text{pH} = 2.5 \pm 0.1$ was reported.³² This is similar to the experimentally measured Eh of ~ 600 mV at pH 2.2 of the present study (see, *e.g.*, Appendix A section A-8). The measured Eh for Antrim shale ~ 600 mV at pH 2.2 falls within the Eh-pH stability field diagram of dissolved Fe^{2+} bounded by pyrite and $\text{Fe}(\text{OH})_3$ solids (Appendix A section A9-1), but above the Eh of ~ 200 mV of redox couple of pyrite/ Fe^{2+} at pH 2.2. Having not yet reached the equilibrium Eh-pH position expected by the presence of oxygen, this analysis supports a kinetic control of Fe^{2+} dissolution of shale in the leaching experiments.

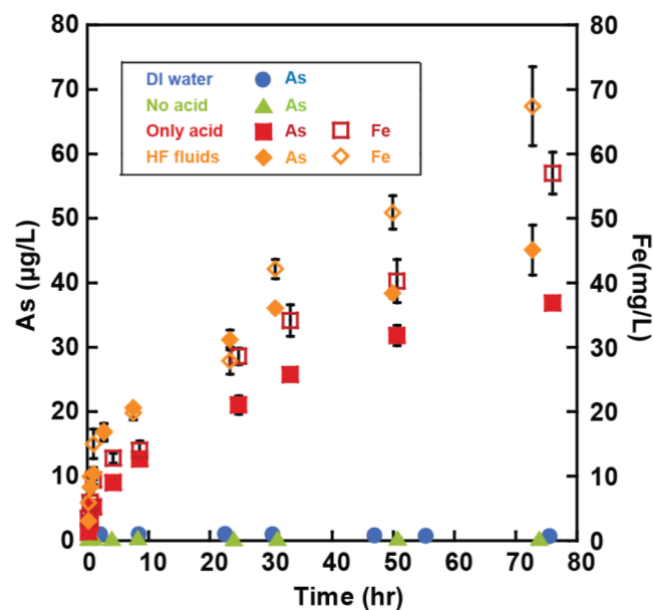


Figure 2.4: Arsenic (solid symbols) and Iron (open symbols) leaching profile of Antrim in contact with different chemical additives.

A batch Fe²⁺ leaching experiment using Antrim shale at pH 2.2 shows two distinct periods of Fe²⁺ dissolution, a fast initial Fe release followed by a much slower release (Figure A9-3). To model the dissolution behavior, the Geochemist's Workbench (GWB) dissolution/precipitation rate model was used (Appendix A section A9-2). According to the results, the initial rapid Fe release is fit well assuming a dissolution rate control of an Fe(II)-bearing carbonate (*e.g.*, ankerite) in the shale (Figure A9-3). After the carbonate is exhausted (predicted at ~0.5 hrs), the model attributes the Fe(II) release to the slower rate of pyrite dissolution (Figure A9-5), with approximately 1/3 of the available pyrite dissolved from the shale after 3 days (Figure A9-4).

Dissolved As follows a similar trend to that of Fe in all Antrim batch experiments (Figure 2.4). The strong correlation ($R > 0.95$) between the ratio of the dissolved concentration of As and Fe (Figure A10-1), suggests release from a common host mineral, *e.g.*, arsenian pyrite. The addition of oxidizer apparently enhanced pyrite dissolution, leading to slightly higher dissolved Fe in the experiments compared to the addition of acid only (Figure 2.4). By assuming the higher dissolved Fe came from pyrite dissolution, it is estimated that an additional 8% of pyrite (0.084g in total) was dissolved due to the presence of the oxidant. Although the oxidant promoted some additional pyrite dissolution, the low pH continues to be the main factor controlling pyrite dissolution.

2.3.4 Comparison of flowback water with batch experiments results

A series of flowback water samples from a Utica-Collingwood natural gas well were analyzed and compared with the batch experiment results to evaluate the extent to which shale-HF fluid interactions may contribute to observed flowback water composition. Flowback water observations (Appendix A section A-11) show increasing concentration of major cations (Na,

Ca, Mg, Fe, Sr) and anions (Cl, Br) during the first ~20 days after which the concentrations reach steady values.

The evolution of dissolved Ba is opposite to that of sulfate (Figure 2.5). Barite is over saturated in all samples (Table A11-1), suggesting that barite solubility may be controlling the concentration of dissolved Ba in solution.³³ For example, due to its limited solubility, even trace concentrations of sulfate will lead to barite precipitation, and when sulfate is in excess of Ba, it will control Ba solubility, keeping Ba concentrations very low. Possible sources of sulfate in flowback water include soluble sulfate minerals (*e.g.*, anhydrite), persulfate (added as gel breaker) decomposition, or pyrite oxidative dissolution. Secondary mineral precipitation (*e.g.*, barite) or sulfate reducing bacterial activity could both decrease sulfate in flowback water, as was observed in the flowback water over time (Figure 2.5). The trend of increasing dissolved Ba but decreasing sulfate was also observed in the UC mixture batch experiments (Figure A11-1).

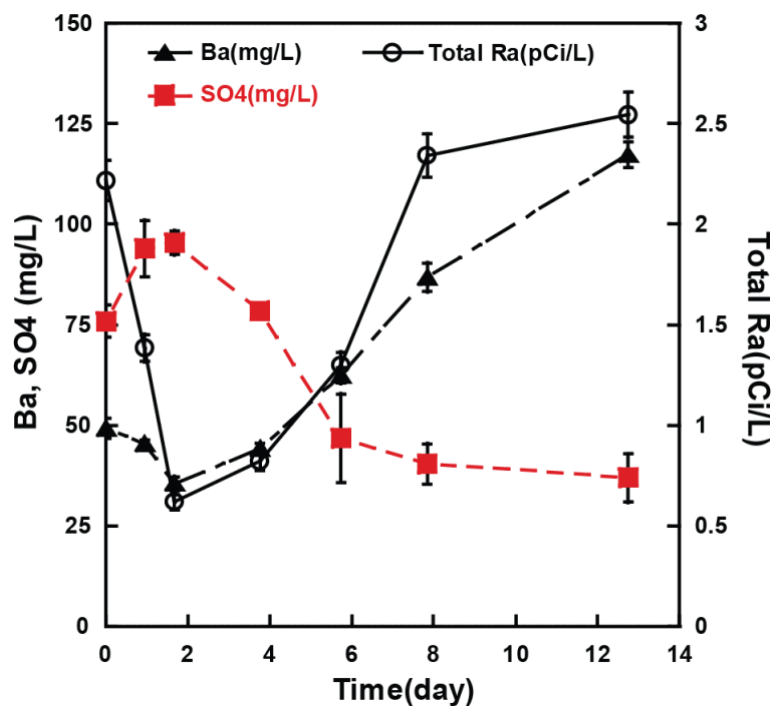


Figure 2.5: Evolution of barium, sulfate, and radium concentration in flowback water sample.

Total dissolved Ra and Ba concentration profiles for the first few days of flowback water sampling are nearly identical (Figure 2.5). With similar ionic radii to Ba, Ra coprecipitates with Ba in barite³³ likely leading to the similar Ra and Ba concentration trends observed in the flowback water.

The shale/water ratio for the Utica-Collingwood flowback water was estimated to be in the range of 0.01-20g/L (discussed in Appendix A section A-1). Compared to the batch experiments (with 10g-shale/L-water), much higher concentrations of Br, Na, Ba, Sr, Ca, Mg, Fe, Cl, and lower concentrations of sulfate, U and As, respectively, were observed in the field samples. The U and As were below the detection limits in the flowback samples (<detection limit ~1 µg/L). Br was not observed in the batch experiments, but was present at concentrations on the order of 2000 mg/L in flowback water samples. The presence of Br suggests its presence in connate water with an origin from seawater evaporates.¹⁴ The various differences difference noted above cannot be fully explained by the different shale:water ratio. In particular, the negligible amount of dissolved U and As in all field samples suggests these elements are either not readily mobilized through HF fluid:rock interactions in the field compared to the batch studies, or more likely that the acid pH is not maintained in flowback water and they are reincorporated by precipitation or adsorbed to other oxidized mineral phases in the formation (e.g., ferric hydroxide phases).

Total Ra activity was ~2000 pCi/L (using gamma ray spectroscopy) in the field samples but below the detection limit (<1250 pCi/L for ICP-MS measurement) in the batch experiments. The longer-lived Ra isotopes (Ra-226 and Ra-228) are decay products of U-238 and Th-232 that formed hundreds of million years ago and are widely distributed in shale. Shale formations are not completely dry and connate water exists before fracturing. In the closed shale formation prior to fracturing, all decay daughter products eventually (after ~2 million years) reach secular equilibrium³⁴ in both the shale and the associated connate water, which means the

daughter/parent activity ratio reaches unity. The Ra-226 and Ra-228 activity levels are similar in field samples. Assuming secular equilibrium, the Ra-226 concentration would be ~1.1 pg/g in the UC rock mixture. In batch experiments with a 10 g/L shale:HF fluid ratio, the Ra-226 is calculated to be 11.1 pCi/L (11.1 pg/L) in solution, assuming all Ra-226 in the shale is leached into solution (see calculation details in Appendix A section A-12). Compared to the relatively higher Ra levels often found in one Collingwood well initial flowback water samples (*e.g.*, from 1,200 – 4,400 pCi/L), the Ra level in flowback water would be expected to be at least two or three orders magnitude lower under reasonable shale:HF fluids ratio, if shale leaching was the main source for Ra in flowback water. This difference indicates that the higher Ra level in flowback water probably does not originate from short-term shale dissolution occurring in the field. The other popular theory is that connate water might be the main source for high Ra activity in flowback water samples. The shale:water (or shale:connate water) ratio depends on porosity and water saturation of the formation. By assuming a representative porosity of 5%, 50% water saturation, and shale rock density as 2.7 g/cm³, the shale:connate water ratio would be ~100,000 g/L. This 100,000 g/L agrees with the order of shale/water ratio estimated in hydraulically fractured wells by Renock et al.³⁵ This high but realistic ratio provides a more plausible basis for high Ra levels observed in actual initial field flowback water samples, even after accounting for dilution of the connate water by the HF injected fluid.

2.3.5 *Environmental implication*

Results from this study demonstrate that the extent of HF fluid induced leaching of trace toxic elements from shale reservoirs is primarily pH driven. Low pH conditions may persist in shale without sufficient carbonate mineral content to buffer and neutralize the acidic fracturing fluids. Persistent low pH conditions and the use of oxidants in hydraulic fracturing fluids may accelerate the dissolution of more recalcitrant minerals and promote leaching of

trace toxic elements. Although carbonate mineral dissolution may inhibit acid-driven dissolution of other less reactive minerals, it could also serve as a source of other regulated contaminants, such as U and Ba that commonly co-precipitated with carbonates.

Shale minerals are the ultimate source of contaminants observed in flowback waters but a majority of these elements in produced and flowback water likely come from shale connate brines as a result of long residence time of the brines in contact with the shale prior to fracking. Mineral dissolution induced by the injection of HF fluids into shale gas reservoirs is likely to important only for those elements that are released relatively rapidly from a carbonate phase following hydraulic fracturing completions.

2.4 References:

- (1) King, G. E. Hydraulic Fracturing 101: What Every Representative, Environmentalist, Regulator, Reporter, Investor, University Researcher, Neighbor and Engineer Should Know About Estimating Frac Risk and Improving Frac Performance in Unconventional Gas and Oil Wells. *Society of Petroleum Engineers*, **2012**; DOI:10.2118/152596-MS.
- (2) Fontaine, J. S.; Johnson, N. J.; Schoen, D. Design, Execution, and Evaluation of a “Typical” Marcellus Shale Slickwater Stimulation: A Case History. *Society of Petroleum Engineers*, **2008**; DOI:10.2118/117772-MS.
- (3) Gregory, K. B.; Vidic, R. D.; Dzombak, D. A. Water Management Challenges Associated with the Production of Shale Gas by Hydraulic Fracturing. *Elements*. **2011**, 7 (3), 181–186; DOI: 10.2113/gselements.7.3.181.
- (4) Vidic, R. D.; Brantley, S. L.; Vandenbossche, J. M.; Yoxtheimer, D.; Abad, J. D. Impact of Shale Gas Development on Regional Water Quality. *Science* **2013**, 340 (6134), DOI: 10.1126/science.1235009.
- (5) Fisher, R. S. Geologic and Geochemical Controls on Naturally Occurring Radioactive Materials (NORM) in Produced Water from Oil, Gas, and Geothermal Operations. *Environ. Geosci.* **1998**, 5 (3), 139–150; DOI: 10.1046/j.1526-0984.1998.08018.x.
- (6) Leventhal, J. Pyrolysis-Gas Chromatography-Mass Spectrometry to Characterize Organic-Matter and Its Relationship to Uranium Content of Appalachian Devonian Black Shales. *Geochim. Cosmochim. Acta* **1981**, 45 (6), 883–889; DOI: 10.1016/0016-7037(81)90116-2.
- (7) Brumsack, H. J. The trace metal content of recent organic carbon-rich sediments: Implications for Cretaceous black shale formation. *Palaeogeogr. Palaeoclimatol. Palaeoecol.* **2006**, 232 (2-4), 344–361; DOI:10.1016/j.palaeo.2005.05.011.

- (8) Vine, J. D.; Tourtelo, E. B. Geochemistry of Black Shale Deposits - a Summary Report. *Econ. Geol.* **1970**, *65* (3), 253–272; DOI: 10.2113/gsecongeo.65.3.253.
- (9) Smith, K. P.; Blunt, D. L.; Williams, G. P.; Tebes, C. L. Radiological dose assessment related to management of naturally occurring radioactive materials generated by the petroleum industry. *Society of Petroleum Engineers*.**1995**; DOI: 10.2118/29712-MS.
- (10) Blauch, M.; Myers, R. R., Moore, T., Lipinski, B. A., & Houston, N. A. Marcellus Shale Post-Frac Flowback Waters - Where is All the Salt Coming from and What are the Implications? *Society of Petroleum Engineers*.**2009**; DOI:10.2118/125740-MS.
- (11) Chapman, E. C.; Capo, R. C.; Stewart, B. W.; Kirby, C. S.; Hammack, R. W.; Schroeder, K. T.; Edenborn, H. M. Geochemical and Strontium Isotope Characterization of Produced Waters from Marcellus Shale Natural Gas Extraction. *Environ. Sci. Technol.* **2012**, *46* (6), 3545–3553; DOI: 10.1021/es204005g.
- (12) U.S. Environmental Protection Agency. Study of the potential impacts of hydraulic fracturing on drinking water resources: Progress Report. EPA 601/R-12/011; **2012**; <https://www.epa.gov/sites/production/files/documents/hf-report20121214.pdf>
- (13) Hayes, T. Sampling and Analysis of Water Streams Associated with the Development of Marcellus Shale Gas; *Marcellus Shale Coalition*, **2009**. <http://energyindepth.org/wp-content/uploads/marcellus/2012/11/MSCCommission-Report.pdf>
- (14) Barbot, E.; Vidic, N. S.; Gregory, K. B.; Vidic, R. D. Spatial and Temporal Correlation of Water Quality Parameters of Produced Waters from Devonian-Age Shale following Hydraulic Fracturing. *Environ. Sci. Technol.* **2013**, *47* (6), 2562–2569; DOI: 10.1021/es304638h.
- (15) Haluszczak, L. O.; Rose, A. W.; Kump, L. R. Geochemical evaluation of flowback brine from Marcellus gas wells in Pennsylvania, USA. *Appl. Geochem.* **2013**, *28*, 55–61; DOI: 10.1016/j.apgeochem.2012.10.002

- (16) Stringfellow, W. T.; Domen, J. K.; Camarillo, M. K.; Sandelin, W. L.; Borglin, S. Physical, chemical, and biological characteristics of compounds used in hydraulic fracturing. *J. Hazard. Mater.* **2014**, *275*, 37–54. DOI: 10.1016/j.jhazmat.2014.04.040.
- (17) Abualfaraj, N.; Gurian, P. L.; Olson, M. S. Characterization of Marcellus Shale Flowback Water. *Environ. Eng. Sci.* **2014**, *31*(9), 514–524; DOI:10.1089/ees.2014.0001.
- (18) Warner, N. R.; Darrah, T. H.; Jackson, R. B.; Millot, R.; Kloppmann, W.; Vengosh, A. New Tracers Identify Hydraulic Fracturing Fluids and Accidental Releases from Oil and Gas Operations. *Environ. Sci. Technol.* **2014**, *48* (21), 12552–12560; DOI: 10.1021/es5032135.
- (19) Ziemkiewicz, P. F.; Thomas He, Y. Evolution of water chemistry during Marcellus Shale gas development: A case study in West Virginia. *Chemosphere.* **2015**, *134*(224–231); DOI:10.1016/j.chemosphere.2015.04.040.
- (20) Wang, L.; Fortner, J. D.; Giammar, D. E. Impact of Water Chemistry on Element Mobilization from Eagle Ford Shale. *Environ. Eng. Sci.* **2015**, *32*(4), 310–320; DOI: 10.1089/ees.2014.0342.
- (21) Wang, L.; Burns, S.; Giammar, D. E.; Fortner, J. D. Element mobilization from Bakken shales as a function of water chemistry. *Chemosphere.* **2016**, *149*, 286–293; DOI: 10.1016/j.chemosphere.2016.01.107.
- (22) Dieterich, M.; Kutchko, B.; Goodman, A. Characterization of Marcellus Shale and Huntersville Chert before and after exposure to hydraulic fracturing fluid via feature relocation using field-emission scanning electron microscopy. *Fuel.* **2016**, *182*, 227–235; DOI:10.1016/j.fuel.2016.05.061.
- (23) Ali, M.; Hascakir, B. Water-Rock Interaction for Eagle Ford, Marcellus, Green River, and Barnett Shale Samples; *Society of Petroleum Engineers*, **2015**; DOI: 10.2118/177304-MS.

- (24) Brunauer, S.; Emmett, P. H.; Teller, E. Adsorption of Gases in Multimolecular Layers. *J. Am. Chem. Soc.* **1938**, *60* (2), 309–319; DOI: 10.1021/ja01269a023.
- (25) Tessier, A.; Campbell, P. G. C.; Bisson, M. Sequential extraction procedure for the speciation of particulate trace metals. *Anal. Chem.* **1979**, *51* (7), 844–851; DOI: 10.1021/ac50043a017.
- (26) Abraitis, P. K.; Patrick, R. A. D.; Vaughan, D. J. Variations in the compositional, textural and electrical properties of natural pyrite: a review. *Int. J. Miner. Process.* **2004**, *74* (1–4), 41–59; DOI: 10.1016/j.minpro.2003.09.002
- (27) Blanchard, M.; Alfredsson, M.; Brodholt, J.; Wright, K.; Catlow, C. R. A. Arsenic incorporation into FeS₂ pyrite and its influence on dissolution: A DFT study. *Geochim. Cosmochim. Acta* **2007**, *71* (3), 624–630; DOI: 10.1016/j.gca.2006.09.021.
- (28) Swanson, V. E. *Geology and geochemistry of uranium in marine black shales--A review*; Professional Paper; USGS Numbered Series 356-C; 1961.
- (29) Gott, G. B. Inferred relationship of some uranium deposits and calcium carbonate cement in southern Black Hills, South Dakota; USGS Numbered Series 1046-A; U.S. Govt. Print. Off., 1956. <http://pubs.usgs.gov/bul/1046a/report.pdf>.
- (30) Hajnos, M. *Buffer Capacity of Soils*. Encyclopedia of Agrophysics; Springer Netherlands, 2011; pp 94–95.
- (31) Tesoriero, A. J.; Pankow, J. F. Solid solution partitioning of Sr²⁺, Ba²⁺, and Cd²⁺ to calcite. *Geochim. Cosmochim. Acta* **1996**, *60* (6), 1053–1063; DOI:10.1016/0016-7037(95)00449-1.
- (32) Abraitis, P. K.; Patrick, R. a. D.; Kelsall, G. H.; Vaughan, D. J. Acid leaching and dissolution of major sulphide ore minerals: processes and galvanic effects in complex systems. *Mineral. Mag.* **2004**, *68* (2), 343–351; DOI: 10.1180/0026461046820191.

- (33) Zhang, T.; Gregory, K.; Hammack, R. W.; Vidic, R. D. Co-precipitation of Radium with Barium and Strontium Sulfate and Its Impact on the Fate of Radium during Treatment of Produced Water from Unconventional Gas Extraction. *Environ. Sci. Technol.* **2014**, *48* (8), 4596–4603; DOI: 10.1021/es405168b.
- (34) Zhang, Y. *Geochemical Kinetics*; Princeton University Press, 2008.
- (35) Renock, D.; Landis, J. D.; Sharma, M. Reductive weathering of black shale and release of barium during hydraulic fracturing. *Appl. Geochem.* **2016**, *65*, 73–86; DOI: 10.1016/j.apgeochem.2015.11.001.

Chapter 3

Impact of Carbonate Dissolution on Arsenic Release during Shale Gas

Extraction

3.1 Introduction

Shale gas extraction by hydraulic fracturing targets organic-rich shale formations that are typically found more than 1 km below the surface. These formations are usually hundreds of millions of years old and serve as sinks of minor elements such as toxic metals and radionuclides including U and Th.¹⁻⁸ Such elements are often concentrated by precipitation, adsorption and complexation to the clay minerals and organic matter within the shale. When highly reduced shales are exposed to the acidic, oxic and saline fracturing fluids, the solid bound metals and radionuclides can be subsequently mobilized through mineral phase acid dissolution or salinity driven ion exchange processes.^{1,4} Pyrite is a ubiquitous mineral in reducing geological environments including in shale formations and known to incorporate trace elements such as Co, Ni, Se, Au, and commonly As.⁹ When oxidants are introduced with hydraulic fracturing fluids, reduced phases such as pyrite release associated trace metals by oxidative dissolution. Oxidation of pyrite-rich mine tailings leads to acid mine drainage (AMD) and contamination of nearby sediments.¹⁰ Similarly, other metal sulfide solids present in shale can cause water quality impairment when they come in contact with oxygen bearing hydraulic fracturing fluids and release associated metals and radionuclides.

Chemical and hydrologic factors controlling toxic element release from shale minerals during hydraulic fluid-rock interactions can be evaluated by reactive transport models.¹¹ One such model, CrunchFlow, covers a range of geological processes in subsurface environments including reactive contaminant transport, chemical weathering, carbon sequestration, biogeochemical cycling, and water-rock interaction, has been used for this purpose.¹²⁻¹⁷ Zhang et al. (2013) used CrunchFlow to simulate wellbore cement and acid gas ($\text{CO}_2 + \text{H}_2\text{S}$) interaction under geologic carbon sequestration conditions that results in mineral dissolution, porosity change, and the formation of calcite and pyrite.¹² CrunchFlow has also been successfully applied in a study of the oxidation of sulfide minerals in acid rock drainage.¹³ Others have employed more simplified reactive transport models. Offeddu et al.¹⁴ used a 1-D reactive transport model in column studies to assess the efficacy of passive treatment of AMD and find out that Ca released from calcite dissolution, along with the sulfate in solution, led to formation of gypsum coatings on the calcite grain surfaces which eventually prevented calcite dissolution.¹⁴ Deng et al.¹⁸ modeled a rock core containing mainly calcite and dolomite in contact with a CO_2 -acidified brine, and captured the development of an altered layer in the near-fracture region and the progressive decrease in the dissolution rate of the fast-reacting mineral in the altered layer. Cai and Li modeled the accidental release of Marcellus shale produced water into a river and found ion exchange reactions with clay minerals in the sediments likely controlled the rate and maximum concentration of released cations into the river.¹⁹ Wen et al. presented a multicomponent reactive transport model of a fractured rock (quartz, clay, and calcite) in contact with a CO_2 -saturated fluids and implicated the lower abundance of reactive mineral calcite to be the cause of significant alterations of the fractured media.²⁰ This work demonstrated the impact of the mineralogical composition and rate-limiting mineral dissolution reactions in the evolution of the complex fractured rock matrix.

In general, carbonate minerals in shale play an important role in trace element mobilization.²¹ When exposed to acidic fracturing fluids, if sufficient carbonates are present, they may buffer pH near neutral to slightly alkaline values; which tends to minimize element leaching for other mineral phases. However, prior work has shown that carbonates can also serve as a source of trace elements, with carbonate dissolution potentially contributing directly to the elevated concentrations of metals present in produced waters. Batch leaching experiments of shale from Michigan (powdered to maximize leaching) in Chapter 2 demonstrated that maximum element leaching occurs when shale is in contact with an oxidizing, strong acid solution (Appendix B: Figure B1). This included the leaching of arsenic, a known carcinogen and natural groundwater contaminant. Sequential extractions were also completed to determine which phases in the shale contributed to the release of hazardous elements and it was found that ~90% of total arsenic is present within the reduced mineral phases present in the shale. Iron showed similar leaching behavior to arsenic indicating arsenic was released along with iron, likely from pyrite dissolution. As-bearing sulfides are commonly observed in a wide variety of sedimentary environments, often as arsenopyrite (FeAsS) or arsenian pyrite (FeAs_xS_{2-x}).^{22,23}

The present study presents results from a core-flooding study where synthetic hydraulic fracturing fluid was injected through a saw-cut core of the Collinwood formation, which is an organic-rich carbonate that is targeted along with the Utica shale for natural gas production in Michigan. Specifically, this study focused on the impact of fracturing fluid components (e.g., acid, oxidizers) in promoting toxic element (e.g., As) leaching from the Collingwood core sample. Previous leaching study in chapter 2 used pulverized shale samples to maximize the accessibility of major solid phase cations and associated minor elements during well-mixed batch reactor leaching experiments. To better understand the chemical and hydrologic factors controlling major and minor trace element release from an intact rock-matrix, a series of short-

term (hours to days) flow-through leaching experiments were performed on Collingwood shale core samples using representative *in situ* reservoir pressure and temperature. Results from these experiments were used to develop a 2D reactive transport model to explore greater timescales and determine rate-limiting controls on mineral dissolution within the shale matrix.

3.2 Materials and methods

3.2.1 Shale sample and injected hydraulic fracturing fluid

The Collingwood core samples for the flow-through experiments were obtained from the Michigan Geological Repository for Research and Education. The cores came from the St. Allis 2-3 shale play in upper Michigan from a depth of 1.62 km. For the experiments, each core was cut in half lengthwise with a diamond saw to create an artificial fracture flow pathway through the core. Approximate mineralogy of the cores was determined by averaging energy dispersive spectroscopy elemental maps at multiple locations along the exposed fracture surface (Figure B2). This analysis indicated the Collingwood cores were comprised of approximately 60% calcite, 14% illite, 20% quartz, 1% pyrite by volume. A simplified model fracturing fluid was created based on reported compositions of hydraulic fracturing fluids used in Michigan shale gas well completions from data available on fracfocus.org. The synthetic fracturing fluid consisted of 30 mM hydrochloric acid, 1 mM ammonium persulfate, 0.64 mM citric acid, and 10 mM choline chloride.

3.2.2 Flow-through experimental setup

Core-flooding experiments (setup shown in Figure 3.1) were conducted by pumping the synthetic hydraulic fracturing fluids into proppant-packed fractured shale cores (a diameter of 2.54 cm, a length of 3.5 cm) under a representative shale gas reservoir temperature of 34°C with a confining pressure of 20.7 MPa. Sand was spread between the core halves before

recombining the halves and securing them via heat shrink tubing. This procedure created a core with an open channel propped with sand grains similar to an *in situ* hydraulically fracture shale fracture with an aperture approximately equivalent to the diameter of the sand grains (~200 μm). The recombined core was then placed in the core holder and surrounded tightly by a rubber confining jacket. Distilled water was introduced inside the reactor to fill the gap between the rubber jacket and the reactor walls to establish a confining pressure via a high pressure syringe pump (Figure 3.1). Due to the corrosive nature of the synthetic fracturing fluids, they were stored in a floating piston accumulator (FPA) and pumped through the core via controlled volume displacement of the piston with water from a high pressure syringe pump. Two different flow rate schemes were performed: the first experiment (CW#1) was run with a constant flowrate of 2.5 ml/hr for ~32 hr; the second experiment (CW#2) incorporated three sequential flow steps of decreasing flowrate from 10 ml/hr, 5 ml/hr, and 2.5 ml/hr, respectively, for a total reaction time of ~90 hr. Effluent concentrations of selected cations were measured by inductively coupled plasma mass spectrometry (ICP-MS). To assess the evolution of the fracture geometry after exposure to the acidic fluids, the cores were scanned before and after the flow-through experiments using SCANCO medical μCT .²⁴ After the final scanning, the fracture was stabilized by filling the core interior with epoxy resin. The resin-filled cores were then sectioned perpendicular to the fracture plane in several locations (Figure B3) for further analysis by scanning electron microscopy (SEM) and energy dispersive x-ray spectroscopy (EDS) to assess physical and chemical changes along the fracture pathway, respectively.

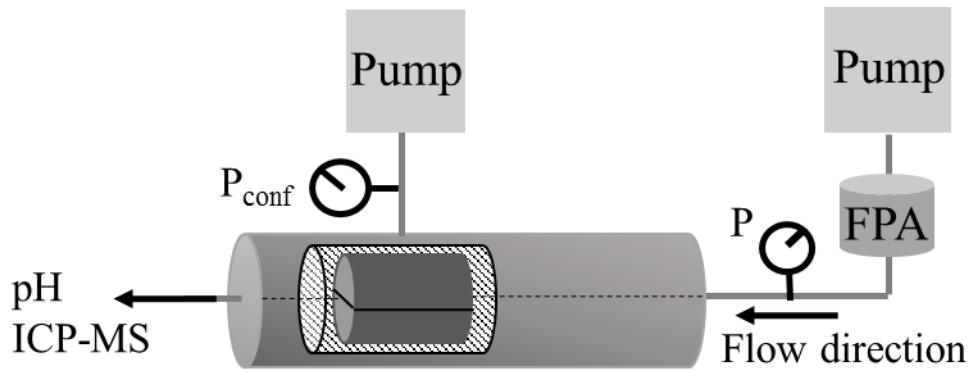


Figure 3.1: Simplified schematic of the flow-through experimental setup

3.2.3 2D reactive transport modeling

A 2D reactive transport model using CrunchFlow^{25,26} was developed to further assess how carbonate dissolution may affect access to less soluble minor mineral phases (such as pyrite) embedded within the carbonate-rich shale matrix and impact subsequent release of elements from these phases (e.g., arsenic and iron from dissolving pyrite). Figure 3.2 illustrates the model domain used for this reactive transport analysis. As shown in Figure 3.2, one half of the core was segmented into a uniform rectangular grid with the cells in the first (bottom) row lined up parallel with the fracture. For model simulations, at time $t = 0$, the fluid was assumed to be simultaneously introduced into the first row of cells across the entire length of the core. Initial shale mineralogy was assumed to be homogenous across all cells except for the fracture channel, which was assumed to have 100% porosity. Based on EDS element mapping of the domain (Figure B2a), the initial mineral volume fractions were assumed to be 60% calcite, 14% illite, 20% quartz, and 1% pyrite, with a porosity of 5%. Note that the localized calcite-rich region identified through X-ray computed tomography (XCT) imaging of the actual core (Figure B2b) was not captured in this model. In addition to the primary mineral phases, siderite, hematite, and goethite were allowed to form as secondary minerals in all cells when their solubility was exceeded, based on the computed pH, dissolved iron and carbonate, and the redox state (i.e., pe) within each cell at a given timestep.

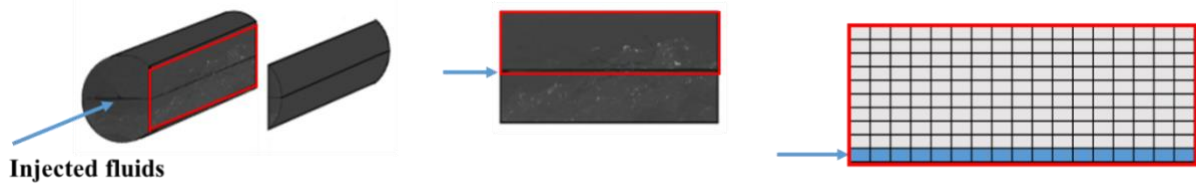
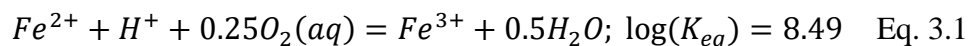


Figure 3.2: Reactive transport model domain

Sequential extraction data (Figure B1 from data in chapter 2), demonstrated that iron is present in both carbonate minerals and pyrite within the shale. For the model simulation reported here, we choose not to include the iron fraction associated with carbonates and assumed that all Fe was extracted from reduced minerals. Jew et al. demonstrated that pyrite is the major source of iron when shale comes into contact with hydraulic fracturing fluids.²⁷ As such and for simplicity, we assumed that iron and arsenic only come from pyrite dissolution. While calcium is released from calcite dissolution under acidic conditions, both acid and an oxidant are needed for any significant release of iron and arsenic by oxidative dissolution of pyrite. To simulate this, $O_2(aq)$ was used as the oxidizing agent in the model input file as a substitute for the actual oxidizer present in the synthetic injected fluids (ammonium persulfate). For the conversion of Fe(II) to Fe(III) during pyrite oxidative dissolution, two different scenarios were tested in CrunchFlow. In one case, rapid oxidation of Fe(II) to Fe(III) by molecular oxygen, with redox pe controlled by the O_2/H_2O couple was assumed (Eq. 3.1). In this scenario Fe(II) from pyrite dissolution is immediately oxidized to Fe(III) and precipitates as goethite, leaving very little Fe in the effluent; however, this scenario is not in agreement with experimental results in which measurable dissolved Fe(II) was present in the effluent.



For the second scenario, a kinetically controlled oxidation of Fe(II) by molecular oxygen was assumed, using the two parallel reactions (one pH dependent and one pH independent) per the rate law proposed by Singer and Stumm:²⁸

$$k_{FeII_oxidation} = 10^{-5.815} a_{H^+}^{-2} a_{Fe^{++}} a_{O_2} + 41.5 a_{O_2} \quad \text{Eq. 3.2}$$

According to Eq. 3.2, when pH is below ~3.5 the oxidation rate of Fe(II) is constant, slow, and independent of pH, but above pH ~4.5 the oxidation rate increases by two orders of magnitude for each unit of pH increase (assuming a P_{O_2} of 0.2 atm).

Chapter 2 demonstrated that carbonate-rich powdered Collingwood samples could substantially neutralize strong pH 2 acid leaching solutions to a pH >5. Similarly, Jew et al.²⁶ recently demonstrated that shale with high carbonate mineral content could substantially buffer pH and significantly enhance the rate of the oxidation of Fe(II) and production of Fe(III) solids. In contrast, the effluent pH in the flow-through experiments of this study never exceeded a pH of 3 due to the short residence time of injected fluids (1 to ~4 minutes under all flow rates) and little to no Fe(II) was oxidized. Because the oxidation of Fe(II) to Fe(III) was negligible and only Fe(II) was found in the effluent, Fe(III) species were not included in the reactive transport modelling. From speciation modelling, $AsH_3(aq)$ and H_3AsO_3 (As(III) species) are expected to be the predominant dissolved arsenic species during pyrite dissolution under the conditions of this study. To include arsenic in the model, the pyrite stoichiometry was modified to include a small percentage of arsenic based on the previous sequential extraction results in chapter 2, with As \approx 0.028 wt% of Fe in pyrite. Under more oxic and mildly acidic conditions, dissolved arsenate species (e.g., As(V) as $H_2AsO_4^-$) predominate.

The CrunchFlow model was calibrated by adjusting the cementation exponent and mineral surface area to best-fit the effluent profiles from the CW#1 and CW#2 experiments (viz., effluent calcium, iron, and arsenic concentration profiles, and the pH profile as a function of time). The value of the cementation exponent ($m = 1.6$) is in line with previous values used for this parameter ($m = 1.3 - 2.5$).^{29,30} CrunchFlow calculates an effective diffusion coefficient, D_{eff} , based on porosity according to Archie's law ($D_{eff} = \frac{D_0}{\phi^{-m}}$, ϕ is formation porosity, D_0 is initial diffusion coefficient); dispersion is neglected in this model. Similar to Heidari et. al.³¹,

the specific surface area for minerals embedded in the shale used in this study was set to be 1–3 orders of magnitude smaller than surface area values measured for powdered minerals³¹ (shown in Table 3.1). Heidari et. al. found the reactive surface area of embedded minerals could be smaller due to the lack of accessibility of the minerals to the leaching fluids compared to powdered samples. The impact of different flowrates on the effluent profile from the CW#2 experiment was also fit by model parameter adjustment. To account for the initial rapid increase in the Ca concentration profile, 1–5% calcite was assumed present in the fracture cells as an initial condition. The initial Ca pulse in the effluent is believed to be associated with flushing of loosely attached calcite particles when the core was exposed to the confining pressure for the first time. According to the model porosity estimates, the inclusion of 1–5% initial calcite in the fracture channel captured well the changes in fracture morphology (i.e., widening of fracture aperture) associated with rapid initial calcite dissolution. The final calibrated model parameters used in all the simulation are shown in Table 3.1. Mineral dissolution rates were obtained from published experimental data.³²

Table 3.1: CrunchFlow model parameters

Flowrate		10ml/hr, 5ml/hr, or 2.5ml/hr		
pH		1.9		
O ₂ (aq) in injected fluids		8×10^{-4} M		
Porosity		5%		
Domain mineralogy		60% calcite, 14% illite, 20% quartz, 1% pyrite		
Mineral surface area	Mineral	Literature range (m ² /g) ^b	used in this model (m ² /g)	used in Heidari's model (m ² /g) ^b
	illite	$42 - 1.37 \times 10^2$ ^c	5.8	6.5
	Calcite	$0.0038 - 7.65$ ^a	0.002	
	pyrite	$5.0 \times 10^{-2} - 2.3$ ^d	0.01	0.002
	quartz	$1.0 \times 10^{-3} - 2.3$ ^e	0.2	0.001
Mineral reaction-rate law ³²		$k_{calcite} (mol/m^2/s) = 10^{-0.3} a_{H^+} + 10^{-5.81}$ $k_{pyrite} (mol/m^2/s) = 10^{-7.52} a_{H^+}^{-0.5} a_{Fe^{3+}}^{0.5} + 10^{-4.55} a_{O_2}^{0.5}$ $k_{quartz} (mol/m^2/s) = 10^{-13.4}$ $k_{illite} (mol/m^2/s) = 10^{-12.75} a_{H^+}^{-0.16}$ $k_{siderite} (mol/m^2/s) = 10^{-3.19} a_{H^+}^{0.5} + 10^{-8.9}$ $k_{hematite} (mol/m^2/s) = 10^{-9.39} a_{H^+} + 10^{-14.6}$ $k_{goethite} (mol/m^2/s) = 10^{-7.94}$		
$R_m = A_m k \left(1 - \frac{Q}{K_{eq}}\right)$				

Effective diffusion: $D_{eff} = \frac{D_0}{F} = \frac{D_0}{\phi^{-m}}$	Parameter	Calibrated value
	Diffusion coefficient D_0	$10^{-9} \text{ m}^2/\text{s}$
	Cementation exponent m	1.6
	Porosity ϕ	5%

- a** Subhas, A. V.; Rollins, N. E.; Berelson, W. M.; Dong, S.; Erez, J.; Adkins, J. F. A Novel Determination of Calcite Dissolution Kinetics in Seawater. *Geochim. Cosmochim. Acta* **2015**, 170, 51–68.
- b** Heidari, P.; Li, L.; Jin, L.; Williams, J. Z.; Brantley, S. L. A Reactive Transport Model for Marcellus Shale Weathering. *Geochim. Cosmochim. Acta* **2017**, 217, 421–440
- c** Köhler, S.J., Dufaud, F. and Oelkers, E.H.. An experimental study of illite dissolution kinetics as a function of pH from 1.4 to 12.4 and temperature from 5 to 50 C. *Geochimica et Cosmochimica Acta*, **2003**, 67(19), pp.3583-3594.
- Bibi, I., Singh, B. and Silvester, E., Dissolution of illite in saline–acidic solutions at 25 C. *Geochimica et Cosmochimica Acta*, **2011**, 75(11), pp.3237-3249.
- Suzuki-Muresan, T., Vandenborre, J., Abdelouas, A. and Grambow, B., Solution controls for dissolved silica at 25, 50 and 90° C for quartz, Callovo-Oxfordian claystone, illite and MX80 bentonite. *Physics and Chemistry of the Earth, Parts A/B/C*, **2011**, 36(17-18), pp.1648-1660.
- d** Kameia, G. and Ohmotob, H., The kinetics of reactions between pyrite and O₂-bearing water revealed from in situ monitoring of DO, Eh and pH in a closed system. *Geochimica et Cosmochimica Acta*, **2000**, 64(15), pp.2585-2601.
- Kuechler, R. and Noack, K., Comparison of the solution behaviour of a pyrite–calcite mixture in batch and unsaturated sand column. *Journal of contaminant hydrology*, **2007**, 90(3-4), pp.203-220.
- Liu, R., Wolfe, A.L., Dzombak, D.A., Stewart, B.W. and Capo, R.C., Comparison of dissolution under oxic acid drainage conditions for eight sedimentary and hydrothermal pyrite samples. *Environmental geology*, **2008**, 56(1), pp.171-182.
- Truche, L., Berger, G., Destrigneville, C., Guillaume, D. and Giffaut, E., Kinetics of pyrite to pyrrhotite reduction by hydrogen in calcite buffered solutions between 90 and 180 C: Implications for nuclear waste disposal. *Geochimica et Cosmochimica Acta*, **2010**, 74(10), pp.2894-2914.
- e** Bennett, P.C., Melcer, M.E., Siegel, D.I. and Hassett, J.P., The dissolution of quartz in dilute aqueous solutions of organic acids at 25 C. *Geochimica et Cosmochimica Acta*, 52(6), **1988**, pp.1521-1530.
- Brady, P.V. and Walther, J.V., Kinetics of quartz dissolution at low temperatures. *Chemical geology*, **1990**, 82, pp.253-264.
- House, W.A. and Orr, D.R., Investigation of the pH dependence of the kinetics of quartz dissolution at 25 C. *Journal of the Chemical Society, Faraday Transactions*, **1992**, 88(2), pp.233-241.

In CrunchFlow, the governing advection-diffusion-reaction equation for the rate of change in the total molar concentration of species i (C_i) is expressed as:^{18,33}

$$\frac{\partial(\phi C_i)}{\partial t} = -\nabla \cdot (\mathbf{u}\phi C_i) + \nabla(\phi \mathbf{D}\nabla C_i) - \sum_m v_{i,m} R_m \quad \text{Eq. 3.3}$$

where ϕ is the porosity, C_i is the concentration of a species i (mol/kg H₂O) in solution, \mathbf{u} is the Darcy flux (ms⁻¹), R_m is the total reaction rate (mol-m⁻³s⁻¹) of species i in solution and \mathbf{D} is the combined dispersion-diffusion coefficient (m²s⁻¹), R_m is the mineral m dissolution/precipitation rate (mol-m⁻³s⁻¹), and $v_{i,m}$ is the stoichiometric coefficient of species i in the reaction of mineral m .

Per Eq. 3.3, the rate of change in mass for each component can be expressed as a function of advection, combined dispersion-diffusion and mineral reaction terms, respectively.

The specific rate law parameters used for each mineral in the rate term calculations are shown in Table 3.1. The mineral dissolution/precipitation rate laws are generally expressed as:

$$R_m = A_m \sum_{terms} k_{m,T} a_{H^+}^{n_{H^+}} \left(\prod_i a_i^{n_i} \right) \left(1 - \frac{Q}{K_{eq}} \right) \quad \text{Eq. 3.4}$$

where A_m is the mineral surface area (m^2m^{-3}), $k_{m,T}$ is the reaction rate constant at a specific temperature ($\text{mol}\cdot\text{m}^{-2}\text{ s}^{-1}$), $a_{H^+}^{n_{H^+}}$ is the term describing the effect of pH on the rate, $a_i^{n_i}$ is the term describing a catalytic/inhibitory effect on the rate by another species, Q is the ion activity product, and K_{eq} is the reaction equilibrium constant. The summation term indicates that several parallel rate laws may be used to describe the dependence of a given reaction rate on pH or on other species.

In order to evaluate the relative importance of these three terms (advection, diffusion, reaction), non-dimensional parameters including Péclet number (Pe) and Damköhler numbers (Da) can be applied. Following Steefel et al.³³, the Pe and Da numbers are defined as:

$$Pe_{grid} = \frac{v\Delta x}{D} \quad \text{Eq. 3.5}$$

$$Da_{I_{grid}} = \frac{Ak\Delta x}{\phi v C_{eq}} \quad \text{Eq. 3.6}$$

$$Da_{II_{grid}} = \frac{Ak\Delta x^2}{\phi D C_{eq}} \quad \text{Eq. 3.7}$$

where Δx refers to the grid spacing at any particular point in space, v is local flow velocity, and D is the diffusion coefficient, A is the mineral surface area (m^2m^{-3}), k is the reaction rate constant ($\text{mol}\cdot\text{m}^{-2}\text{ s}^{-1}$), C_{eq} is the solubility of the mineral in moles m^{-3} .

The dimensionless grid Péclet number (Eq. 3.5) can be used to assess the relative importance of advection vs. diffusion. When the Péclet number is $\gg 1$, the advection term in the numerator dominates, while for Péclet numbers $\ll 1$, diffusion is the dominant mass transport process. Dissolution of minerals like calcite can lead to an increase of porosity and

the effective diffusion (D_{eff}) coefficient. Similarly, the flow velocity adjusts to changes in the flow path, which is affected by permeability changes as minerals dissolve.

The relative significance of the advection vs. mineral reaction rates can be expressed using the Damköhler number Da_I (Eq. 3.6). A different Damköhler number, Da_{II} (Eq. 3.7) describes the relative importance of diffusion vs. mineral reaction rate. For Damköhler numbers $\gg 1$, the reaction rate term is much greater than the transport term for a given length scale. A large Damköhler number indicates that mass transport is the rate limiting process compared to mineral reaction kinetics. A smaller Damköhler number implies that mass transport is the more rapid process and therefore reaction kinetics is the rate limiting process controlling mineral dissolution and precipitation.

When advection can be neglected compared to diffusion or chemical kinetics, rate expressions can be derived to assess the relative importance of surface-controlled reaction rates (Eq. 3.8) vs. diffusion-controlled reaction rates (Eq. 3.9).^{18,34}

$$R_{surf} = -k_{surf}A_{rxn}\left(1 - \frac{Q}{K_{eq}}\right) \quad \text{Eq. 3.8}$$

where k_{surf} is the surface-controlled rate constant, A_{rxn} is the reactive surface area.

$$R_{diff} = -k_{diff}A(C_{eq} - C_{bulk}) = -\frac{D_{eff}}{L}A(C_{eq} - C_{bulk}) \quad \text{Eq. 3.9}$$

where k_{diff} is the diffusion-controlled rate constant, A is the fracture surface area, C_{eq} is equilibrium concentration, C_{bulk} is the bulk concentration in the fracture, L is the thickness of the altered layer.

For a mixed kinetic control,³⁴ an appropriate overall reaction rate constant can be derived (Eq. 3.10) with parameters as previously defined. The combined rate equation demonstrates that the slower rate will always dominate and control the overall reaction rate.

$$R = -kA(C_{eq} - C_{bulk}) = 1/\left(\frac{1}{R_{diff}} + \frac{1}{R_{surf}}\right) \quad \text{Eq. 3.10}$$

When $k_{surf} > k_{diff}$, the mineral reaction will be mass transport-controlled, while for $k_{surf} < k_{diff}$, the mineral surface reaction will control the overall reaction rate according to Eq. 3.11:

$$k = 1 / \left(\frac{1}{k_{diff}} + \frac{1}{k_{surf}} \right) \quad \text{Eq. 3.11}$$

where k is the mixed kinetic rate constant, and R is the mixed kinetic rate law.

3.3 Results and discussion

3.3.1 Flow-through experiment effluent chemistry

Effluent profiles for pH, Ca, Fe, and As concentrations from the CW#2 experiment are shown in Figure 3.3 (CW#1 results are provided in Appendix B: Figure B7). As shown in Figure 3.3, when strongly acidic injection fluids (initial pH ~1.9) were pumped through the Collingwood core, the effluent pH increased to a pH value between ~2-3, depending on the flowrate (2.5 ml/hr, 5 ml/hr, 10 ml/hr). Even though the Collingwood core has abundant calcite (~60%), the short hydraulic residence time and limited exposure of the injected fluids to calcite beyond the main fracture pathway led to ineffective buffering by the shale and only small pH increase.

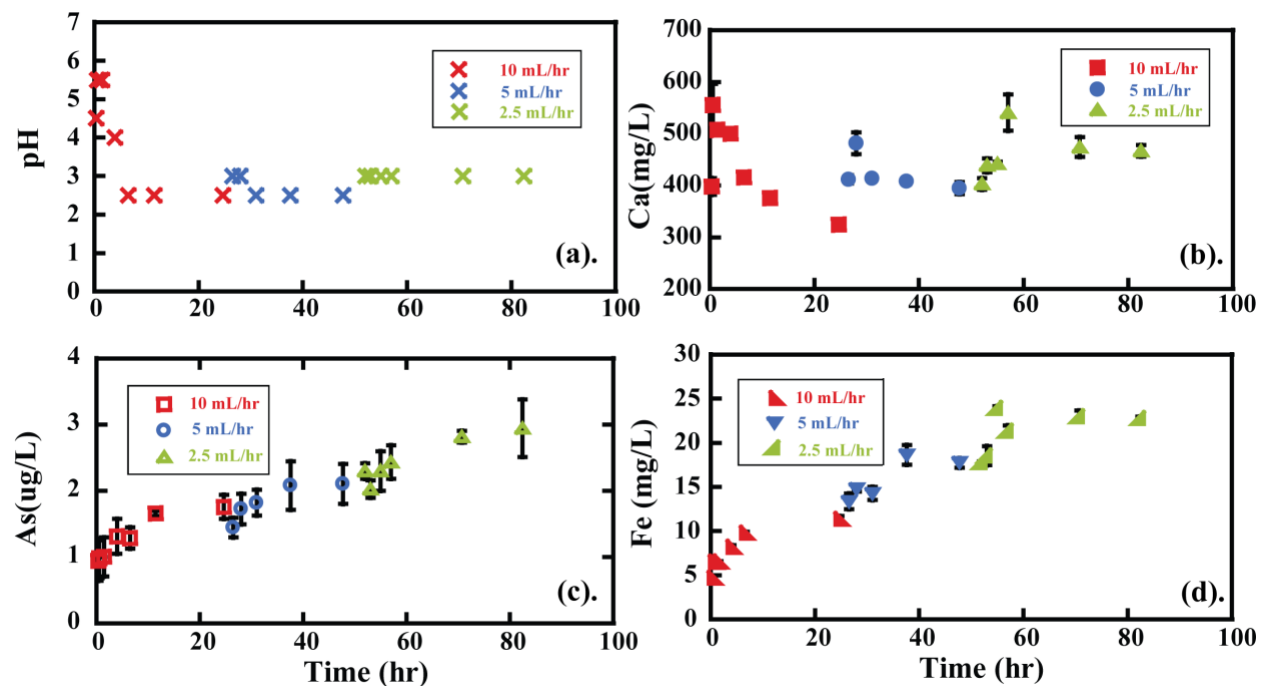


Figure 3.3: Effluent pH, calcium, iron, and arsenic concentrations as a function of time for flow-through experiment CW#2. Red, blue, and green symbols represent experimental data for flowrates of 10 ml/hr, 5 ml/hr, and 2.5 ml/hr, respectively.

For each flow rate change in CW#2, the effluent Ca concentration had a short rapid increase before diminishing (Figure 3.3b). The initial Ca spike suggests either the release of detachable and rapidly dissolving calcite particles or a pulse of dissolved Ca from the pores adjacent to the main fracture channel at the initiation of each flowrate change. After the short initial spike in Ca concentration, the rate of Ca leaching decreases with time as calcite dissolution becomes mass transport limited. As shown in Figure 3.3c and d, As and Fe concentration continuously increased in CW#2, regardless of the flowrate, with each approaching a plateau value. Pyrite dissolution is the likely source of Fe and As. Eventually, as pyrite dissolution and diffusion from small pores reach steady state, the Fe and As effluent concentration level off at the lowest flowrate. In general, slower flowrates led to higher pH and Ca, Fe, and As concentrations (Figure 3.3). This is attributed to the longer hydraulic residence time allowing for greater pH buffering and more time for calcite and pyrite to dissolve and Ca, As, and Fe to diffuse into the main channel.

A comparison of the effluent concentration profiles of Ca, Fe and As in Figure 3.3 shows much greater Ca release compared to As and Fe. This is consistent with the greater shale calcite content and its faster rate of dissolution compared to pyrite. The rapid depletion of calcite in direct contact with the main fluid flow channel leads to the creation of depleted regions adjacent to the main fracture (shown as altered layers in Appendix B: Figure B4, B5, B6) where more slowly dissolving minerals like clays and quartz remain largely intact. When calcite becomes significantly diminished in these depleted areas, calcite dissolution slows and the effluent dissolved Ca concentration begins to decrease. During this time, pyrite dissolution continues to increase, leading to increasing Fe and As effluent concentrations. As and Fe

effluent concentrations eventually reach steady-state, likely a result of a combination of slow kinetics of pyrite dissolution and slow diffusion of As and Fe from the smaller pores created in the altered region into the main flow channel. In this way, faster and greater calcite dissolution serves as the major driver for enhancing the accessibility of the more slowly dissolving minerals like pyrite within the calcite-rich matrix.

3.3.2 Image analysis results

A combination of XCT and SEM analyses were conducted before and after the ~32 hr CW#1 flow-through experiment to further identify the rate limiting processes controlling the dissolution of secondary minerals embedded in carbonate-rich shale. Figure 3.4a illustrates the evolution of preferential dissolution pathways formed adjacent to the main fracture channel and surrounding regions (represented by the orange rectangle in the figure). As shown, an expanding altered layer forms with the appearance of widening fractures adjacent to the preferential flow path. Post-experiment XCT/SEM images and EDS mapping of two of the growing fractures are shown in Figures 3.4b1 and 3.4b2. Figure 3.4b1 shows a calcite-depleted region and exposure of embedded minerals within the dissolving calcite matrix including quartz, clay, and pyrite (see also Appendix B: Figure B4, Figure B5) within the dissolving calcite matrix. Figure 3.4b2 shows another depleted calcite region from a smaller fracture emanating from the main fluid flow channel. Once again, the rapidly dissolving calcite exposes the more slowly-dissolving minerals like pyrite (per Fe/As profiles in Figure 3.3c, d; and dissolution rates in Table 3.1). As calcite depletion continues, the remaining minerals in the depleted zones limit rapid access to fresh calcite regions within the core, which ultimately causes effluent Ca concentration to decrease (Figure 3.3b). In turn, acid driven calcite dissolution becomes increasingly controlled by the diffusive transport of the acid into and the reaction products out of the porous altered region. In contrast, exposure of embedded Fe/As

bearing minerals (e.g., arsenopyrite) increase, and both Fe and As effluent concentrations increase with time (Figure 3.3c, d). Due to the relatively slower rate of acid driven oxidative dissolution of pyrite-like minerals, the leaching rate ($\sim 10^{-7}$ mol/m²/s) is likely controlled by a combination of a surface chemical dissolution reaction and diffusive transport of As and Fe into the main flow channel until a steady-state of mass flow in the effluent is achieved.

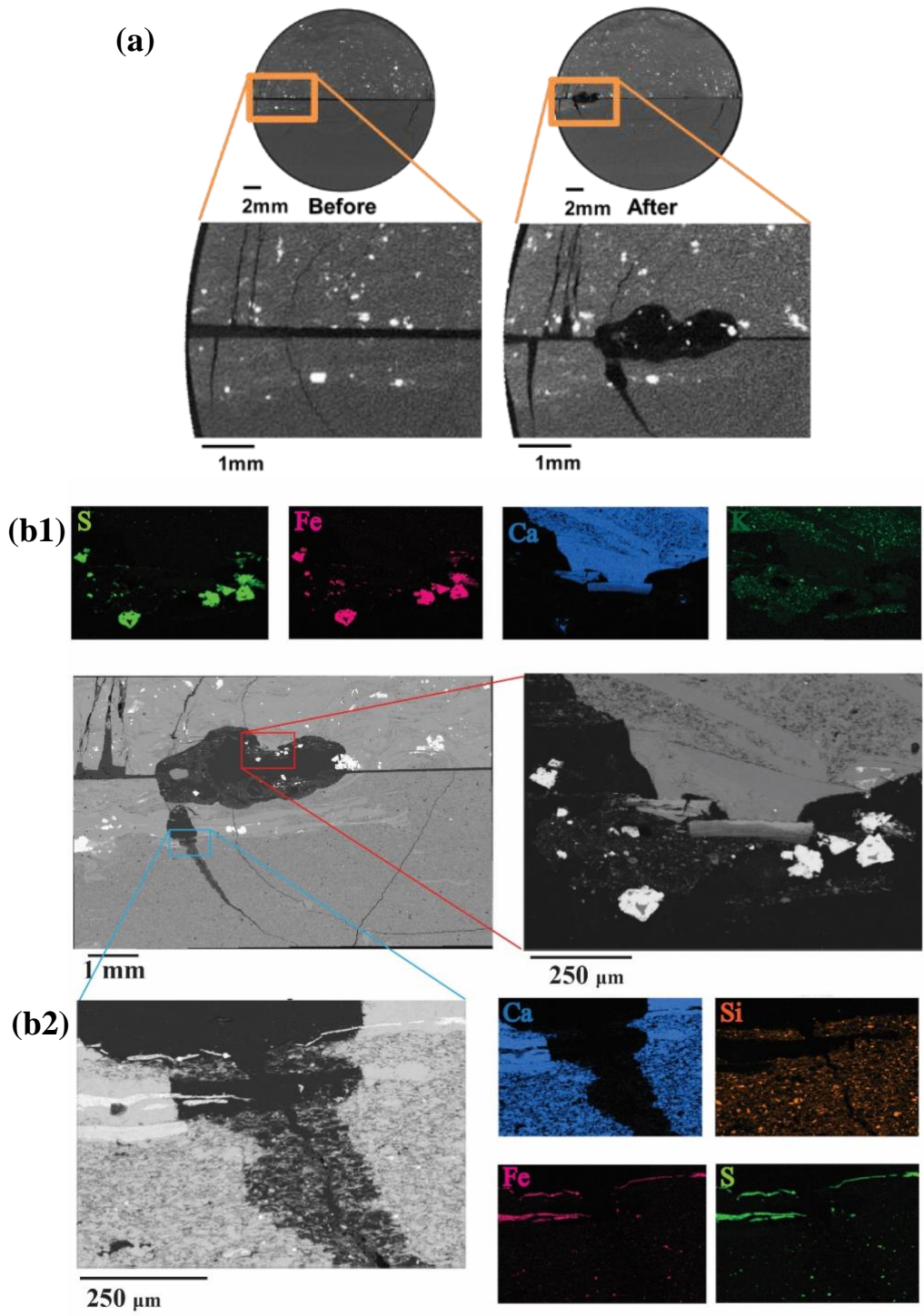


Figure 3.4: Combined XCT (a) and SEM image analysis (b1 and b2) of dissolving fracture pathway cross section. Energy dispersive spectroscopy was used for element mapping.

Although SEM images and element mapping show increasing exposure of the clay matrix and pyrite grains following significant calcite dissolution, the impacts and amount of surface area of pyrite exposed during calcite dissolution remains to be quantified. An attempt to do this is presented in the reactive transport modelling section that follows. The model is capable of providing estimates of reactive surface area changes of slowly dissolving minerals in contact with fluids from the faster calcite mineral dissolution (like pyrite exposure from calcite dissolution). From these estimates, surface-area normalized dissolution reaction rates for calcite and pyrite can be quantified, as well as the cause and effects of increasing mineral contact with the flowing fluid phase through a model sensitivity analysis.

3.3.3 CrunchFlow reactive transport model calibration

As mentioned previously, the CrunchFlow reactive transport model was calibrated using the effluent concentration results for pH and Ca, Fe, and As concentration profiles from the CW#1 and CW#2 experiments. Although real shale formations are heterogeneous in rock properties like porosity and mineralogy (Figure B14), a homogenous shale core was assumed as the model domain for simplicity, with the main goal to capture key cause and effect relationships among reactive transport processes. To this end, the model calibration was focused on matching the effluent concentration profiles as a function of changing flow conditions. Although a rigorous “best-fitting” of the experimental effluent data was not the primary objective, an attempt was made to capture the major effluent concentration trends through model parameter adjustments. Most of the calibration focused on representing well the CW#2 effluent data since it had both variable flow and pH changes within the experimental

run. Subsequently, the calibrated model was used to simulate CW#1 effluent data for Ca, Fe, and As. Although no effluent pH data was collected during the single flow CW#1 experimental run, the pH was calculated as function of time and showed similar trends to the CW#2 for a similar flow rate.

The calibrated model simulations matched reasonably well the overall concentration profiles for both CW#2 and most of the CW#1 data (Appendix B: Figure B8). In the case of CW#1, the Ca concentration profile data matched up well with the model results, but the Fe profile was not as well matched, especially for the beginning times compared with the experimental results in which Fe showed an initial spike similar to Ca. The differences between the model predictions and the experimental effluent Fe concentrations at the early times were thought to be due to an initial carbonate release (not captured by the model reactions) at the beginning of the flow initiation leading to a concomitant initial spike of dissolved Fe within the calcite (consistent with the sequential extraction results for the Collingwood core shown in Figure B1). In contrast, the model simulation under predicted the effluent As concentration at later times. Arsenic effluent concentration predictions depend on the amount of pyrite specified and the assumed concentration of arsenic incorporated within pyrite. Since the model cannot account for non-homogenous distributions of As within pyrite minerals and the pyrite itself may be unevenly distributed within the core, this could cause the model to under predict As release.

To simulate the impact of sequential and decreasing flowrate changes on effluent concentrations in CW#2 experiments, the component masses in each cell at the end of each flowrate simulation were used as the initial condition for each subsequent flowrate change. By doing this, the model was able to capture well the experimental effluent data trends with flowrate change (Figure B8). As in the case for CW#1 simulations, slight differences between

the calibrated model simulations and the actual effluent concentrations of Ca, Fe, and As and pH profiles from CW#2 were found and could have been due to shale mineral heterogeneity.

Longer-term simulations were also run to further enhance the applicability of the simulations to field time-scales (discussed below). While it is recognized that a model calibrated against short hydraulic residence times and laboratory-scale flow-through experiments may miss longer time and larger spatial scale processes present in the field, the model calibrated at shorter times and laboratory spatial scales can be used to inform about general trends in effluent concentration that may occur at larger length when the rate limiting processes controlling mineral dissolution may change as the thickness of the calcite depleted regions extend further into the shale matrix away from the main flow channel fracture.

3.3.4 Model results and discussion

The 2D reactive transport model developed in CrunchFlow was used to simulate the mobilization of trace elements from the carbonate-rich Collingwood fractured core sample exposed to a strong acid injection fluid. The modelling results for a flowrate of 10 ml/hr are discussed here. Based on the image analysis (Figure B6) and modelling results discussed above, the formation of a depleted calcite altered layer is thought to be the primary basis for the trends observed in changing effluent concentrations of Ca, Fe, As and pH as a function of time. Figure 3.5a and b illustrate a conceptual model of the formation of two types of altered layers during a core-flooding experimental run. During early times of the simulation, the injected fluid flows primarily through the main fracture channel (Figure 3.5a). As shown in Figure 3.5b: as calcite begins to dissolve, an altered layer, designated as “*i*”, begins to form with calcite content that varies from an initial content of 60% by volume down to 0%; when calcite becomes fully depleted in a given cell, an altered layer designated as “*ii*” with a constant porosity of 65% is formed; as the porosity reaches 65%, a substantial increase in permeability and advective flow

may result. SEM images together with post reaction XCT (Appendix B: Figure B4, B5d, B6) verify the formation of calcite-depleted layers. In Figure 3.5c, the model-estimated thickness of layer i first increases and then levels off demonstrating calcite dissolution first leads to increasing exposure of calcite up to ~ 50 hr but then reaches a steady-state thickness. This is consistent with calcite dissolution rate kinetics controlling Ca effluent concentration initially until diffusive transport takes over at longer times. In contrast, the altered layer ii thickness continues to increase as the calcite in layer i becomes completely depleted and is converted into layer ii with a porosity of 65%. Figure 3.5c shows the change in average thickness of the two altered layers over time. The continuous increase in the thickness of altered layer ii leads to greater exposure of pyrite within the shale (results shown in Table 3.2). Table 3.2 also demonstrates that the total reactive pyrite area is mainly contributed by pyrite area inside altered layer ii after ~ 100 hr, which means pyrite inside layer ii can represent total pyrite dissolution after ~ 100 hr. This observation is used in the following discussion.

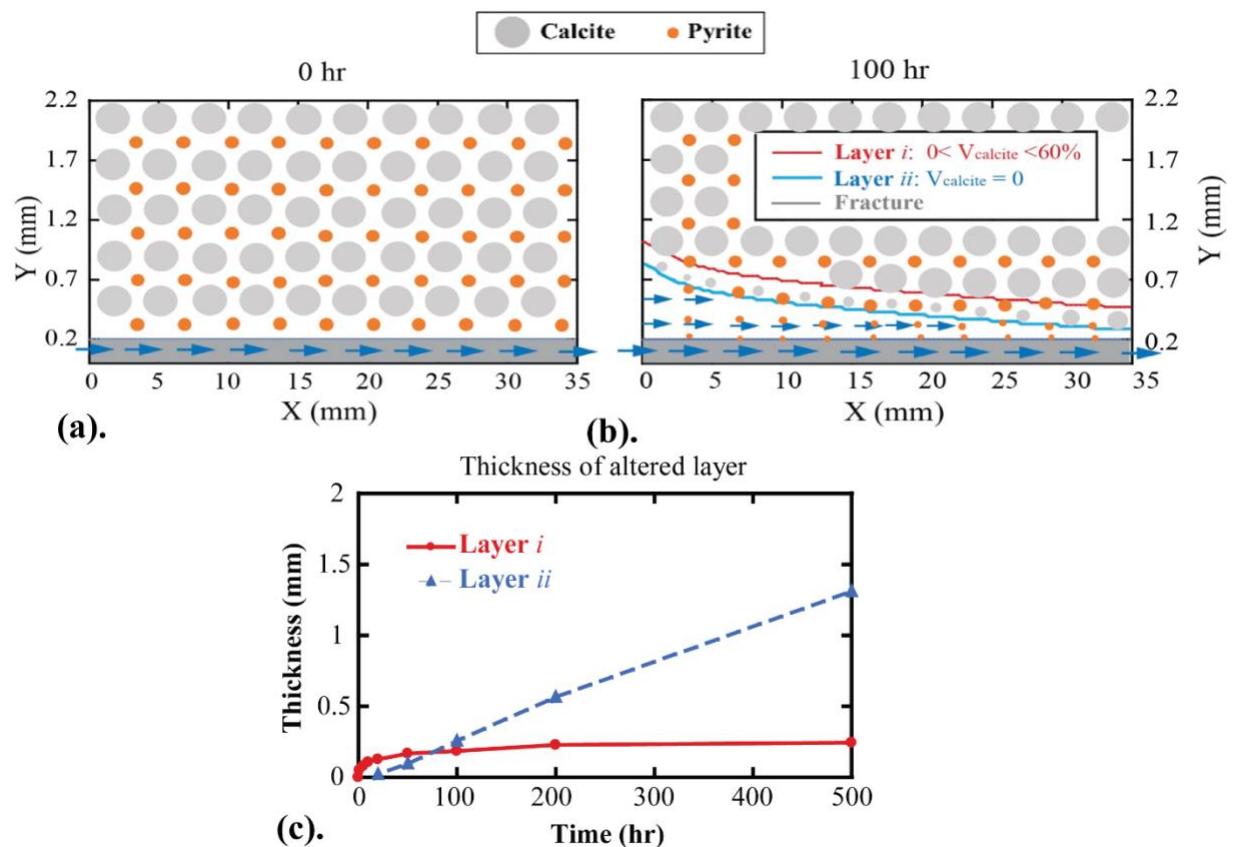


Figure 3.5: Altered layer formation schematics: (a) Initial domain condition with no altered layers at 0 hr; (b) Final domain condition with altered layers adjacent to flow path at 100 hr. The blue area indicates the fracture channel, while grey circles represent calcite and orange circles represent pyrite. Blue arrows symbolize fluid flow through the domain. (c) Thickness of altered layer *i* and layer *ii* as a function of time.

Table 3.2: Summary of pyrite mineral surface area.

Time (hr)	Reactive pyrite area (m ²)	Pyrite area inside layer <i>ii</i> (m ²)	$\frac{\text{pyrite area inside layer } ii}{\text{total reactive pyrite area}}$ (%)
30	0.000191	9.89E-05	52
50	0.000360	0.000215	60
100	0.000554	0.000417	75
200	0.000576	0.000576	100
500	0.00166	0.00166	100

As mentioned previously, the Péclet number describes the relative importance of advective vs. diffusive transport. The averaged grid-scale Pe number for all model cells inside altered layers *i* and *ii* were calculated according to Eq. 3.5 (with individual Pe numbers shown in Figure B9) and are plotted as a function of time in Figure 3.6. In the first ~10 hrs of the simulation, the Pe numbers in the grid cells of altered layer *i* are < 1 indicating diffusion dominates mass transport in and out of the cells. As the porosity increases in layer *i*, mass transport becomes advection-dominated after the first few hours (10 to ~150 hr) as indicated by the Pe numbers > 1 . After ~20 hr, the Pe number inside altered layer *i* begins to decrease with time with the concomitant development of the calcite-depleted region, layer *ii*. The reduction in Pe number towards 1 indicates the increasing importance of diffusive transport compared to advection at later times. After ~150 hr, the thickness of layer *i* levels off as the Pe number decreases to < 1 . This further reduction in the Pe number indicates diffusion becomes the dominant mass transport process controlling calcite dissolution inside layer *i* as the layer

attains a steady-state thickness. Figure 3.6 also shows the Pe number in layer *ii* continuously decreases throughout the simulation and approaches a value of 1 where both diffusion and advection are of equal importance. As expected, the Pe numbers of layer *ii* grid cells are always larger than layer *i* due to the larger porosity of layer *ii* ($\phi = 65\%$ by definition and devoid of calcite) compared to layer *i* ($5\% < \phi < 65\%$).

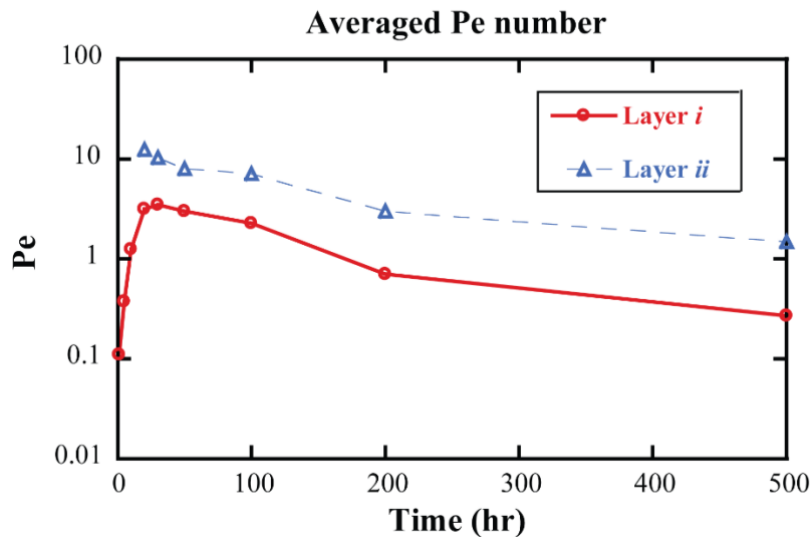


Figure 3.6: Averaged Péclet number of cells inside altered layer *i* and *ii*.

The relative significance of the advection/mineral reaction rate and diffusion/mineral reaction rate can be expressed using Da_I in Eqn. 3.6 and Da_{II} in Eqn.3.7, respectively (Figure B10). For calcite dissolution both Da_I and Da_{II} for altered layer *i* are $\gg 1$, as shown in Figure 3.7b. These large Damköhler numbers indicate that calcite dissolution kinetics is much faster than rate of mass transport. Since the slowest rate term determines the overall mineral dissolution rate, the two large Damköhler numbers indicate calcite dissolution is primarily controlled by mass transport. The grid-specific Da values (Figure B10) are larger and cover a wider range for calcite dissolution in layer *i* ($Da_{I, 500hr} = 10^{-3}$ to 10^9 ; $Da_{II, 500hr} = 10^{-3}$ to 10^6) compared to pyrite dissolution in layer *ii* ($Da_{I, 500hr} = 0.1$ to 10^3 ; $Da_{II, 500hr} = 0.1$ to 10^4). The range of Da values at different time steps are given in Table 3.3. In layer *i*, the high value of

the Da numbers for both calcite and pyrite indicate that diffusive mass transport is controlling their dissolution rates in this layer. Since region *i* has lower porosity compared to layer *ii*, mass transport controls the dissolution rate in this region for both calcite and pyrite. However, in layer *ii*, which is completely depleted of calcite, there are regions where slow pyrite dissolution kinetics is demonstrated to be the rate limiting process controlling pyrite dissolution (layer *ii*: $Da_{I, 500hr} = 0.1$ to 10^3 ; $Da_{II, 500hr} = 0.1$ to 10^4). After ~100hr of flow, nearly all of the reactive pyrite is present within the layer *ii* revealing that pyrite dissolution is influenced by both mass transport and surface chemical dissolution processes. The overall high Da numbers for calcite dissolution in most grid cells, indicate mass transport primarily controls dissolution rates.

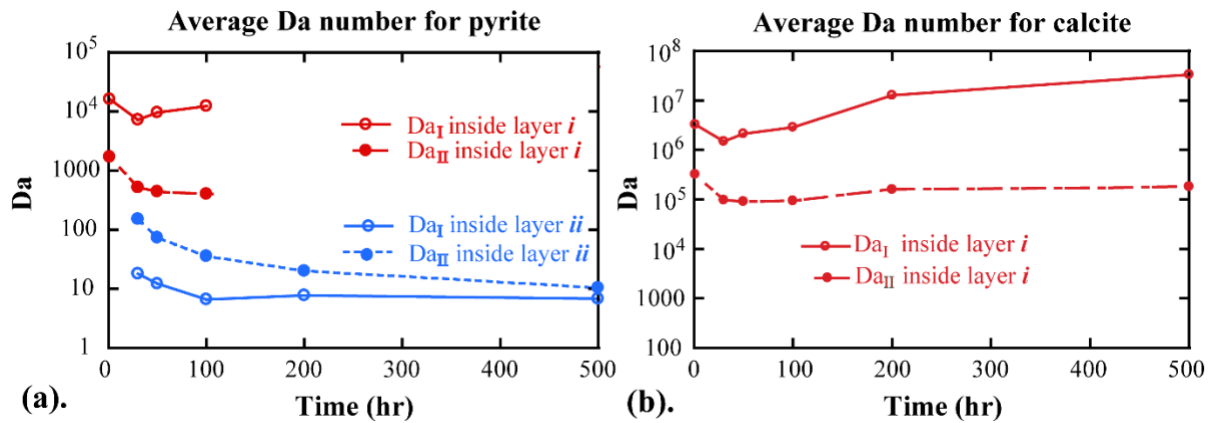


Figure 3.7: (a) Damköhler numbers for pyrite dissolution in altered layer *i* and *ii*; (b) Damköhler number for calcite dissolution in altered layer *i*.

Table 3.3: Ranges of Da_I , Da_{II} , and Pe numbers in layers *i* and *ii* for calcite and pyrite.

		30 hr	50hr	100hr	500hr
Layer <i>i</i> 5% < porosity < 65%	Da_I for calcite	$10^{-3} - 10^7$	$10^{-2} - 10^7$	$10^{-3} - 10^7$	$10^{-3} - 10^9$
	Da_{II} for calcite	$10^{-2} - 10^6$	$10^{-2} - 10^6$	$10^{-2} - 10^6$	$10^{-3} - 10^6$
	Pe	$10^{-2} - 100$	$10^{-2} - 10$	$10^{-3} - 10$	$10^{-4} - 10$
	Da_I for pyrite	$10^{-1} - 10^5$	$10^{-1} - 10^5$	$10^{-1} - 10^6$	$10^{-1} - 10^6$
	Da_{II} for pyrite	$10 - 10^4$	$1 - 10^4$	$1 - 10^4$	$10 - 10^3$
Layer <i>ii</i> Porosity=65%	Da_I for pyrite	$1 - 10^3$	$0.1 - 10^3$	$0.1 - 10^3$	$0.1 - 10^3$
	Da_{II} for pyrite	$10 - 10^4$	$1 - 10^4$	$1 - 10^4$	$0.1 - 10^4$
	Pe	~ 10	~ 10	$1 - 10$	$0.1 - 10$

Based on analysis of the Pe number over time, it is clear that the diffusion term becomes more important compared to advection in layer i at later times. When advective mass transport becomes negligible compared to diffusion, a combined mixed-kinetic control³⁴ relationship can be used for comparing the relative importance of surface-reaction kinetics versus diffusion control of effluent concentrations per Eqn. 3.10 and 3.11. The slower of the two rate terms in Eqn. 3.10, or the corresponding rate constants in Eqn.3.11, determines which of the processes controls dissolved species effluent concentration. For calcite dissolution, $k_{surf,calcite}$ and k_{diff} in layer i are plotted at 500hr in Figure 3.8, showing that $k_{surf,calcite} \gg k_{diff}$. This confirms that diffusion is the rate limiting process controlling calcite dissolution after 500hr of flow.

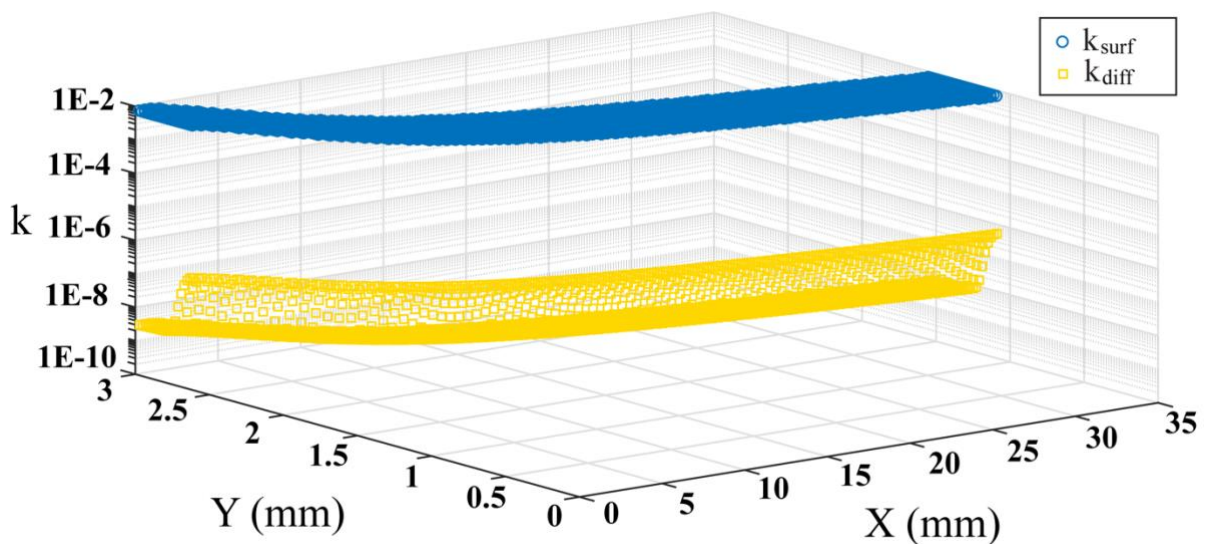


Figure 3.8: Surface-controlled reaction rate constant k_{surf} and diffusion-controlled reaction rate constant k_{diff} for calcite dissolution at 500 hr.

Model effluent pH and concentration of Ca, Fe, and As as a function of time up 1000 hr of simulation are presented in Figure 3.9. Similar to the experimental data trends shown earlier in Figure 3.3 for up to 100 hr of flow, the effluent Ca concentration shows an initial sharp increase and then decreases with time. An initial increase in pH corresponds to buffering

of the acidic solution by carbonate mineral dissolution at early times, which is consistent with the initial spike in Ca shown in Figure 3.9b. Per the Pe and Da number analysis discussed previously, the decline in Ca concentration after ~20 hrs is due to diffusive mass-transport limitations on calcite dissolution associated with the growing thickness of the depleted layers limiting access to remaining calcite within the shale matrix. In contrast, Fe and As effluent concentrations show a more gradual increase over the first ~400 hrs of simulation followed by a slow decrease at longer times. The increase in Fe and As effluent concentration is due to the increasing exposure of embedded pyrite in layer *i* initially at earlier times. However at longer times, as the thickness of layer *ii* increase pyrite dissolution is affected by a combination of reduction of pyrite reactive surface area and enhanced diffusive/advective transport process of pyrite allowing it to become nearly completely depleted in layer *ii* and only allowing very slow diffusion dissolution products out of layer *i*. The combined effects lead to the decrease of Fe and As effluent concentrations at the much longer times (1000 hr) simulated in Figure 3.9 compared to Figure 3.3 (100 hr).

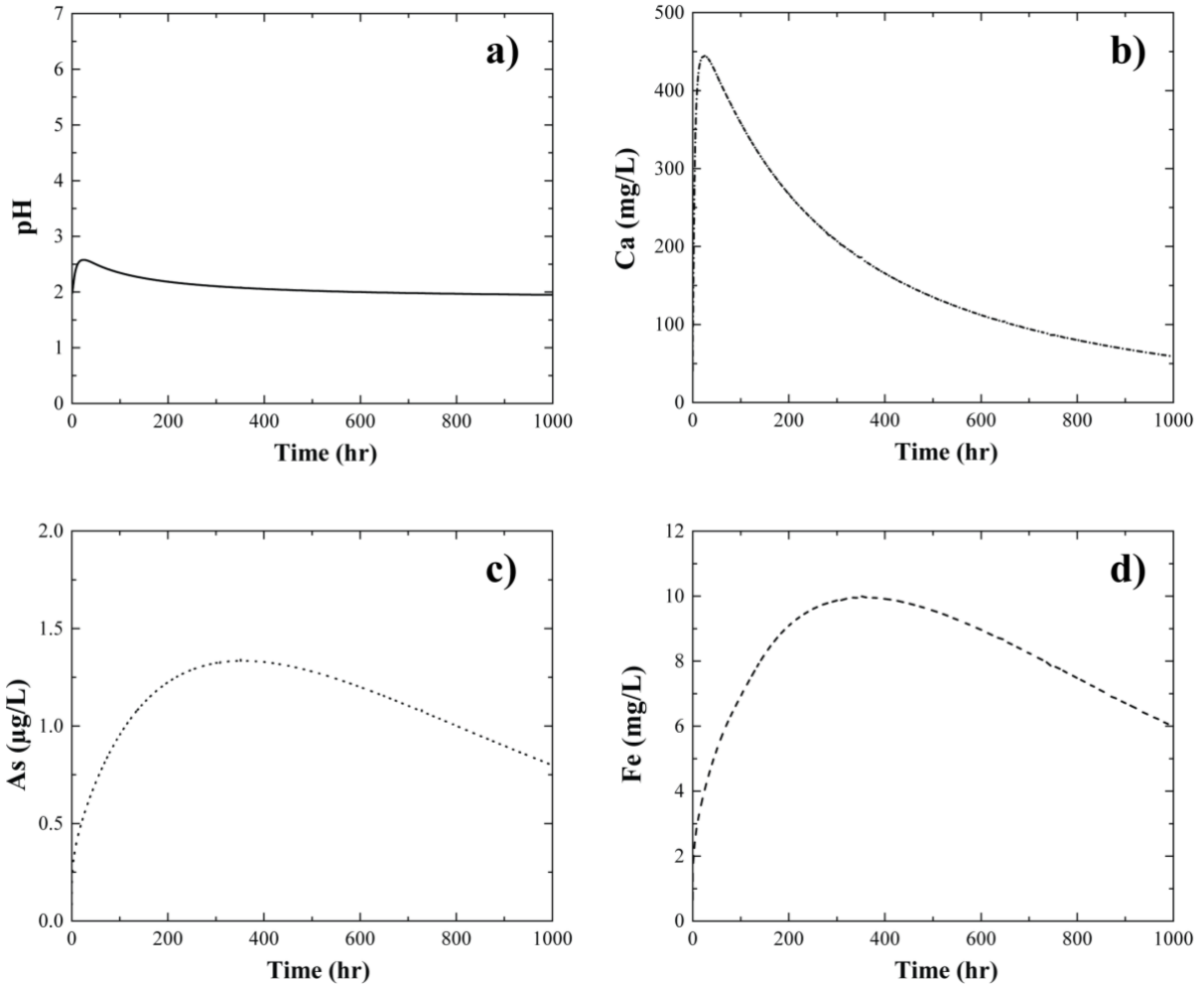


Figure 3.9: Model effluent pH and Ca, Fe and As concentration as a function of time at a flowrate of 10 ml/hr.

According to the mineral saturation index and volume data (model results shown in Figure B11), only calcite and siderite ($\text{FeCO}_3(\text{s})$) approach equilibrium in the altered layers *i*. In contrast, pyrite and illite are significantly under-saturated. Since the rate of calcite dissolution kinetics is much faster than the diffusive mass transport in grid cells within the altered layers *i*, the Ca effluent concentration is controlled by mass transport in and out of these cells, as noted earlier. For minerals like pyrite and illite, the surface-dissolution reaction rates are generally much slower than calcite. As such, the effluent concentrations of the species resulting from their dissolution (e.g., Al, Si) might be expected to be primarily controlled by the slower dissolution reaction rates of these minerals. However, the effluent concentration of

species from pyrite dissolution (e.g., Fe and As) are enhanced by higher mineral surface exposure with time and also limited by diffusion/advection transport as a result of their lower content and low equilibrium solubility. As such, even as effluent Ca concentration decreases with time due to its much faster dissolution and depletion, the effluent concentrations of Fe and As from pyrite dissolution continue to increase with time (Figure 3.9) as more pyrite surface area is exposed in region *ii* up to about 300 hr, after which it begins to diminish over longer times as slower transport processes begin to limit mineral dissolution.

3.3.5 Model sensitivity analysis

A model sensitivity analysis was performed to further assess the impact of mineral composition, injected fluid chemistry and flowrate on As and Fe mobilization from pyrite dissolution. In particular, variation in the calcite and pyrite content of the Collingwood shale as a function of the three different flowrates used in the experimental study were evaluated to see whether such changes would alter the conclusions drawn from the simulations of the experimental results previously discussed. Similarly, variations in pH and p_e were considered in the sensitivity analysis to determine whether they would significantly impact the extent of leaching of Fe from pyrite and As from As-bearing pyrite in shale.

Calcite content: Effluent Ca and As concentration profiles were generated from model simulation runs for variable calcite content (5%, 10%, 15%, 30%, 60% by volume) at a flowrate of 10 ml/hr with results shown in Figures 3.10b and d. As shown, higher calcite content generally leads to enhanced calcite dissolution and higher Ca effluent concentration resulting from a faster rate of dissolution as evidenced by the increasing slope of the Ca concentration profile vs. time (Figure 3.10b). However, calcite dissolution was slightly faster (greater slope) for a calcite content of 30% compared 60% as evidenced by the arrival of the peak

concentration are earlier times for 30% content as shown by the inset in Figure 3.10b. This was due to the acidic injection fluid maintaining a lower pH for the 30% compared to 60% calcite (Figure 3.10a and inset). In Figure 3.10c and d, higher calcite content leads to higher As and Fe effluent concentrations. Higher calcite content allows for a greater rate of exposure of pyrite and depletion with time in region *ii* (shown as thickness of altered layer *ii* in Figure 3.12). In addition, greater calcite depletion (greater porosity) leads to higher advective/diffusive transport in the altered layers, which further enhances pyrite dissolution and promotes As mobilization.

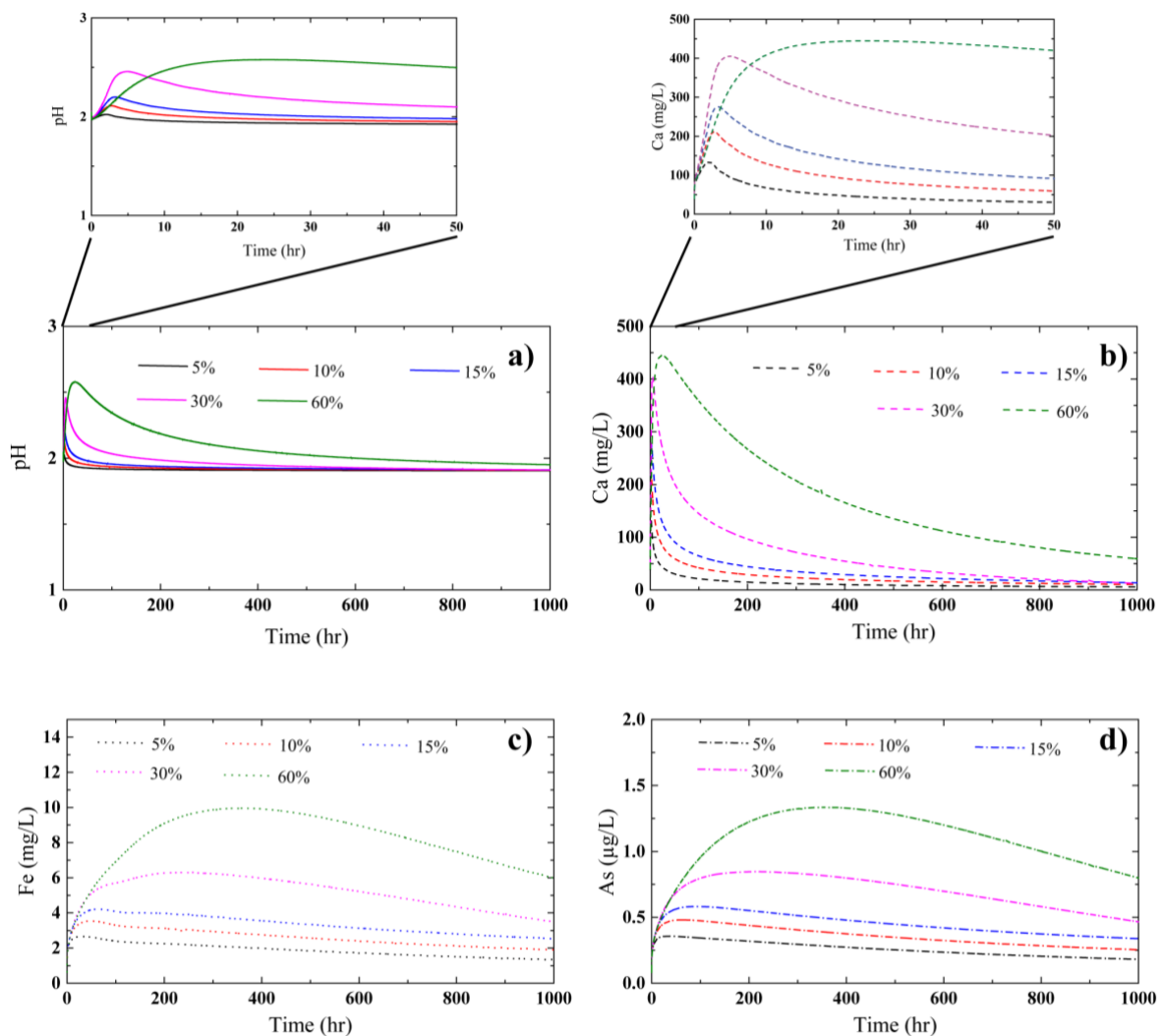


Figure 3.10: Model results (effluent pH, calcium, iron and arsenic concentration) at a flowrate of 10 mL/hr and variable calcite content (5%, 10%, 15%, 30%, 60%).

An analysis of the Pe numbers provides an explanation for the Ca dissolution trends with respect to changes in calcite content. Pe numbers $\gg 1$ indicate dominance of advection compared to diffusive mass transport. A value closer to 1 indicates the combined influence of advection and diffusion in controlling mass transport of aqueous species in and out of the grid cells. As shown in Figures 3.11a, b, and c, Pe numbers < 10 are found in altered layer regions *i* and *ii* for all calcite contents examined (e.g., 5%, 30%, 60%). Except for the highest calcite content of 60%, when the Pe number is near 10 in altered layer *ii* initially before decreasing to a value near 1 after 500 hr, the Pe number is ≤ 1 in both altered layers *i* and *ii*. This indicates advection can play a role in mass transport when calcite content is high. At a calcite content of 5% (Figure 3.11a), the average Pe number is always < 1 for both layers *i* and *ii*, indicating that slow diffusion is always dominating mass transport when calcite content is low. When the calcite content is low the porosity change is also small (from 5% to 10%), resulting in an effective diffusion coefficient that remains relatively small and constant throughout the simulation time.

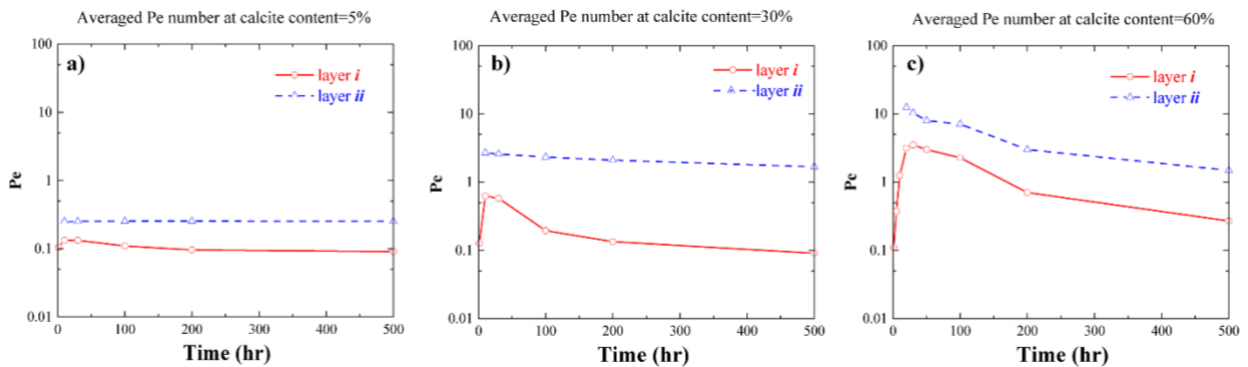


Figure 3.11: Model averaged Péclet number of cells inside altered layer *i* and *ii* at variable calcite content: a) 5%, b) 30%, c) 60%.

The specific grid Da_I and Da_{II} numbers for calcite dissolution (at 500 hr) as a function of calcite content are shown in Figure B12. The large Damköhler numbers are in line with prior results that demonstrate calcite dissolution kinetics are much faster than mass transport rates.

Advective mass transport becomes negligible compared to diffusion at 500 hr in layer *i*, with $k_{surf,calcite} \gg k_{diff}$. In general, these results are consistent with the previous simulations that demonstrate the importance of diffusive transport in controlling the rate of calcite dissolution and the resultant Ca effluent concentration over time.

The changes in the thickness of altered layers *i* and *ii* are plotted in Figure 3.12 as a function of calcite content. As calcite content increases, the thicknesses of layers *i* and *ii* increase slightly, but does not change significantly with calcite content. Figure B13 shows the penetration of the layers into the shale along the length of the core. When calcite content increases from 5% to 30%, the maximum penetration of the dissolution front into the shale matrix increases with calcite content near the reactor inlet and then slowly decreases along the length of the model domain. As the calcite content increases from 30% to 60%, the penetration depth of the altered layer is slightly less at the inlet for higher calcite contents due to greater pH buffering. As a result, a more rapid increase in the Ca effluent concentration occurs for the 30% compared to 60% calcite content at early times. Both Da numbers for pyrite dissolution inside layer *ii* are smaller when calcite content is higher. As discussed previously, higher calcite content leads to a greater increase in advective and diffusion transport within the calcite depleted regions, as well as higher As effluent concentration associated with pyrite dissolution. Smaller Da numbers also demonstrate how at later times surface-controlled pyrite dissolution becomes more and more important for As release. Greater exposure of pyrite and faster mass transport process associated with higher calcite content and subsequent increases in matrix porosity combine to promote more rapid pyrite dissolution and As leaching.

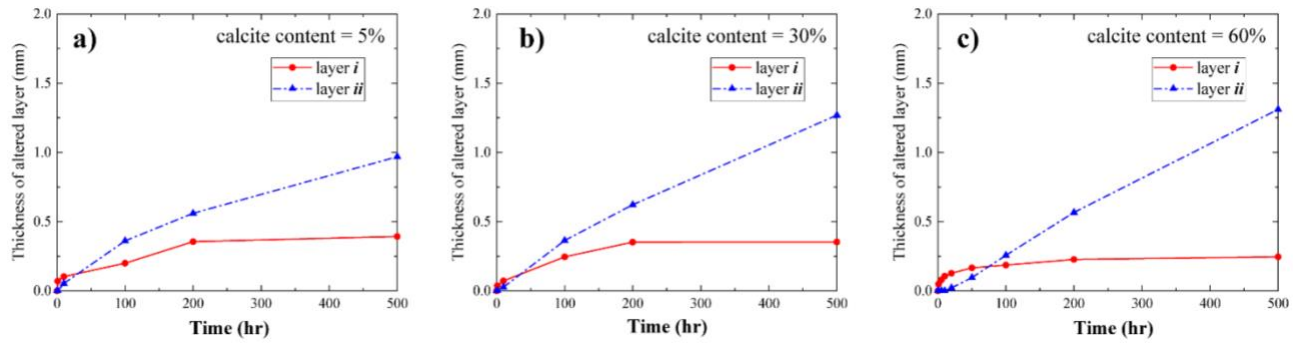


Figure 3.12: Thickness of altered layer *i* and layer *ii* as a function of time at variable calcite content (5%, 30%, 60%).

Pyrite content: Simulations of the impact of pyrite content from 1–3% over 1000 hr on As effluent concentration are shown in Figure 3.13. Higher pyrite content leads to higher effluent concentration of arsenic at all times. In all cases, As effluent concentration increases with time up to a broad peak region followed by a slower decrease of As with time. A more rapid increase to a higher value of effluent As concentration with time occurs as the pyrite content increases and more pyrite is exposed to injected fluid. Although not shown, higher O₂ content leads to an even greater increase in the pyrite dissolution rate for a given pyrite content. The Pe numbers for these simulations are the same as those previously mentioned, viz., Pe numbers < 10 (Figure 3.6), with advection and diffusive limited mass transport of mixed importance in the altered layers *i* and *ii*. The Da analysis is also similar to what was described previously at a calcite content of 60% (Figure 3.7) in which a combination of surface reaction and diffusive mass transport controls the Fe and As effluent concentrations at longer times over the narrow range of pyrite content (1–3%) simulated. Both Da_I and Da_{II} numbers for pyrite dissolution in layer *ii* decrease with the increase of pyrite content shown in Table B1, which highlight the importance of surface-controlled pyrite dissolution reaction.

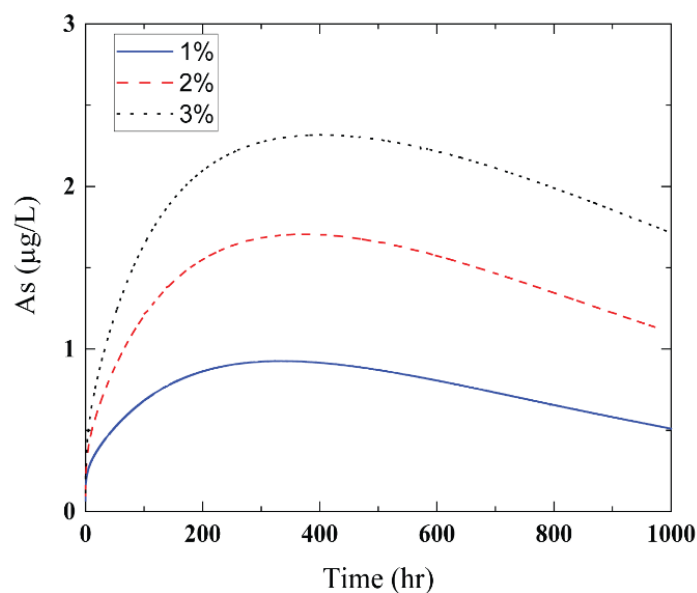


Figure 3.13: Model results effluent arsenic concentration at a flowrate of 10 mL/hr and variable pyrite content (1%, 2%, 3%).

Fluids characteristics: As shown in Table 3.1, the pyrite reaction rate is a function of oxygen concentration when no Fe(III) is present in this system. Higher O₂ levels and lower pH both theoretically lead to higher pyrite dissolution. However, higher O₂ content does not necessarily lead to higher effluent iron concentration since higher O₂ content also result in faster Fe(II) oxidation and the formation of insoluble Fe(III) precipitates like goethite. Model results at variable injected fluids pH values are shown in Figure 3.14. Only the lowest pH value of 1.9 of the injected fluids leads to substantial calcite and pyrite dissolution with trends consistent with previous simulations at this pH. However, once the injection fluid pH reaches 3 and above, leaching of Ca, Fe, and As becomes low, and at pH values of 4 and above, no significant change in Ca, Fe or As effluent concentrations from low values is observed with time and distance along the domain length in Figure 3.14. Only the calcite in direct contact with the main channel dissolves, albeit minimally, which leads to the low effluent concentrations of Ca, and low effluent concentration of Fe, and As from the pyrite embedded in the calcite.

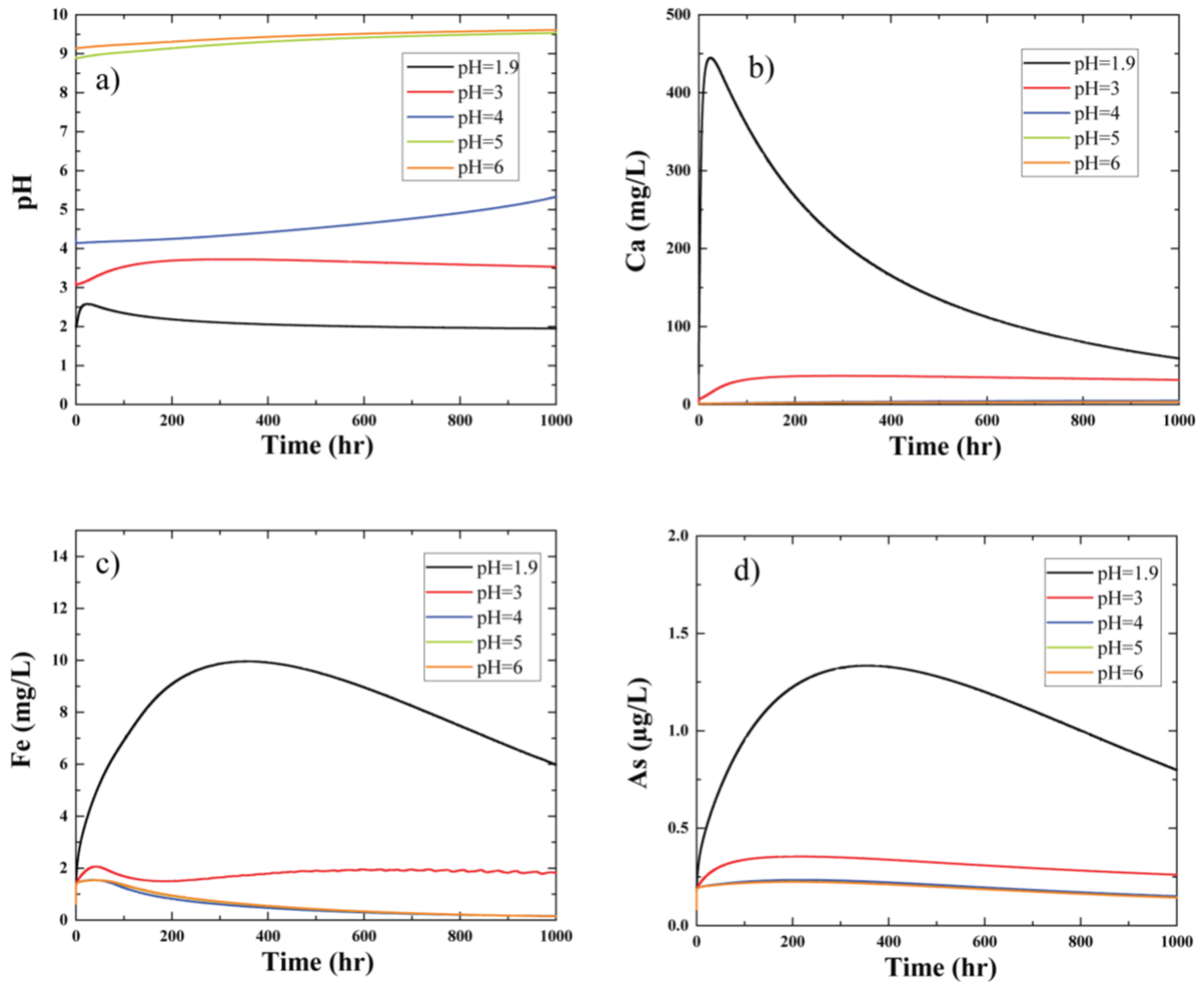


Figure 3.14: Model results (of effluent pH, and calcium, iron and arsenic concentrations) at a flowrate of 10 mL/hr and variable injected fluids pH (1.9, 3, 4, 5, 6).

Different flowrate: The impact of flow rate on effluent pH and concentration of Ca, Fe, and As is shown in Figure 3.15. In general, higher flowrate, leads to the maintenance of lower pH and Ca, Fe, and As effluent concentration. Lower flow rates allow greater calcite dissolution (Figure 3.15b), greater pH buffering (Figure 3.15a), and more pyrite exposure, which results in higher Fe and As effluent concentrations (Figures 3.15c and d). At the slowest flowrate of 2.5 ml/hr, the Ca effluent concentration increases rapidly and then levels off to a steady-state value. In contrast, the Fe and As concentrations increase more gradually but eventually reach a near steady-state value before decreasing slightly at the longest run time.

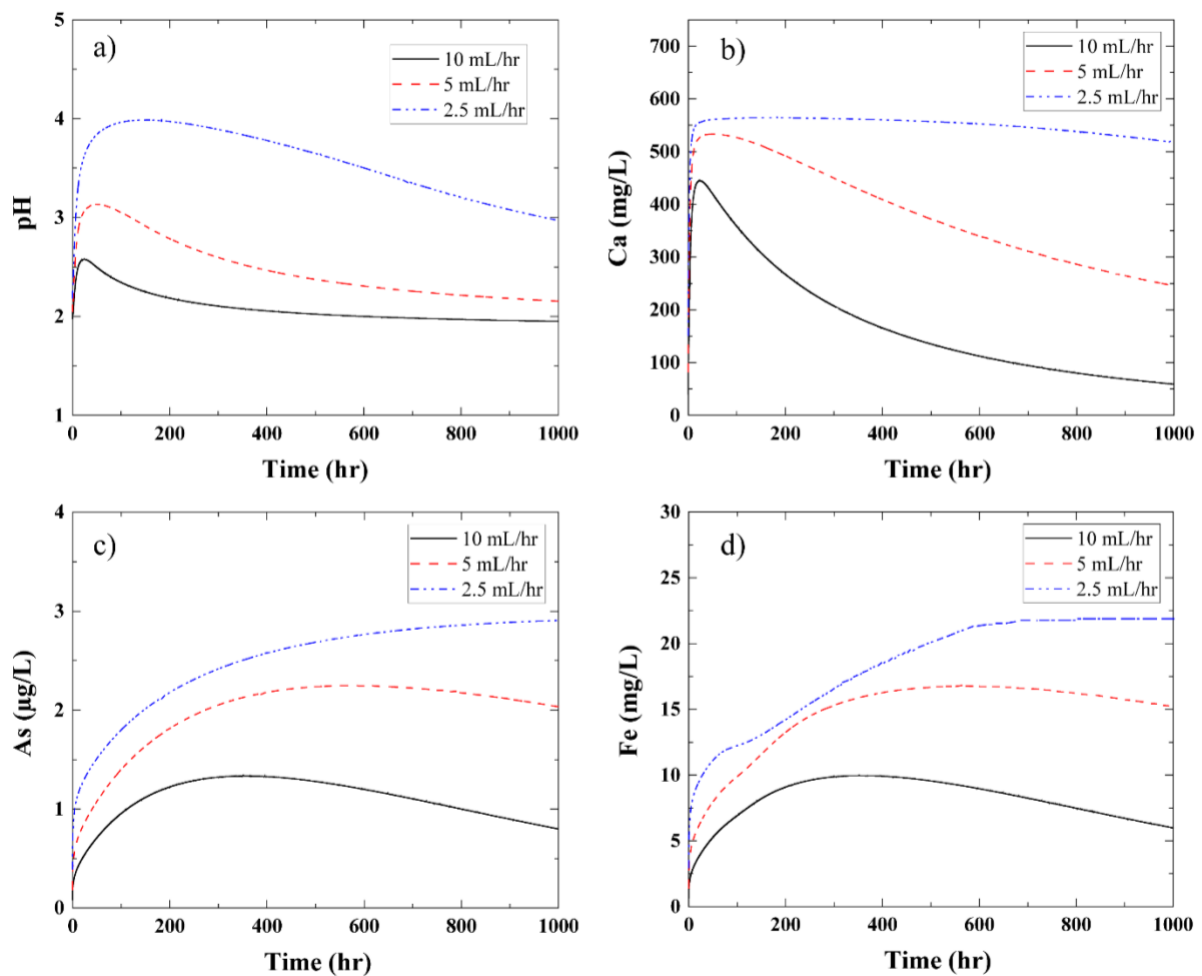


Figure 3.15: Model results (effluent pH, calcium, iron and arsenic concentration) at variable flowrate (10 mL/hr, 5 mL/hr, 2.5 mL/hr).

Based on Da dimensionless number analysis (not shown), at the highest flow rate condition, Ca, Fe and As effluent concentration are primarily limited by mass transport limitations out of the altered regions. Similar to previous discussion, the slight decrease for Fe and As at the longest times, results from the decreased diffusive mass transport at these longer times. Pyrite dissolution is more and more controlled by surface-controlled reaction under slower flowrates; Fe and As concentration keeps increasing with time instead of decreasing at higher flowrates (shown in Figure 3.15c and d). For the two faster flowrates of 5 and 10 mL/hr, the Ca effluent concentration increases initially until reaching a peak value and then decreases with time with a greater overall decrease at the highest flowrate. Per the Pe number analysis

shown in Figure 3.16, the lower Pe values for the slowest flowrate of 2.5 ml/hr compared to the flowrate of 10ml/hr indicate the increasing importance of diffusive vs. advective mass transport control of mineral dissolution as the flow rate decreases. Also, similar to early discussion (Figure 3.6), the averaged Pe grid numbers decrease with time (Figure 3.16) for a given flow rate indicating diffusion mass transport limitations prevail at longer time periods.

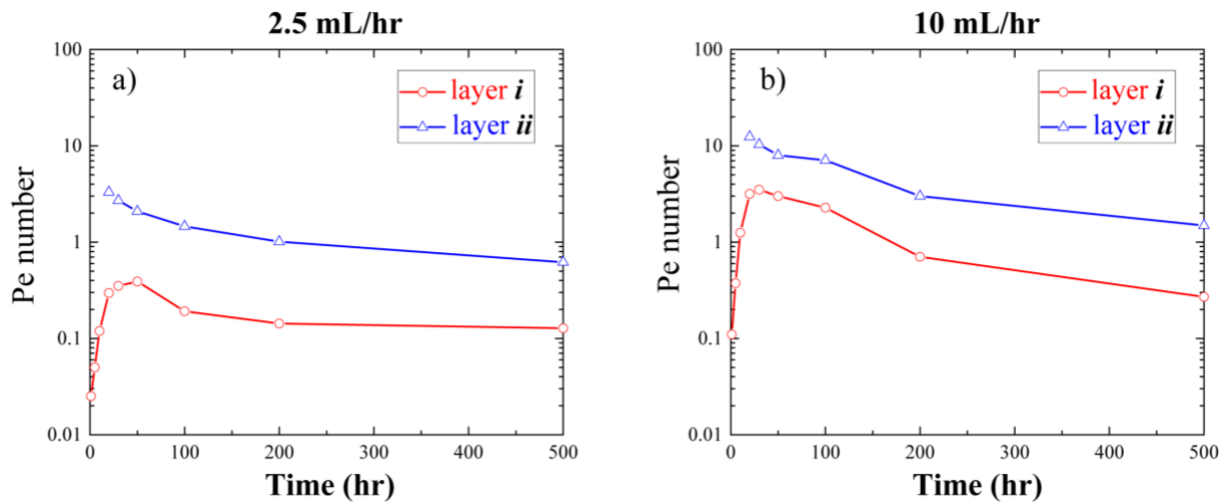


Figure 3.16: Averaged Péclet number of cells inside altered layers *i* and *ii* at two different flowrates (2.5 mL/hr, 10 mL/hr).

3.4 Conclusion

The reactive transport model developed in this paper assesses the importance of carbonate mineral dissolution as it relates to mobilization of toxic elements such as As in carbonate-rich shale in contact with oxidic acidic fluids. The model was calibrated based on two core flooding experiments and simulation results agree well with experimental data. This model tracks the mineral dissolution front, demonstrates and quantifies the formation of two distinct altered shale layers adjacent to the fracture pathway, and allows for evaluation of rate limiting controls of mineral dissolution. The non-dimensional number discussion results demonstrate that calcite dissolution is mainly diffusive mass transport limited, while the dissolution of pyrite embedded within calcite-depleted layers of the shale is controlled by a combination of surface

reaction rate and mass transport limitations. The fast dissolving calcite affects the accessibility of slowly dissolving mineral like pyrite, increases mass transport process, exposes more pyrite area, and then subsequently enhances As mobilization.

Higher carbonate content in shale formations lead to higher effluent As concentration. A smaller overall Pe number indicates diffusion dominates mass transport over the entire experimental timeframe at lower calcite content. Narrower Da number ranges for calcite dissolution have been observed in formations with higher calcite content. When calcite is at smaller initial concentrations calcite dissolution contributes less to changes in porosity and effective diffusion change flow of acidic fluids and calcite dissolution is mass transport-controlled. The thickness of altered layer δ increases with calcite content when calcite is less than 30% of the shale composition. However, the thickness of the altered layer δ is similar or even smaller at higher calcite content when calcite content is higher than 30%. The altered layer δ thickness can directly affect pyrite exposure area and As leaching. Diffusive mass transport will be enhanced because of the higher porosity that can be achieved at higher calcite content after the shale formation becomes calcite depleted with time. The larger exposure of pyrite together with faster diffusion process associated with higher calcite content results in enhanced As mobilization. In addition to higher calcite content, higher pyrite content, and lower pH and lower flowrate of the injected fluid can all lead to an increase As leaching.

3.5 References:

- (1) Lavergren, U.; Åström, M. E.; Bergbäck, B.; Holmström, H. Mobility of Trace Elements in Black Shale Assessed by Leaching Tests and Sequential Chemical Extraction. *Geochem. Explor. Environ. Anal.* **2009**, 9 (1), 71–79.
- (2) Andrew W. Nelson; Andrew W. Knight; Dustin May; Eric S. Eitrheim; Michael K. Schultz. Naturally-Occurring Radioactive Materials (NORM) Associated with Unconventional Drilling for Shale Gas. In *Hydraulic Fracturing: Environmental Issues*; ACS Symposium Series; American Chemical Society, 2015; Vol. 1216, pp 89–128.
- (3) Brumsack, H.-J. The Trace Metal Content of Recent Organic Carbon-Rich Sediments: Implications for Cretaceous Black Shale Formation. *Palaeogeogr. Palaeoclimatol. Palaeoecol.* **2006**, 232 (2–4), 344–361.
- (4) Peng, B.; Song, Z.; Tu, X.; Xiao, M.; Wu, F.; Lv, H. Release of Heavy Metals during Weathering of the Lower Cambrian Black Shales in Western Hunan, China. *Environ. Geol.* **2004**, 45 (8), 1137–1147.
- (5) Leventhal, J. S. Pyrolysis Gas Chromatography-Mass Spectrometry to Characterize Organic Matter and Its Relationship to Uranium Content of Appalachian Devonian Black Shales. *Geochim. Cosmochim. Acta* **1981**, 45 (6), 883–889.
- (6) Leventhal, J. S. Comparison of Organic Geochemistry and Metal Enrichment in Two Black Shales: Cambrian Alum Shale of Sweden and Devonian Chattanooga Shale of United States. *Miner. Deposita* **1991**, 26 (2), 9.
- (7) Swanson, V. E. *Geology and Geochemistry of Uranium in Marine Black Shales--A Review*; Professional Paper; Report 356C; 1961.
- (8) Vine, J. D.; Tourtelot, E. B. Geochemistry of Black Shale Deposits—a Summary Report. *Econ. Geol.* **1970**, 65 (3), 253–272.

- (9) Matamoros-Veloza, A.; Peacock, C. L.; Benning, L. G. Selenium Speciation in Framboidal and Euhedral Pyrites in Shales. *Environ. Sci. Technol.* **2014**, *48* (16), 8972–8979.
- (10) Galán, E.; Gómez-Ariza, J. L.; González, I.; Fernández-Caliani, J. C.; Morales, E.; Giráldez, I. Heavy Metal Partitioning in River Sediments Severely Polluted by Acid Mine Drainage in the Iberian Pyrite Belt. *Appl. Geochem.* **2003**, *18* (3), 409–421.
- (11) Expanding the role of reactive transport models in critical zone processes
<http://www.sciencedirect.com/science/article/pii/S001282521630280X>
- (12) Zhang, L.; Dzombak, D. A.; Nakles, D. V.; Brunet, J.-P. L.; Li, L. Reactive Transport Modeling of Interactions between Acid Gas (CO₂ + H₂S) and Pozzolan-Amended Wellbore Cement under Geologic Carbon Sequestration Conditions. *Energy Fuels* **2013**, *27* (11), 6921–6937.
- (13) Mayer, K. U.; Alt-Epping, P.; Jacques, D.; Arora, B.; Steefel, C. I. Benchmark Problems for Reactive Transport Modeling of the Generation and Attenuation of Acid Rock Drainage. *Comput. Geosci.* **2015**, *19* (3), 599–611.
- (14) Offeddu, F. G.; Cama, J.; Soler, J. M.; Dávila, G.; McDowell, A.; Craciunescu, T.; Tisceanu, I. Processes Affecting the Efficiency of Limestone in Passive Treatments for AMD: Column Experiments. *J. Environ. Chem. Eng.* **2015**, *3* (1), 304–316.
- (15) Luquot, L.; Gouze, P.; Niemi, A.; Bensabat, J.; Carrera, J. CO₂-Rich Brine Percolation Experiments through Heletz Reservoir Rock Samples (Israel): Role of the Flow Rate and Brine Composition. *Int. J. Greenh. Gas Control* **2016**, *48*, 44–58.
- (16) Thaysen, E. M.; Soler, J. M.; Boone, M.; Cnudde, V.; Cama, J. Effect of Dissolved H₂SO₄ on the Interaction between CO₂-Rich Brine Solutions and Limestone, Sandstone and Marl. *Chem. Geol.* **2017**, *450*, 31–43.

- (17) Soler, J. M. Two-Dimensional Reactive Transport Modeling of the Alteration of a Fractured Limestone by Hyperalkaline Solutions at Maqarin (Jordan). *Appl. Geochem.* **2016**, *66*, 162–173.
- (18) Deng, H.; Molins, S.; Steefel, C.; DePaolo, D.; Voltolini, M.; Yang, L.; Ajo-Franklin, J. A 2.5D Reactive Transport Model for Fracture Alteration Simulation. *Environ. Sci. Technol.* **2016**, *50* (14), 7564–7571.
- (19) Cai, Z.; Li, L. How Long Do Natural Waters “Remember” Release Incidents of Marcellus Shale Waters: A First Order Approximation Using Reactive Transport Modeling. *Geochem. Trans.* **2016**, *17* (1), 6.
- (20) Wen, H.; Li, L.; Crandall, D.; Hakala, A. Where Lower Calcite Abundance Creates More Alteration: Enhanced Rock Matrix Diffusivity Induced by Preferential Dissolution. *Energy Fuels* **2016**, *30* (5), 4197–4208.
- (21) Wang, L.; Fortner, J. D.; Giammar, D. E. Impact of Water Chemistry on Element Mobilization from Eagle Ford Shale. *Environ. Eng. Sci.* **2014**.
- (22) Le Pape, P.; Blanchard, M.; Brest, J.; Boulliard, J.-C.; Ikogou, M.; Stetten, L.; Wang, S.; Landrot, G.; Morin, G. Arsenic Incorporation in Pyrite at Ambient Temperature at Both Tetrahedral S–I and Octahedral FeII Sites: Evidence from EXAFS–DFT Analysis. *Environ. Sci. Technol.* **2017**, *51* (1), 150–158.
- (23) Huggins, F. E.; Huffman, G. P. Modes of Occurrence of Trace Elements in Coal from XAFS Spectroscopy. *Int. J. Coal Geol.* **1996**, *32* (1), 31–53.
- (24) Scanco Medical: micro CT scanners, image analysis software, microtomography scan services <http://www.scanco.ch/>.
- (25) Steefel, C. I.; Appelo, C. a. J.; Arora, B.; Jacques, D.; Kalbacher, T.; Kolditz, O.; Lagneau, V.; Lichtner, P. C.; Mayer, K. U.; Meeussen, J. C. L.; et al. Reactive Transport

- Codes for Subsurface Environmental Simulation. *Comput. Geosci.* **2015**, *19* (3), 445–478.
- (26) Steefel, C. CrunchFlow Software for Modeling Multicomponent Reactive Flow and Transport. User's Manual. *Earth Sci. Div. Lawrence Berkeley Natl. Lab. Berkeley CA Oct.* **2009**, 12–91.
- (27) Jew, A. D.; Dustin, M. K.; Harrison, A. L.; Joe-Wong, C. M.; Thomas, D. L.; Maher, K.; Brown, G. E.; Bargar, J. R. Impact of Organics and Carbonates on the Oxidation and Precipitation of Iron during Hydraulic Fracturing of Shale. *Energy Fuels* **2017**, *31* (4), 3643–3658.
- (28) Singer, P. C.; Stumm, W. Acidic Mine Drainage: The Rate-Determining Step. *Science* **1970**, *167* (3921), 1121–1123.
- (29) Dullien, F. A. L. *Porous Media: Fluid Transport and Pore Structure*; Academic Press, 1979.
- (30) Kadhim, F. S.; Samsuri, A.; Kamal, A. A Review in Correlation between Cementation Factor and Carbonate Rock Properties. *Life Sci J* **2013**, *10* (4), 2451–2458.
- (31) Heidari, P.; Li, L.; Jin, L.; Williams, J. Z.; Brantley, S. L. A Reactive Transport Model for Marcellus Shale Weathering. *Geochim. Cosmochim. Acta* **2017**, *217*, 421–440.
- (32) Palandri, J. L.; Kharaka, Y. K. *A Compilation of Rate Parameters of Water-Mineral Interaction Kinetics for Application to Geochemical Modeling*; DTIC Document, 2004.
- (33) Steefel, C. I.; Maher, K. Fluid-Rock Interaction: A Reactive Transport Approach. *Rev. Mineral. Geochem.* **2009**, *70* (1), 485–532.
- (34) Rickard, D.; Sjöberg, E. L. Mixed Kinetic Control of Calcite Dissolution Rates. *Am. J. Sci.* **1983**, *283* (8), 815–830.

Chapter 4

Estimating Radium Activity in Shale Gas Produced Brine

4.1 Introduction

The accumulation of naturally occurring radioactive materials (NORM) in wastewater from oil and gas production has been recognized by the industry since the early 1930s, but the potential for harmful exposure from NORM in such waste streams did not gain significant attention until the mid-1980's when Ra-226 was detected in mineral scale.^{1,2} Ra mineral scale may form in downhole and aboveground piping, sludge, sand, and produced water, with produced water representing the largest source of NORM waste from shale hydrocarbon extraction. Ra-226 and Ra-228 comprise the majority of the NORM in produced water and can be concentrated during mineral scale formation through co-precipitation with barite ($\text{BaSO}_4(\text{s})$). The subsequent potential for radiation exposure from Ra and its decay products in produced brine water and barite residues is of primary concern.³ Proper management of produced wastes is essential for preventing NORM contamination of freshwater resources from shale gas production. When the Ra radiation levels exceed safe exposure limits for NORM,⁴ produced wastewater treatment and sludge disposal options will largely be driven by the Ra regulatory radiation limits.

Organic-rich shale deposits are known to have inherently higher radioactivity than typical rock formations and production of elevated levels of NORM in flowback wastewater from shale gas production, typically quantified in terms of Ra isotopes, has been reported.⁵⁻⁸ This is confirmed by gamma-ray log counts that show elevated readings for radioactive

potassium (K), thorium (Th) and uranium (U) in organic-rich shale formations.⁹ High K and Th radioactive counts in shale typically reflect the high clay content, while the presence of relatively high counts for U is often indicative of its association with the reduced organic matter in targeted shale formations.¹⁰ In this case, U remains trapped within the shale in a reduced, highly insoluble and immobile U(IV) form. In contrast, in oil and gas reservoirs comprised primarily of limestone, U is often present in its oxidized form U(VI) and primarily held within the $\text{CaCO}_{3(s)}$ crystal lattice, with UO_2^{2+} substituting for Ca^{2+} .¹¹

Naturally abundant radio isotopes of U (U-238) and Th (Th-232) are present in most targeted reservoirs, leading to elevated amounts of their decay products including Ac, Ra, Bi, Po, Rn, Pb (decay chains shown in Appendix C Figure C4).¹² Rn is a gas and can be easily released to the atmosphere during production activities. In contrast, Ac, Pb, and Po form very insoluble solid phases and tend to remain in the formation associated with solid phases during oil and gas production.^{4,13,14} The Ra isotopes (e.g., Ra-226 and Ra-228 with relatively long half-lives of 1500 yr and 5.75 yr, respectively) have higher solubility¹⁵ and are more likely to be present in produced brines returning to the surface. As an alkaline earth divalent cation, Ra(II)'s chemical properties closely resemble barium (as Ba(II)), the element above it in Group 2 of the periodic table. As such, Ra(II) radioisotopes will accumulate in barite-scale that forms on wellbore pipes or in solid waste.^{14,16}

Over the past decade, new unconventional horizontal drilling technology together with hydraulic fracturing has extracted large quantities of natural gas in the United States.¹⁷ Along with the successful energy production, the TENORM (i.e., technology enhanced NORM concentrations) in liquid and solid wastes have been of particular concern.^{4,18,19} Total Ra levels in produced waters range from below the detection limit to radioactive concentrations as high as several thousand pCi/L.^{6,7,20,21} Associated barite-scale sludge waste, which can incorporate Ra,²² may contain as much as several thousand pCi/g after condensation.¹⁴ Compiled Ra

content data for oil and gas field produced water in the Northern Appalachian Basin show that Ra concentration in produced water increases with increasing salinity.⁶ Higher Ra concentrations were also found in Marcellus produced water compared to conventional oil and gas wells, also likely due to the high total dissolved solids (TDS) content of the produced water.⁶ An investigation by Warner et al.⁸ indicated that the effluent discharge from a facility treating Marcellus produced water led to high bromide concentrations in surface water and enhanced Ra concentrations in the associated sediments. The Ra adsorption to river sediments was thought to be enhanced by the salinity decrease of the wastewater effluent that occurred upon mixing with the surface water.⁸ A recent study by Lauer et al.²³ also indicated that the disposal of treated conventional oil and gas wastewaters can lead to higher Ra activity in stream sediments at centralized waste treatment facility disposal sites. Nelson et. al⁴ used the theoretical Bateman model²⁴ to calculate the total radioactivity in produced fluids including Ra and Ra decay products, assuming the system is closed to the release of gaseous radon. This model predicted that decay products can contribute to an increase in total NORM levels. However, this model focused on calculating total radioactivity based on Ra isotope activity in produced fluids and did not seek to connect Ra activity in produced fluids with the original shale composition or the produced water composition (e.g., TDS or sulfate concentration). In another study, Nelson et al.²⁵ investigated the partitioning behavior of NORM in Marcellus produced fluids and found that the levels of heavier alkaline earth metals (Ba, Sr) are stronger predictors of dissolved Ra(II) than ionic strength alone. A RESRAD (RESidual RADioactive) model was used by Zhang et. al²⁶ to assess the radiation dose equivalent and associated health risk from Marcellus shale flowback water in storage impoundments. Further development of a method for estimating Ra activity in shale gas wastewaters would be of substantial value if it could provide an *a priori* estimate of the potential for high Ra activities in produced brine based

on measurable parameters such as U, Th content in shale, shale cation exchange capacity (CEC), and TDS and sulfate concentration.

As indicated above, Ra originates from the decay of parent radionuclides present in the shale that formed several hundred million years ago. Because U-238 and Th-232 are the most abundant and stable isotopes for U and Th (with half-lives of 4.5 and 14.5 billion years, respectively), they remain in measurable amounts in shale today. The rate-determining, slowest decay step is the first one (U-238 and Th-232 decay), which is several orders of magnitude slower than the following steps in the decay chain. When the time interval is longer than 2 million years steady-state is achieved,¹⁵ with all isotopes in the decay chain at equal activity. This steady-state condition in a decay chain is known as secular equilibrium (per Appendix C section C-4). When Ra isotopes have reached secular equilibrium, inorganic elements in shale reservoirs are highly reduced. The formation brine water is high in TDS. Under these conditions, the main processes responsible for mobilizing Ra between the reduced rock matrix and formation water are thought to be alpha-recoil, chemical leaching by formation brine, adsorption/desorption by ion exchange, and possibly, co-precipitation of Ra in solution with barite, depending on the concentration of sulfate.¹³ Sulfate in the formation brine may come from gypsum dissolution, pyrite oxidation, and/or remnant marine waters, while sulfate can be lost via SO₄ microbial reduction or mineral precipitation.²⁷ Compared to groundwater, notably low levels of sulfate were reported in several Devonian organic-rich shale and sandstone formation water samples.²⁷

Although high-purity germanium (HPGe) gamma spectroscopy has been proven to be a reliable approach to measure Ra activity in shale gas produced brines,²¹ this method is limited by the available sample size, long preparation time, detector efficiency, and available counting time. Zhang et al.²⁸ developed a method that combined inductively coupled mass spectrometry (ICP-MS) with solid-phase extraction to separate and purify radium isotopes from the matrix

elements to obtain rapid Ra-226 activity measurements with a relative standard deviation of 15%. In the current study, a simpler approach was developed to measure Ra-226 also using ICP-MS by matching the matrix of the measurement standards to that of the produced brine samples. This measurement provided for rapid Ra-226 analysis compared to traditional time-consuming measurements via HPGe gamma spectroscopy.

The overall goal of this work was to develop a simplified predictive model to estimate the Ra activity in produced brine by linking the shale U and Th content together with CEC to Ra activities in produced water of variable TDS and sulfate composition. To do this, the Ra activity and TDS were measured in produced brines from several formations, including the Antrim and Utica-Collingwood formations from the Michigan basin as well as the Marcellus shale, which is currently the largest shale play in the shale gas industry.²² Shale U and Th content can be estimated based on spectral gamma-ray well logs. Given that the respective ages of the Antrim, Utica/Collingwood, and Marcellus formations are 359–383 Ma and 444–458/458–470 Ma, and 384 Ma; a model assumption of secular equilibrium is reasonable and Ra content in a shale can be estimated based upon the U and Th content of the shale. Finally, assuming that co-precipitation of Ra with barite or ion exchange of Ra by clay minerals in shale are the primary processes controlling produced water Ra activity, this work develops an empirical relationship for estimating Ra-226 activity as a function of shale U content and brine TDS as a first order screening tool to identify shale formations where Ra in TENORM waste streams may reach activities of concern.

4.2 Materials and methods

4.2.1 Shale samples

Shale samples from Antrim and Utica-Collingwood formation for this study were collected at the Michigan Geological Repository for Research and Education. Antrim shale

underlies the uppermost Devonian formation, the Ellsworth shale, in the Michigan Basin. Antrim shale samples were gathered from the following wells: Thompson 1–27 well at depths ranging between 127–151 m; State Chester 18 well at four intervals between 457–506 m; and St. Otsego Lake #9-15 at depth of 462–489 m. The Utica-Collingwood formation is a natural gas reservoir comprised of the Utica shale and the organic-rich Collingwood limestone. It is an emerging shale gas reservoir located in the northern Lower Peninsula of Michigan at a depth of ~3 km. The Collingwood and Utica shale samples were collected from drilled core material from the JEM Brugger #3-7 well. The Collingwood samples were taken from depths between 2948–2954 m and Utica samples from depths between 2940–2944 m. The Marcellus shale sample was collected from an outcrop near Bedford, Pennsylvania. Shale sample compositions were obtained by X-Ray diffraction (XRD) (see Appendix C section C-5 Table C3).

4.2.2 Flowback and produced water samples

Flowback water was sampled from the Utica-Collingwood State Beaver Creek 1-23 HD-1 well. Samples were withdrawn starting at 2 hours after the initial flowback from a port downstream of the wellhead but upstream of the storage tank. After the well was brought into production (~2 weeks), water samples were collected from the separator. Produced water samples from 17 Antrim wells were also collected. All field samples were filtered through 0.45 µm PTFE filters and then stabilized by the addition of nitric acid to a pH < 2 prior to analysis of major cations by an ICP-MS. The major anions were obtained by ion chromatography (IC) using filtered but not acidified samples.

4.2.3 Shale digestion and chemical analyses

Complete digestion of the shale samples was conducted by Activation Laboratories Ltd (ON, Canada) using the 4B2-STD method²⁹ to obtain U and Th data for several Antrim,

Collingwood and Utica samples. Dissolved metal analyses in field water samples were conducted on an Agilent 7900 ICP-MS. Anions including chloride, bromide, and sulfate were measured by IC. ICP-MS and HPGe gamma spectroscopy (following methods of Nelson et al.²¹) were used to directly measure long half-life radium isotopes in the field water samples. Rapid ICP-MS method is established by adding 100g/L Cl⁻ to all Ra-226 standard to match high salinity sample matrix. The average calibration curve is shown in Figure C2. The HPGe gamma spectroscopy detector was calibrated by counting a mixed multiple isotope standard (Eckert & Ziegler 7501) to establish efficiency curves for HPGe and covered an energy range from 60 to 1836 keV. This standard was specially ordered to have a density of 1.2 g/cm³ in order to be representative of the density of the high salinity water samples. Flowback samples were decanted into a 500 mL HDPE bottle and adjusted to a density of 1.2 g/cm³ using NaCl. A 5% Bacto agar powder was then added to form a homogeneous suspension.²¹ Samples were held for 21 days in a closed container to ensure the short-lived Rn daughter product of Ra-226 decay reached secular equilibrium. The daughter decay products Bi-214 and Ac-228 were used to estimate total Ra-226 and Ra-228, respectively. During each sample counting, gamma emissions were measured for 100,000 s for the field samples and 200,000 s for blanks run between field samples. GenieTM 2000 software³⁰ was used to estimate the Ra activity.

4.2.4 Ba adsorption/desorption experiments

Adsorption/desorption experiments were performed to better understand Ra mobilization mechanisms. As mentioned earlier, U and Th levels are higher in shale gas reservoirs compared to normal rock samples. However, even so, Ra levels are often at trace levels (pg/g level) and below detection typical in the shale quantities (e.g., 1–10g) used for laboratory-scale experiments. When Ra becomes concentrated in solid phases such as barite (e.g., several hundred pCi/g³¹), potential health concerns can arise from radiation exposure, and

in such cases special handling may be required for conducting laboratory experiments or disposing of solid phase residues. Because the Ra activities in our selected shale samples were too low to monitor, Ba was used as a surrogate for Ra. Ba is expected to have similar adsorption affinity to Ra for exchange sites, based on ionic radii for Ba and Ra (e.g., 1.42 Å and 1.48 Å, respectively).³² Also, since Ba was in higher concentration in our shale samples and is non-radioactive, it could be measured conveniently by ICP-MS. Ba adsorption experiments were conducted using powdered Collingwood, Utica, Antrim, and Marcellus shale samples to establish adsorption isotherm. Samples were contacted with different concentrations of Ba to determine the CEC for each shale. Each set of desorption experiments was also conducted by exposing the Ba-loaded shale to varying TDS concentrations. This was done to determine the amount of Ba that could be released from the shale as a function of initial Ba loading conditions and TDS.

4.3 Results and discussion

4.3.1 Validating U, Th estimates from spectral gamma-ray well logs

The long half-lives of U-238 (4.5 billion years) and Th-232 (14 billion years) ensure that their content in the Collingwood, Utica, Antrim, and Marcellus shale are the same today as when the shale formed millions of years ago. Given this, it is possible to estimate the total Ra-226 and Ra-228 activities generated by decay if the activity of U-238 and Th-232 can be accurately measured. Even though it is unrealistic to assume U and Th concentrations remain constant throughout a formation, spectral gamma-ray well logs may serve as a good first-order approach to estimate the U and Th content for a given shale reservoir at a given depth (e.g., per Appendix C Section C-2). To confirm this, spectral gamma-ray well logs within the targeted shale region of the Antrim formation were obtained and compared to actual U and Th concentrations obtained from digestion of the shale samples. In particular, two shale samples

from the Antrim interval (458 m, 475 m) with higher U content and two samples (503 m, 506 m) with low U content were chosen to compare the U and Th content determined by the total digestion measurement versus the gamma-ray log estimation method (Table C2). According to Blum et al.³³, spectral gamma-ray log estimates for U and Th are expected to have errors on the order of ~35% and 23%, respectively, compared to actual total shale content. As shown in Table C2, the differences between measured and gamma-ray log estimated values are within the range of error provided by Blum et al.³³, suggesting that gamma-ray logs can be used to reasonably estimate an average U and Th concentration for a given shale formation.

4.3.2 Rapid analysis of Ra activity via ICP-MS

Although HPGe gamma spectroscopy (HPGe-GS) has proven to be an effective approach for measuring Ra-226 and Ra-228 in hydraulic fracturing flowback water²¹, the time-consuming sample preparation and long waiting time (~21 day) required to achieve secular equilibrium are not ideal for rapid, routine analysis. As a result, an ICP-MS method was evaluated for determining Ra-226 activity with the goal of developing a faster approach for measuring Ra activities in shale gas waste fluids. The details of this approach and a sample calibration curve are provided in the Appendix C (Section C-3).

To compare the two analytical methods, Ra-226 activity was measured by both ICP-MS and HPGe-GS for flowback water from the Collingwood and Antrim formations. In the case of the Collingwood flowback water, samples were taken starting from early well production up to about 20 days to follow the changes in the flowback water Ra activity with time. Results from HPGe-GS show that total Ra activity (Ra-226 and Ra-228) peaked at around 8–12 days from the start of flowback (~4500 pCi/L), and reached steady state after 20 days (~2200 pCi/L) (Figure C3). It was also found that Ra-226 correlated well with total radium, indicating that Ra-226 could serve as a suitable estimate for total Ra assuming a proper ratio

factor with Ra-228. In contrast to HPGe-GS, the ICP-MS measurement of Ra-226 did not perform well at high salinity (e.g., 150–230g/L chloride)/low Ra activity (e.g., <1000 pCi/L) samples like those from Collingwood flowback water (Figure 4.1a). However, the ICP-MS measurement results were in good agreement with HPGe-GS for Antrim produced water samples that had lower salinity and higher Ra activity (Figure 4.1b). Figure 4.1b shows a positive correlation between dissolved Ra-226 activity and increasing salinity from the different Antrim wells. The results from both ICP-MS and HPGe-GS for the Antrim water measurements were also in good agreement. Although the ICP-MS method provides a more rapid analysis (e.g., same day results and samples can be run without the preprocessing steps and equilibration time needed for HPGe-GS), the ~1250 pCi/L detection limit (Figure C2) of the ICP-MS analysis is more than ten times higher than the HPGe-GS method. Nonetheless, since many produced water samples fall within the ICP-MS method operational range with respect to salinity and Ra-activity, ICP-MS analysis will often be a more efficient method for measuring Ra in flowback water samples.

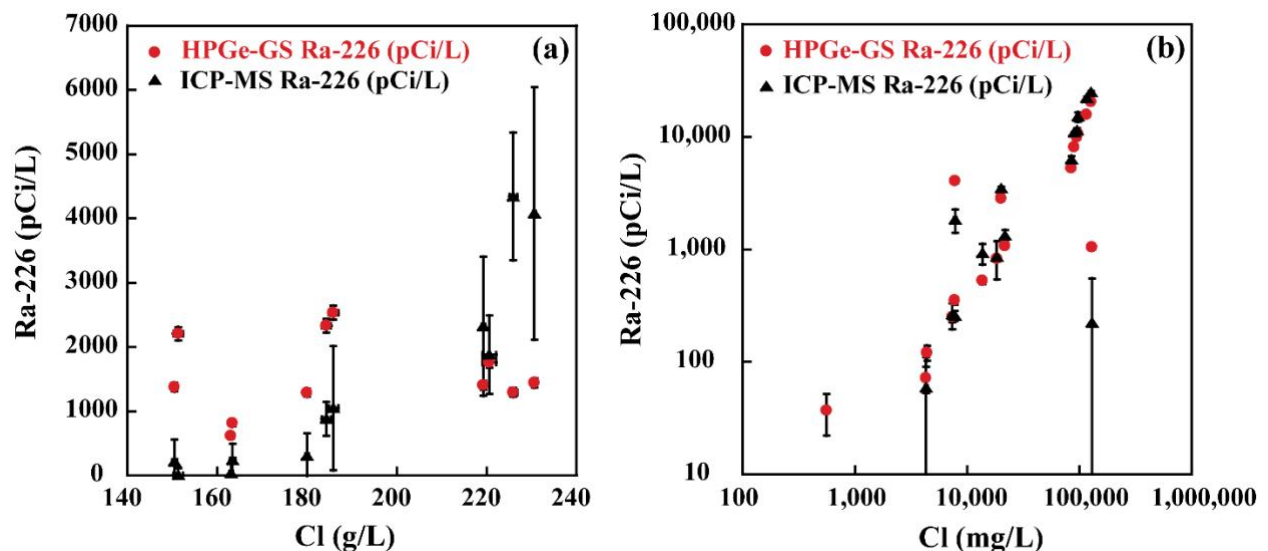


Figure 4.1: Ra-226 activity in Collingwood (a) and Antrim (b) produced water measured by ICP-MS and HPGe-GS. Error bars represent standard deviation of three measurements.

4.3.3 Ra activity in produced brine

As discussed previously, the primary Ra isotopes (Ra-226, Ra-228) in shale come from decay of U-238 and Th-232. Using equations 4.1 and 4.2 below, Ra-226 and Ra-228 activities can be calculated in source rocks according to secular equilibrium theory (Appendix C section C-4).¹⁵

$$[\text{Ra} - 226] = 3.58 \times 10^{-7} [\text{U} - 238] \quad (4.1)$$

$$[\text{Ra} - 228] = 4.11 \times 10^{-10} [\text{Th} - 232] \quad (4.2)$$

Typical ranges of U (1–13 ppm) and Th (2–47 ppm) concentrations in source rock show that shales, especially black shales, tend to have higher U and Th content than carbonate rocks or sandstone.³⁴ For example, Marcellus shale has an average U concentration of 26 ppm,³⁵ while a typical sandstone formation has a U concentration of 0.45 ppm.³⁶ Since the Ra isotopes in formation brines originate from U and Th in the rock, produced water samples from Marcellus shale (up to 18,000 pCi/L) should be higher in Ra than that from non-Marcellus shale formation in the Northern Appalachian Basin (up to 6700 pCi/L) given its relative enrichment in U and Th compared to typical shales.⁶

Once Ra source activities in shale are estimated from U, Th content following equations 4.1 and 4.2, the rock/water effective contact ratio between shale and formation water is needed to predict Ra activity in formation water. The actual rock/water ratio can be calculated using the formation's porosity and the water saturation, which can be obtained from well logs (Appendix C section C-1). Using this approach, the average rock/water ratios for three formations (Appendix C section C-1) were estimated to be ~140,000 g/L (with a high of ~180,000 for Marcellus and a low of ~90,000 for Antrim). The measured Ra 228/226 ratio for produced brine from the Collingwood and Antrim formations (Figure C5) were in good agreement with the calculated U/Th ratios for the shales (0.81 for Antrim and 0.1 for Marcellus, Table C1).

Finally, to estimate Ra activity in produced water, the amount of extractable Ra from the shale needs to be known (or assumed). Using a rock/water ratio of 140,000 g/L and assuming that 0.001–5% (with 5% considered as an upper bound³⁴) of the total Ra-226 in shale can be extracted by formation water, the Ra-226 activity as a function of U content from 0–30 ppm in shale was calculated (Figure 4.2). For comparison, measured Ra-226 activities in Utica-Collingwood and Antrim produced water samples, and Marcellus water compiled from other studies^{6,21,37,38} are also plotted in Figure 4.2. As shown in Figure 4.2, the wide range of Ra-226 activity found in produced water samples (from ~10–15,000 pCi/L), which vary by more than three orders of magnitude, cannot be explained simply due to the differences in the U content of different shales, which typically only vary over a range of 0–30 ppm (U content for the three formations is given in Table C1). Nor can it be explained by assuming a range of other typical rock/water ratios (Figure C1). This indicates that other factors must contribute to cause the wide variation of measured Ra activity in shale gas wastewaters.

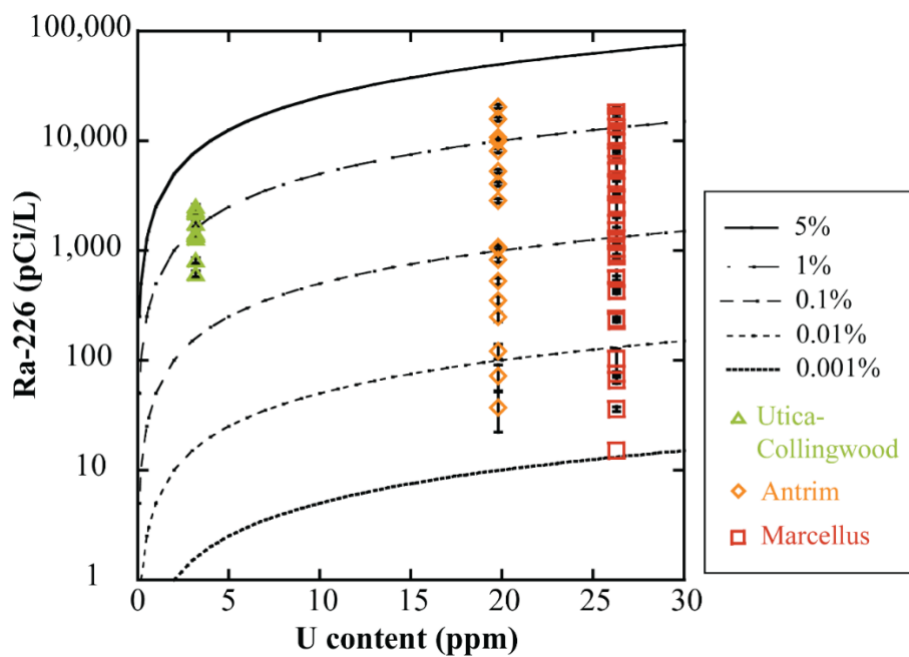


Figure 4.2: Predicted Ra-226 activity as a function of potential total Ra present in the shale for a given shale U content. Symbols represent produced water sample data from the Utica-Collingwood (triangle), Antrim (diamond), and Marcellus (square).

The U content and rock/water ratio used for the calculations presented in Figure 4.2 provide an upper limit for Ra-226 activity in the different formation waters. As such, additional possible parameter values or Ra sinks need to be considered in order to account for the more than three orders of magnitude variation in Ra content of Antrim and Marcellus shale produced water (Figure 4.2). Adsorption/desorption processes between formation water and shale minerals will influence the mobility of Ra and may help to explain the range of measured Ra(II) concentrations. In particular, the differences in the clay and organic content in shale, which provide adsorption sites for cation exchange, could cause differences in the amount of Ra(II) in produced waters among different shales due to competition between Ra and other cations for adsorption sites. This competitive adsorption/desorption process is discussed further in the following section.

4.3.3.1 Influence of shale cation exchange capacity

Clay mineral and solid organic matter components of shale with primarily negatively charged surface functional groups can adsorb and remove positively charged ions (e.g., Ca(II), Mg(II), Sr(II) and Ra(II)) from shale formation water. The CEC (meq/100g) of a shale is a measure of the number of exchangeable cation sites per 100g dry rock at a given pH value. The CEC depends primarily on clay type and content, and solid phase organic matter. The primary clay minerals present in shale, in general, are kaolinite, illite, smectite, chlorite, and kaolinite. These minerals have CEC values, respectively, on the order of 1–10, 10–40, 80–150, and <10 meq/100g.³⁹ Based on the clay type and content, the calculated CEC (Table C4) for shales used in this study was: Collingwood (6.5 meq/100g) < Utica (9.5) < Antrim (10) < Marcellus (11.4). These are similar to the average CEC measured by Staub⁴⁰ of 5.9 ± 1.36 meq/100g for Marcellus and 3.5 ± 1.08 meq/100g for Utica.

The clay mineral CEC does not necessarily reflect the total or actual reactivity of the clay. For example, some cations bind more strongly than others, and some cations may be in inaccessible sites and subsequently, less exchangeable.⁴¹ As such, the narrow range in CEC of the clays in this study suggest that inorganic clay minerals alone may not be a major contributor to the range in measured Ra activity in formation water. In general, the order of exchangeability of common cations for clay exchange sites has been reported as $\text{Li}^+ < \text{Na}^+ < \text{K}^+ < \text{Rb}^+ < \text{Cs}^+$ and $\text{Mg}^{2+} < \text{Ca}^{2+} < \text{Sr}^{2+} < \text{Ba}^{2+}$.⁴²

In addition to clay minerals present in shale, solid phase organic matter is also present and adds to the total CEC. The organic content of shale considered in this work is shown in Table C5 in which organic matter CEC ranges from ~200–300 meq/100g.³⁹ The Utica-Collingwood formation has lower TOC compared to the Antrim and Marcellus shale (Table C5). The measured CEC for several Marcellus shale samples are lower than CEC calculated based on clay type and content.⁴³ Given this, the contribution of organic matter to CEC is considered to be negligible. Quantifying the accessible Ra exchange sites (clay plus organic) in different shale samples is more important than accurately estimating the total clay CEC for all cations present. To do this, the amount of Ra that could adsorb was estimated by using Ba as a proxy. Adsorption of Ba by the Antrim, Marcellus, Utica and Collingwood shales is shown in Figure 4.3. The uptake of Ba conforms to Langmuir isotherm adsorption behavior, with an initial steep increase in adsorbed Ba with increasing barium concentration in solution leading to a maximum plateau value (akin to the CEC) at high Ba solution concentration. According to Figure 4.3, the Marcellus and Collingwood samples have similar, but relatively lower, estimated Ba maximum uptake values compared to the Utica and Antrim. The estimated CEC of Marcellus (2 meq/100g-shale, Table C4) from Figure 4.3 is nearly one order of magnitude lower than the value calculated based on clay content (11.4 meq/100g, Table C4), but still within the CEC range from a previous study.^{43,44} The Ba CEC values for the Antrim, Utica,

and Collingwood are close to the estimates based on clay mineral content (Table C4). The relatively small differences in the shale CEC cannot account for the several orders of magnitude Ra activity variation measured in produced water from the Antrim and Marcellus shale formations.

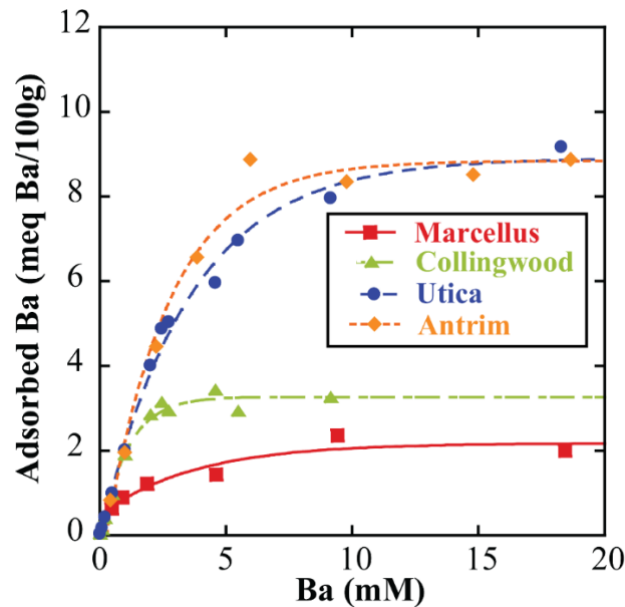


Figure 4.3: Estimated shale cation exchange capacity based on Ba adsorption titration.

4.3.3.2. Influence of formation water salinity

Another component of formation water that can impact dissolved Ra is the TDS value, which reflects the concentration of dissolved salts in the water. High TDS often indicates extremely high concentrations of monovalent Na^+ as well as relatively high concentration of divalent cations including Ca^{2+} , Mg^{2+} , Sr^{2+} , and Ba^{2+} , which may compete with Ra^{2+} for the cation exchange sites in the shale matrix. For a given shale formation, Ra activity in formation water has been found to be positively correlated with TDS.⁶ As TDS increases, Ra^{2+} is thought to increase in the produced water as a result of being outcompeted for exchange sites by Na^+ and divalent cations. To verify this, experiments were conducted to quantify the amount of Ba (again serving as a proxy for Ra) desorbed from shales as a function of increasing TDS with NaCl concentrations ranging from 0.1– 5 M. As shown in Figure 4.4, an upper bound of

desorbed Ba is achieved with increasing NaCl concentration, representing the total amount of Ba that can be desorbed from the shale samples. Interestingly, the Marcellus shale had the highest amount of Ba desorbed while Collingwood had the lowest (Figure 4.4), even though the Marcellus CEC was found to be the lowest among the different shale samples of this study. This suggests the Marcellus had exchange sites with higher affinity for Ba. Overall, the small range of values for maximal desorption (from ~2 to 7 ug-Ba/g-shale) suggests the differences in Ba (and by proxy Ra) uptake and desorption is not that different among the shale samples investigated.

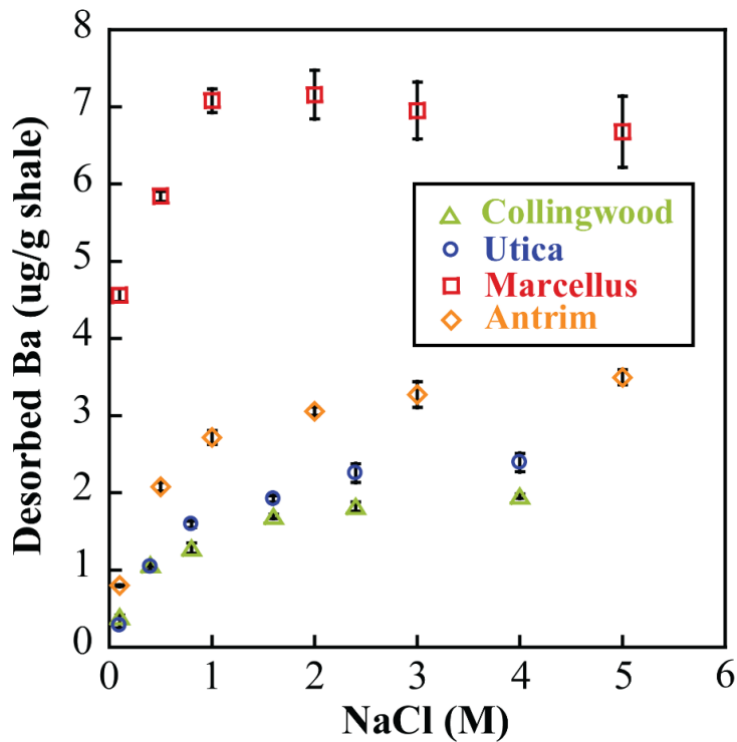


Figure 4.4: Ba desorbed from four different shales as a function of increasing NaCl concentration.

The TDS levels of produced brines can vary by three to four orders of magnitude within the same formation such as the Marcellus shale.²⁰ By plotting dissolved Ra-226 activity vs. TDS for samples of Antrim produced brines (Figure 4.5a), a clear positive correlation between Ra activity and TDS in produced brines. The linear regression fit of the Antrim produced water

data is given in Equation 4.3 ($R^2 = 0.98$) and is shown in Figure 4.5(a) as a solid black line. A theoretical correlation in Equation 4.4 can be used to describe Ra-226 activity as a function of U content, CEC, and TDS. Based on the closeness in values of CEC among the Marcellus, Collingwood and Antrim samples (the average CEC for the range of samples tested), direct inclusion of CEC in the empirical correlation given by Equation 4.4 was neglected. Equation 4.5 was then developed based on linear coefficient from the Antrim correlation (Equation 4.3) and the average U content of the Antrim formation. The resulting equations 4.5 can be used to predict Ra activity in produced waters based primarily on known TDS of the formation water.

$$\log(\text{Ra-226 (pCi/L)}) = 1.35\log(\text{TDS (mg/L)}) - 3.03 \quad (R^2=0.98) \quad (4.3)$$

$$\log(\text{Ra-226})=a*\log(\text{TDS})-b*\log(\text{CEC})+c*\log(\text{U content})+d \quad (4.4)$$

$$\log(\text{Ra-226 (pCi/L)}) = 1.35\log(\text{TDS (mg/L)}) + \log(\text{U content (mg/g)}) - 4.44 \quad (4.5)$$

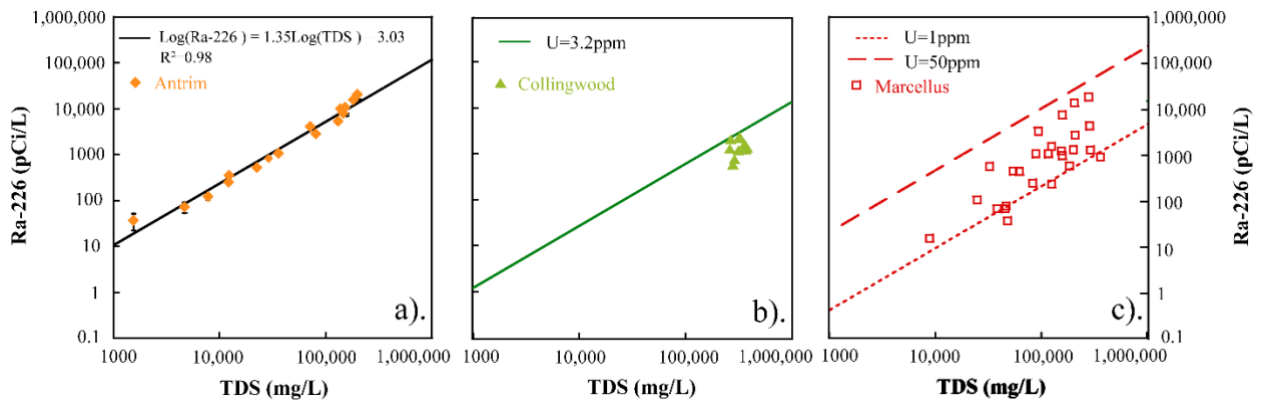


Figure 4.5: Correlation of Ra-226 activity with TDS for produced water samples from the (a) Antrim, (b) Collingwood, and (c) Marcellus formations.

The Collingwood has a lower U content than the Antrim shale and this contributes to the observed lower Ra activity at similar TDS levels compared to the Antrim brine samples. Equation 4.5 is plotted by using average Collingwood U content in Figure 4.5b together with

flowback water Ra-226 activities from a single Collingwood well in this study. The solid green line in Figure 4.5b matches with Collingwood samples well, which supports that equation 4.5 can be used to predict Ra-226 activity on known TDS of flowback water. For Marcellus shale, a typical range of U content is 1 to 50 ppm³⁵ and is used to bracket the scattered Marcellus water data shown in Figure 4.5(c) following application of Equation 4.5. Because the Marcellus brine data are gathered from the literature from spatially dispersed wells of varying depths, there is much greater variance in CEC and U content of the shale associated with these samples. This leads to the greater degree of scatter in these data and results in a poorer correlation between Ra activity and produced water TDS for the Marcellus samples. Even so, there is still a clear indication that increasing TDS correlates with increased Ra activity in Marcellus produced brine.

TDS is the strongest predictor of Ra activity and can largely account for changes of over three orders of magnitude in Ra activity. The average Marcellus samples, with generally higher CEC and greater adsorption capacity for removing Ra from water, have lower Ra activity than Antrim produced water samples with similar TDS (Figure 4.5c and 4.5a). Future efforts could more explicitly incorporate shale CEC into estimates of produced brine Ra-226 activity by starting with Equation 4.4 for shales that may have a significantly lower or higher CEC than the three shales used here.

4.3.3.3. Influence of sulfate

Barite precipitation may also impact Ra activity in produced brine due to Ra co-precipitation with Ba in $(\text{Ba,Ra})\text{SO}_4(\text{s})$.⁴⁵ Typical sulfate levels in shale formation waters are quite low (~1ppm or below detection limits measured in this study). Sulfate concentration is also often well below that of Ba, suggesting that sulfate is limited by barite solubility and the reducing conditions expected to be found in organic-rich shale reservoirs. Growth of sulfur

oxidizing bacteria after introduction of oxic hydraulic fracturing fluids into the shale is often inhibited through the use of biocides,⁴⁶ so sulfate production from sulfide mineral oxidation after hydraulic fracturing is unlikely to produce enough sulfate to promote significant barite precipitation and concomitant removal of Ra from shale brines.

Plotting Ra-226 activity and TDS of Antrim produced water samples (Figure C6) reveals a clear positive trend with one notable outlier: an Antrim sample with far lower Ra-226 activity (highlighted in red) than indicated by the trend line. It is noted that this outlier and had much higher sulfate levels (62.3 ppm, Table C6) compared to all the other Antrim samples (<2 ppm, Table C6). This indicates that in some exceptional cases sulfate may be at high enough concentration to influence Ra activity through removal via sulfate-promoted barite precipitation. As such, sulfate concentration should be monitored during initial reservoir assessment to be sure that barite precipitation can be ruled out as a potential control on Ra activity in produced shale gas brines (and to assess whether scaling problems from barite precipitation in wells are likely to be of concern).

4.4 Environmental implications

This study provides a simple predictive tool for estimating Ra activity in shale gas produced waters. Ra activity in produced brine is a function of the U content, Th content, and CEC of a given shale, as well as the TDS and sulfate concentrations of the formation water. TDS, together with sulfate, has been shown to be the key factor for predicting Ra activity in produced brine for a given shale composition. The strong correlation between TDS and Ra activity in produced water samples from two different shale formations was used to develop and validate an empirical equation for estimating the expected Ra activity in shale gas produced brines (Equation 4.5). The U content of a target reservoir can be reasonably obtained via spectral gamma-ray well logs and formation water TDS is often known or can be easily

measured. Given this information, the linear correlation developed here provides a direct method to predict Ra activity in produced brines prior to shale gas production. Knowing *a priori* which wells are likely to produce brines with elevated Ra activity could help to optimize wastewater treatment and disposal strategies for future shale gas plays and serve to reduce hazards associated with the handling of shale gas derived TENORM waste streams.

4.5 References:

- (1) Escott, P. *The Occurrence of Radioactive Contamination on Offshore Installations*. NRPB report for the Department of Energy, London, 1984.
- (2) Otto, G. H. *A National Survey on Naturally Occurring Radioactive Material (NORM) in Petroleum Production and Gas Processing Facilities*. American Petroleum Institute, 1997.
- (3) Bou-Rabee, F.; Al-Zamel, A. Z.; Al-Fares, R. A.; Bem, H. Technologically Enhanced Naturally Occurring Radioactive Materials in the Oil Industry (TENORM). *Nukleonika* **2009**, *54*, 3–9.
- (4) Nelson, A. W.; Eitrheim, E. S.; Knight, A. W.; May, D.; Mehrhoff, M. A.; Shannon, R.; Litman, R.; Burnett, W. C.; Forbes, T. Z.; Schultz, M. K. Understanding the Radioactive Ingrowth and Decay of Naturally Occurring Radioactive Materials in the Environment: An Analysis of Produced Fluids from the Marcellus Shale. *Environ. Health Perspect.* **2015**, *123* (7), 689–696.
- (5) Gregory, K. B.; Vidic, R. D.; Dzombak, D. A. Water Management Challenges Associated with the Production of Shale Gas by Hydraulic Fracturing. *Elements* **2011**, *7* (3), 181–186.
- (6) Rowan, E. L.; Engle, M. A.; Kirby, C. S.; Kraemer, T. F. *Radium content of oil-and gas-field produced waters in the northern Appalachian Basin (USA)—Summary and discussion of data*. No. 2011-5135. US Geological Survey, 2011.
- (7) Haluszczak, L. O.; Rose, A. W.; Kump, L. R. Geochemical Evaluation of Flowback Brine from Marcellus Gas Wells in Pennsylvania, USA. *Appl. Geochem.* **2013**, *28*, 55–61.

- (8) Warner, N. R.; Christie, C. A.; Jackson, R. B.; Vengosh, A. Impacts of Shale Gas Wastewater Disposal on Water Quality in Western Pennsylvania. *Environ. Sci. Technol.* **2013**, *47* (20), 11849–11857.
- (9) Zimmerle, W. and Zimmerle, H., *Petroleum sedimentology*. Springer Science & Business Media. 1995.
- (10) Swanson, V. E. *Geology and geochemistry of uranium in marine black shales: a review*. Washington, DC: US Government Printing Office, 1961.
- (11) Gott, G. B. *Inferred relationship of some uranium deposits and calcium carbonate cement in southern Black Hills, South Dakota*. No. 1046. US Government Printing Office, 1956.
- (12) Fisher, R. S. Geologic, Geochemical, and Geographic Controls on NORM in Produced Water from Texas Oil, Gas, and Geothermal Reservoirs. *SPE Adv. Technol. Ser.* **1996**, *4* (02), 94–100.
- (13) Hammond, D. E.; Zukin, J. G.; Ku, T.-L. The Kinetics of Radioisotope Exchange Between Brine and Rock in a Geothermal System. *J. Geophys. Res. Solid Earth* **1988**, *93* (B11), 13175–13186.
- (14) Baird, R.; Merrell, G.; Klein, R.; Rogers, V.; Nielson, K. *Management and Disposal Alternatives for Norm Wastes in Oil Production and Gas Plant Equipment*; American Petroleum Institute, 1990.
- (15) Zhang, Y. *Geochemical Kinetics*; Princeton University Press, 2008.
- (16) Smith, K. P.; Blunt, D. L.; Williams, G. P.; Tebes, C. L. *Radiological Dose Assessment Related to Management of Naturally Occurring Radioactive Materials Generated by the Petroleum Industry*; Society of Petroleum Engineers. 1996.
- (17) Kerr, R. A. Natural Gas From Shale Bursts Onto the Scene. *Science* **2010**, *328* (5986), 1624–1626.

- (18) Kargbo, D. M.; Wilhelm, R. G.; Campbell, D. J. Natural Gas Plays in the Marcellus Shale: Challenges and Potential Opportunities. *Environ. Sci. Technol.* **2010**, *44* (15), 5679–5684.
- (19) Vengosh, A.; Jackson, R. B.; Warner, N.; Darrah, T. H.; Kondash, A. A Critical Review of the Risks to Water Resources from Unconventional Shale Gas Development and Hydraulic Fracturing in the United States. *Environ. Sci. Technol.* **2014**, *48* (15), 8334–8348.
- (20) Barbot, E.; Vidic, N. S.; Gregory, K. B.; Vidic, R. D. Spatial and Temporal Correlation of Water Quality Parameters of Produced Waters from Devonian-Age Shale Following Hydraulic Fracturing. *Environ. Sci. Technol.* **2013**, *47* (6), 2562–2569.
- (21) Nelson, A. W.; May, D.; Knight, A. W.; Eitrheim, E. S.; Mehrhoff, M.; Shannon, R.; Litman, R.; Schultz, M. K. Matrix Complications in the Determination of Radium Levels in Hydraulic Fracturing Flowback Water from Marcellus Shale. *Environ. Sci. Technol. Lett.* **2014**, *1* (3), 204–208.
- (22) Zielinski, R. A.; Otton, J. K. *Naturally Occurring Radioactive Materials (NORM) in Produced Water and Oil-Field Equipment: An Issue for Energy Industry*; US Department of the Interior, US Geological Survey, 1999.
- (23) Lauer, N. E.; Warner, N. R.; Vengosh, A. Sources of Radium Accumulation in Stream Sediments near Disposal Sites in Pennsylvania: Implications for Disposal of Conventional Oil and Gas Wastewater. *Environ. Sci. Technol.* **2018**, *52* (3), 955–962.
- (24) Bateman, H. The Solution of a System of Differential Equations Occurring in the Theory of Radioactive Transformations; 1910; Vol. 15, pp 423–427.
- (25) W. Nelson, A.; J. Johns, A.; S. Eitrheim, E.; W. Knight, A.; Basile, M.; Iii, E. A. B.; K. Schultz, M.; Z. Forbes, T. Partitioning of Naturally-Occurring Radionuclides (NORM)

- in Marcellus Shale Produced Fluids Influenced by Chemical Matrix. *Environ. Sci. Process. Impacts* **2016**, 18 (4), 456–463.
- (26) Zhang, T.; Hammack, R. W.; Vidic, R. D. Fate of Radium in Marcellus Shale Flowback Water Impoundments and Assessment of Associated Health Risks. *Environ. Sci. Technol.* **2015**, 49(15), 9347-9354.
- (27) Osborn, S. G.; McIntosh, J. C. Chemical and Isotopic Tracers of the Contribution of Microbial Gas in Devonian Organic-Rich Shales and Reservoir Sandstones, Northern Appalachian Basin. *Appl. Geochem.* **2010**, 25 (3), 456–471.
- (28) Zhang, T.; Bain, D.; Hammack, R.; Vidic, R. D. Analysis of Radium-226 in High Salinity Wastewater from Unconventional Gas Extraction by Inductively Coupled Plasma-Mass Spectrometry. *Environ. Sci. Technol.* **2015**, 49 (5), 2969–2976.
- (29) 4B2 - STD - Lithium Metaborate/Tetraborate Fusion - ICP/MS - Geochemistry / Assay Actlabs.<http://www.actlabs.com/page.aspx?page=515&app=226&cat1=549&tp=12&lk=no&menu=64>.
- (30) Genie 2000 Software Family - CANBERRA Industries
http://www.canberra.com/products/radiochemistry_lab/genie-2000-software.asp.
- (31) Zhang, T. Origin and Fate of Radium in Flowback and Produced Water from Marcellus Shale Gas Exploration Ph.D. Dissertation, University of Pittsburgh, 2015.
- (32) Langmuir, D.; Riese, A. C. The Thermodynamic Properties of Radium. *Geochim. Cosmochim. Acta* **1985**, 49 (7), 1593–1601.
- (33) Blum, P.; Rabaute, A.; Gaudon, P.; Allan, J. F. Analysis of Natural Gamma-Ray Spectra Obtained from Sediment Cores with the Shipboard Scintillation Detector of the Ocean Drilling Program: Example from Leg 1561; *Proceedings of the Ocean Drilling Program. Scientific Results*. Vol. 156. 1997.

- (34) Adams, J. A.; Osmond, J. K.; Rogers, J. J. The Geochemistry of Thorium and Uranium. *Phys. Chem. Earth* **1959**, *3*, 298–348.
- (35) US EPA, Trace Metal Geochemistry and Mobility in the Marcellus Shale
<https://www.epa.gov/hfstudy/trace-metal-geochemistry-and-mobility-marcellus-shale>.
- (36) Turekian, K. K.; Wedepohl, K. H. Distribution of the Elements in Some Major Units of the Earth's Crust. *GSA Bull.* **1961**, *72* (2), 175–192.
- (37) Ziemkiewicz, P. F.; Thomas He, Y. Evolution of Water Chemistry during Marcellus Shale Gas Development: A Case Study in West Virginia. *Chemosphere* **2015**, *134*, 224–231.
- (38) Dresel, P. E.; Rose, A. W. Chemistry and Origin of Oil and Gas Well Brines in Western Pennsylvania. *Open-File Rep. OFOG* 2010, *10*, 01-0.
- (39) Drever, J. I.; Marion, G. The Geochemistry of Natural Waters: Surface and Groundwater Environments. *J. Environ. Qual.* **1998**, *27* (1), 245–245.
- (40) Staub, P. Clay Mineralogy of the Marcellus and Utica Shales: Implications for Fluid Development via Cation Exchange. M.S. thesis, University of New York at Buffalo, 2014.
- (41) Breeden, D.; Shipman, J. Shale Analysis for Mud Engineers; AADE Drilling Fluids Conference, Texas, 2004.
- (42) Carroll, D. Ion Exchange in Clays and Other Minerals. *Geol. Soc. Am. Bull.* **1959**, *70* (6), 749–779.
- (43) Derkowski, A.; Marynowski, L. Reactivation of Cation Exchange Properties in Black Shales. *Int. J. Coal Geol.* **2016**, *158* (Supplement C), 65–77.
- (44) Abdulsattar, Z. R.; Agim, K.; Lane, R. H.; Hascakir, B. Physicochemical Interactions of Source Rocks with Injected Water-Based Fluids; Ph.D. Dissertation, Texas A&M University, 2015.

- (45) Zhang, T.; Gregory, K.; Hammack, R. W.; Vidic, R. D. Co-Precipitation of Radium with Barium and Strontium Sulfate and Its Impact on the Fate of Radium during Treatment of Produced Water from Unconventional Gas Extraction. *Environ. Sci. Technol.* **2014**, *48* (8), 4596–4603.
- (46) Kahrilas, G. A.; Blotevogel, J.; Stewart, P. S.; Borch, T. Biocides in Hydraulic Fracturing Fluids: A Critical Review of Their Usage, Mobility, Degradation, and Toxicity. *Environ. Sci. Technol.* **2014**, *49* (1), 16–32.

Chapter 5

Concluding Remarks

The goal of this dissertation was to provide a comprehensive understanding of the potential to mobilize trace elements and radionuclides due to water-rock interactions between shales and HF fluids. This objective was achieved through a combination of experimental observations, field sample comparisons, image analyses, and geochemical modelling.

Batch experiment results in Chapter 2 demonstrated that low pH conditions caused by the addition of strong acids in synthetic HF fluids had the largest impact on element mobilization. The addition of oxidants, often added as gel-breakers in HF fluids, further enhanced the dissolution of reduced mineral phases such as pyrite, and concomitant release of As and U. For pulverized shale samples in this leaching study, all minerals are always under maximum accessibility and interact efficiently with HF fluids. Under such conditions, carbonate mineral dissolution was found to buffer the pH and thereby lower the potential of the strong acids to promote element leaching of other less reactive non-carbonate minerals. However, carbonates were also shown to serve as a source of trace elements. This portion of trace elements can be released from the shale matrix during carbonate dissolution. Compared to powder samples used in the batch experiments to study maximum element leaching potential, the core flooding experiments in Chapter 3 examined the role of mass transport limitations and mineral spatial heterogeneity in controlling mineral dissolution processes.

In order to assess the effect of carbonate mineral dissolution on As leaching, two core flooding flow-through experiments were carried out and a reactive transport model was developed to explore longer timeframes and spatial domains. When HF fluid is continuously

injected through the carbonate-rich core, mineral dissolution is controlled through a combination of mineral surface reaction and element mass transport processes. During the flow through experiments substantial carbonate mineral dissolution occurred along the fracture pathway and was coincident with an increasing rate of As release over time. Post-reaction SEM analysis demonstrated the co-occurrence of calcite-depleted regions and the exposure of pyrite at the fracture face. These observations indicate that fast erosion of calcite by the acidic HF fluids increases the accessibility of other less soluble minerals exposed to the oxic influent fluids, which has been validated through reactive transport modelling. This combination of acid-driven and oxidative dissolution processes enhanced the As leaching rate from the fractured shale.

Furthermore, analysis of the reactive transport modelling results highlighted that mass transport process always controlled element leaching during flow of the HF fluids. Fast carbonate mineral dissolution is mainly limited by diffusive mass transport. While for pyrite dissolution within the calcite-depleted layer, surface reaction rate limitations play an important role in controlling mineral dissolution rates in addition to diffusive mass transport. The fast dissolving calcite increases pyrite reactive area as well as through enhanced porosity within the shale matrix, which all enhance As mobilization due to pyrite dissolution. However, over longer timeframes both processes will eventually diminish following the continuously decreasing carbonate dissolution rate. Based on the experimental results presented in Chapters 2 and 3, it is clear that the carbonate content of a given shale reservoir will have a strong influence on the extent of HF motivated release of trace element from shale reservoirs.

Comparison of the flowback water composition from a shale gas well in the same formation to the batch leaching experiments in Chapter 2 revealed no measurable concentrations of some of the toxic elements observed in the flowback water (e.g., Ra), even at relatively high rock/water ratios similar to those expected in shale gas formations. This

comparison suggests that although shale minerals are the ultimate source of contaminants observed in flowback waters a majority of these elements are likely already present in shale connate brines prior to well stimulation.

All the results from this study demonstrate that toxic metal leaching may not be the most challenging factor facing proper management of flowback/produced water. The elevated level of radium activity in produced brine might ultimately control the optimal treatment strategy for shale gas produced brines. In Chapter 4, a rapid ICP-MS method for Ra measurement of field samples was developed to replace the time-consuming HPGe-Gs Ra measurement method. This chapter also focused on evaluating the controlling parameters determining Ra activity in produced brine. An empirical relationship was developed to predict Ra in produced brine prior to shale gas development in an effort to wastewater management strategies. U and Th in shale is known to be the ultimate source of Ra and after Ra has reached secular equilibrium from radioactive decay of its parent and daughter decay isotopes, the main process believed to control fate of Ra in formation brines is adsorption/desorption on mineral surfaces.

After investigating all possible controlling parameters for Ra mobility, it was clear that formation brine salinity (TDS) is the most important factor controlling Ra activity in produced brine. High levels of Ra in flowback water are found when the rock CEC is small and the TDS is high. In addition to TDS being the controlling factor for Ra mobilization, barite precipitation will also affect Ra activity in produced brine. The Ra level in produced brine will be much lower if the sulfate concentration is high enough to promote precipitation of barite, which will incorporate Ra within the barite solid. An empirical correlation between TDS, U content and Ra activity was developed to predict Ra activity in flowback/produced water. By following the approach presented in this study, Ra activity in produced brines can be estimated through a simple analysis of shale brine TDS and native U content.

In addition to being a guideline for estimating the level of potential elements of concern during shale gas production process, the investigative approaches applied in this dissertation can also be used to study trace element and radionuclide mobilization during water/rock interactions (dissolution/precipitation, adsorption/desorption, mass transport) during development of other emerging subsurface energy resource activities.

Appendices

Appendix A

Supplemental data and figures for Chapter 2:

Abbreviation:

DI water ultrapure DI water

No acid ammonium persulfate, choline chloride

Acid only hydrochloric acid, citric acid

HF Fluids hydrochloric acid, ammonium persulfate, citric acid, choline chloride

A-1: Estimation of rock: water ratio

The rock: water ratio chosen for batch experiments should be similar to the real ratio of shale gas production wells. The contact surface area is the most important factor for mineral dissolution. A certain surface area of shale is in contact with certain volume of injected HF fluids is what we try to match in batch experiments. Two assumptions were made: 1) the system only contains a single fracture, which supported by sphere proppant; 2) the total volume of this fracture is the volume of the injected HF fluids. The equation below was used to calculate water-rock ratio.

$$\frac{m_{rock}}{V_{water}} = \frac{\left(\frac{\text{Total surface area}}{\text{Specific area of shale sample}} \right)}{V_{water}}$$

The specific area of our samples are 2 m²/g. The range of proppant sizes is from 0.1 millimeter in diameter to over 2 millimeters in diameter depending customer specifications.¹ The rock: water ratio is then between **0.01-20 g/L**. Since most of the proppant is between 0.4 and 0.8 millimeters in size¹, the rock: water ratio is **2.5-5 g/L**. **10 g/L** was chosen as rock: water ratio in all batch experiments.

A-2: Procedure and results of sequential extraction

The first step in the sequential extraction targets water-soluble salts by mixing ultrapure DI water with powdered shale with a rock: water ratio of 30ml/1g. All samples were covered and kept in a temperature controlled (25°C) shaker for 8 hours, then centrifuged. The supernatant was then filtered through a 0.22 µm PTFE filter prior to further analysis. The second step extracted exchangeable cations by adding 8 ml of ammonium acetate. These samples were agitated in a temperature-controlled shaker for 5 hours, then centrifuged and filtered. The third step was followed by adding 8% ultrapure acetic acid (ThermoFisher 64-19-7) until a pH of 5 was reached. This acidification procedure targets metals partitioned to carbonate mineral phases. After 5 hours in the shaker the samples were centrifuged and then filtered. The last extraction step aims to extract trace metals from reduced phases, such as sulfide minerals, and from organic matter by using a 30% hydrogen peroxide solution and reducing the pH to 2 via nitric acid addition. Hydrogen peroxide was added repeatedly until bubbling was no longer observed, demonstrating complete oxidation of reduced phases and organic material. In this final extraction step, the samples were heated to 80°C and continuously shaken for 8 hours. After cooling, the last procedure is to centrifuge and filter the eluent and then dilute with DI water to a final volume of 50 mL. All extraction samples were taken and immediately refrigerated for anion analysis, while the remaining eluent was acidified by nitric acid to a pH of 2 prior to performing cation analysis via ICP-MS.

Table A2-1: Extraction percentages of sequential extraction results

		Water Soluble (%)	Exchangeable Sites (%)	Carbonate (%)	Reduced Phases (%)	Total Available (mg/kg)
Na	Antrim	76	7	1	6	1,683
	Utica	70	11	2	12	512
	Collingwood	19	3	44	8	622
Mg	Antrim	3	12	14	48	5,058
	Utica	1	3	16	65	9,788
	Collingwood	1	4	70	22	7,090
K	Antrim	8	8	1	16	3,558
	Utica	21	15	1	13	4,200
	Collingwood	20	15	4	29	1,744
Ca	Antrim	13	35	22	12	7,729
	Utica	4	28	40	28	19,809
	Collingwood	<1	3	95	2	216,524
Sr	Antrim	6	29	3	9	43
	Utica	14	38	18	27	71
	Collingwood	1	7	74	3	752
Ba	Antrim	<1	26	3	18	21
	Utica	1	21	4	21	17
	Collingwood	1	25	30	19	13
Fe	Antrim	<1	<1	1	84	27,924
	Utica	<1	<1	5	77	28,132
	Collingwood	<1	<1	13	79	7,121
As	Antrim	<1	<1	<1	75	30
	Utica	<1	<1	1	84	4
	Collingwood	<1	<1	5	93	2
U	Antrim	<1	8	7	45	17
	Utica	11	4	3	72	0.3
	Collingwood	7	3	43	42	1

A-3: Batch experiment list

The following table shows all the batch experiments conducted in this study with different parameters setting.

Table A3-1: Batch experiments conducted in this study

Experimental conditions Fluid composition	Ambient conditions (0.101 MPa, 23°C)	10 MPa, 34°C	15 MPa, 43°C
MilliQ water with no chemical additives	3 UC	3 C 3 U 3 UC 2 A	3 UC
Citric acid, HCl		3 UC 2 A	
Choline chloride, ammonium persulfate		3 UC 2 A	
Choline chloride, ammonium persulfate, citric acid, HCl	3 UC 2 U 2 C 2 A	3 UC 2 C 2 U 3 A	3 UC 2 A

Formation name abbreviations: 1:1 Utica-Collingwood mixture (UC); Collingwood

(C); Utica (U); Antrim (A); the number before U, A, C, UC all indicates the number of experiments conducted.

A-4: Images of presence of pyrite framboid in three shale samples

The following figures (Figure A4-1, A4-2, A4-3) demonstrate the presence of pyrite in all shale samples in addition to XRD data (Table A1).

Figure A4-1: Scanning electron micrograph and selective elemental maps of Utica thin sections:

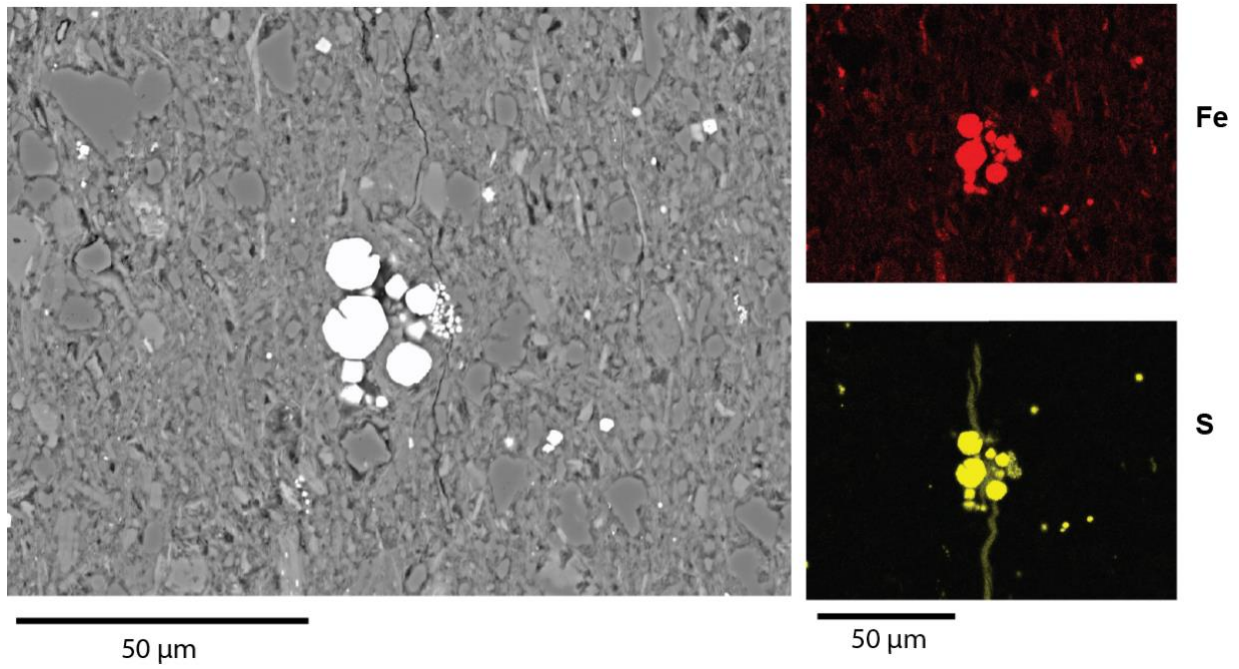


Figure A4-2: Scanning electron micrograph and selective elemental maps of Collingwood powder sample:

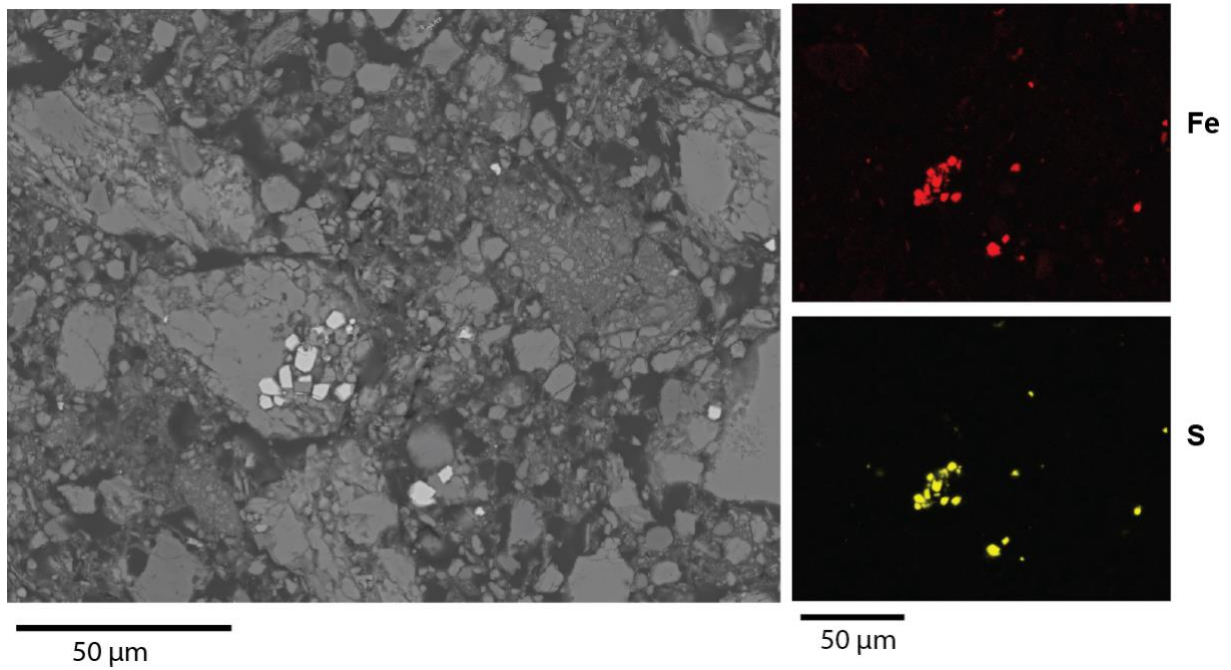
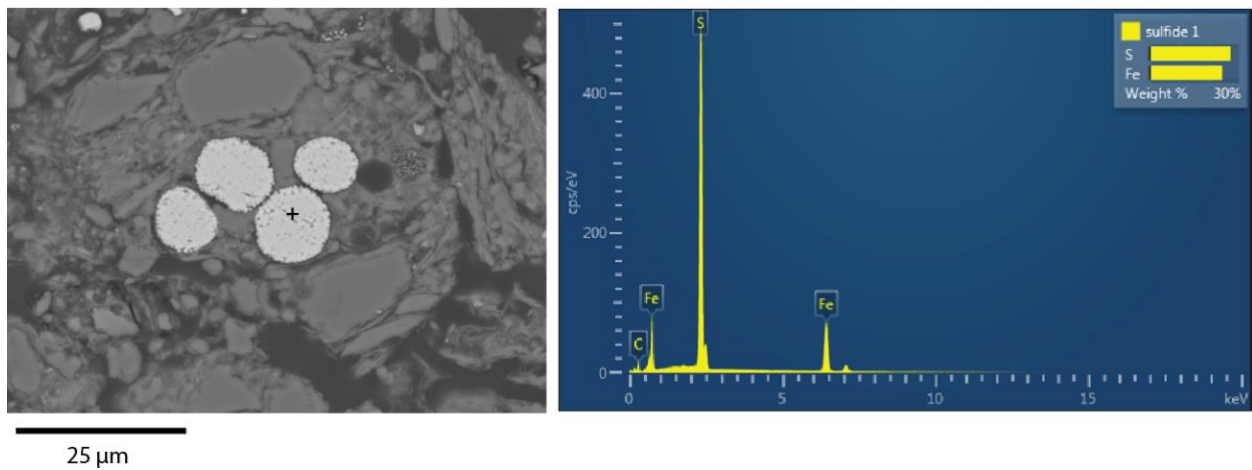


Figure A4-3: Scanning electron micrograph of Antrim powder sample and Energy dispersive X-ray spectroscopy (EDS) spectrum of pyrite grain:



A-5: Adjusted equilibrium constants at different P and T

The following tables (Table A5-1, A5-2) demonstrate the major mineral dissolution reactions calculated equilibrium constants at variable T, P conditions. The equilibrium constants influenced by elevated T, P is very small.

Table A5-1: Reactions and equilibrium constants of mineral dissolution reaction

Mineral Dissolution Reaction	Log Ksp		
	0 km depth Ambience T and P	1 km depth 34 °C / 10 MPa	1.5 km depth 43 °C / 15 MPa
$CaCO_3(s) \rightarrow Ca^{2+} + CO_3^{2-}$	-8.480	-8.479	-8.502
$BaSO_4(s) \rightarrow Ba^{2+} + SO_4^{2-}$	-9.970	-9.764	-9.577

Table A5-2: Parameters used in equilibrium constant calculation:

	LogK	ΔH^0 (kJ/mol)	ΔV^0 (cm ³ /mol)
Calcite dissolution	-8.47 ²	-9.61 ²	-29.7 ³
Barite dissolution	-9.97 ²	26.568 ²	-51.4856 ⁴

A-6: Extraction percentages of Ba, Fe, Mg, As

The extraction percentages of Ba, Fe, Mg, As of three different shales (Antrim, Utica, Collingwood) in contact with synthetic HF fluids are expressed in Figure A6.

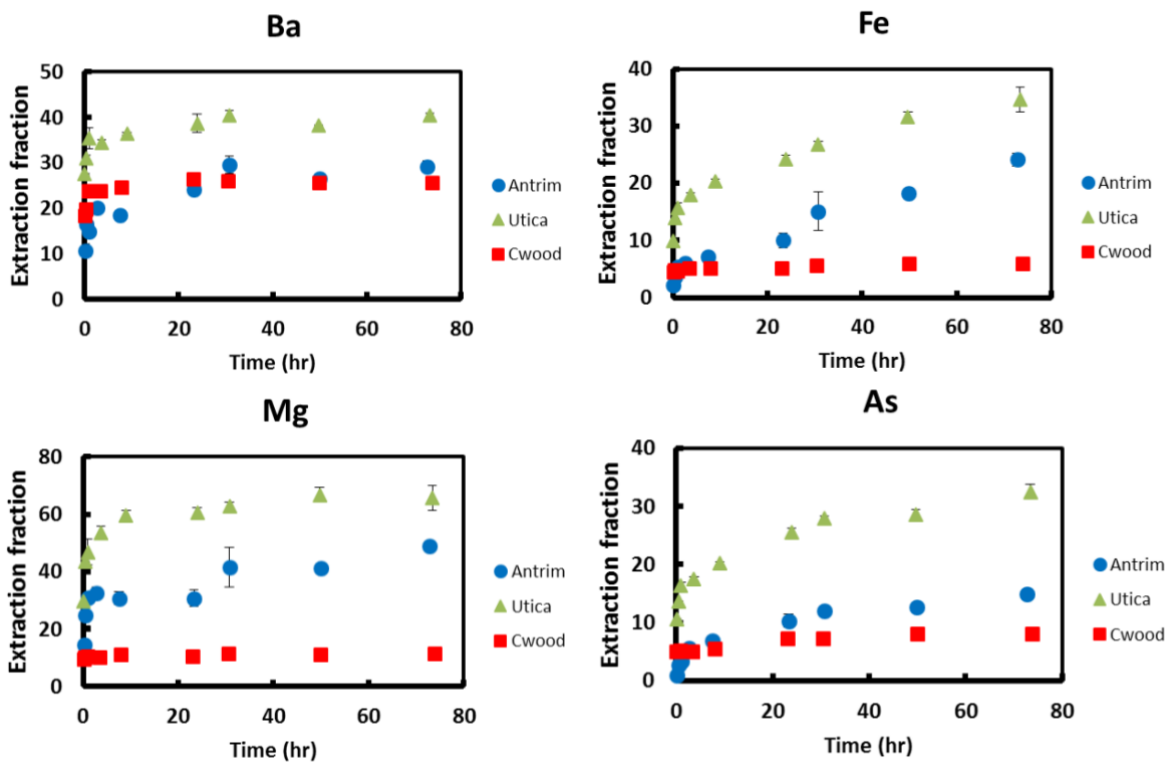


Figure A6: Extraction percentages ($Me/M_{e_{total}}$) of Ba, Fe, Mg, As from Utica, Collingwood and Antrim shale after contact with synthetic HF fluids (composition shown in Table 2) at 1.0 km T, P conditions and a rock: water ratio of 10 g/L.

A-7: Buffering capacity of shale

Buffer capacity of soil is defined as a soil's ability to maintain a constant pH level during addition of an acidifier or alkalescent agent.⁵ The definition for soil buffering capacity is adopted for shale buffering capacity. There are several mineral phases in shale such as carbonates can consume acid and maintain pH value. For the sake of simplicity, calcium is assumed only exist in calcite and calcite is the only mineral providing buffering capability. The following equation was adopted.

$$\text{Buffering capacity} = \frac{\text{mmol } \{H^+\}}{\text{g shale}} = \frac{2 \text{ mmol } \{H^+\}}{\frac{1 \text{ mmol } CO_3^{2-} * 0.1 \text{ g/mmol}}{\text{calcite percentage in shale}}} = \frac{20 \text{ mmol } \{H^+\}}{\text{Calcite percentage in shale}}$$

Table A7-1 shows the calculated calcite content and buffering capacity of different rock samples.

Table A7-1: Buffering capacity

	Calculated Calcite Content	Buffering Capacity [mmol{H⁺}/kg]
Utica	5%	1
Collingwood	54%	10.8
Antrim	1.9%	0.4

A-8: Eh and pH profiles

Eh and pH values of all batch experiments were recorded every 10 min. The following four figures (Figure A8-1, A8-2, A8-3, A8-4) illustrated Eh and pH profiles for Utica-Collingwood as well as Antrim reacting with different chemical mixture.

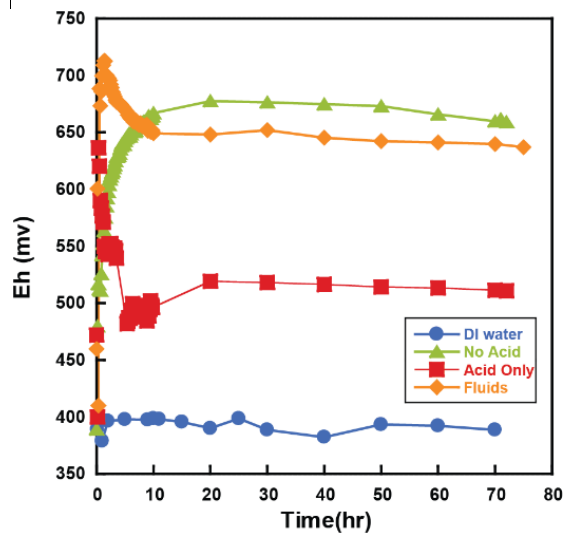


Figure A8-1: Eh profile for Utica-Collingwood mixtures experiments

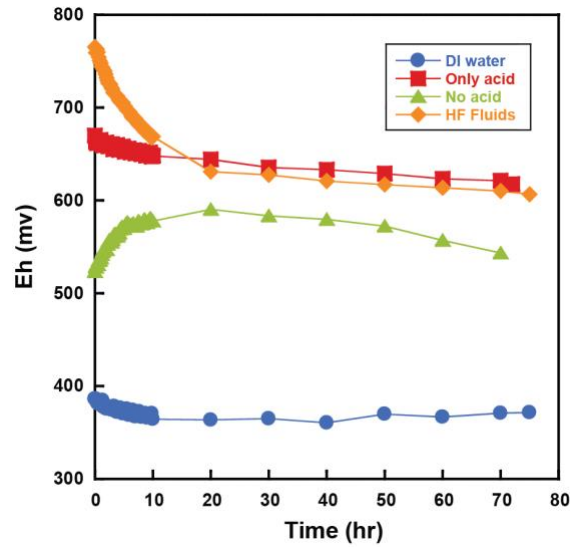


Figure A8-2: Eh profile for Antrim experiments

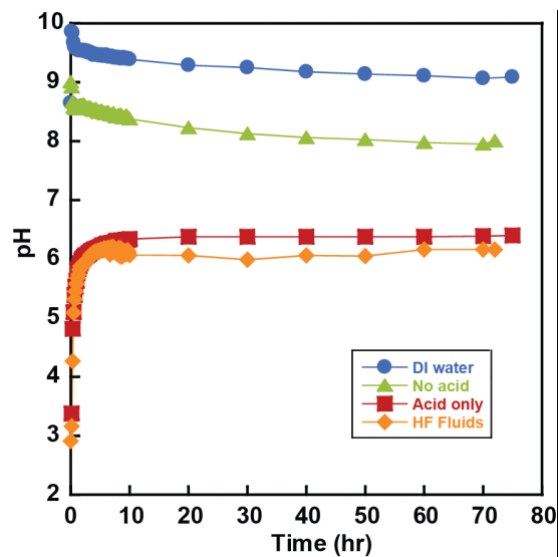


Figure A8-3: pH profile for Utica-Collingwood mixture experiments

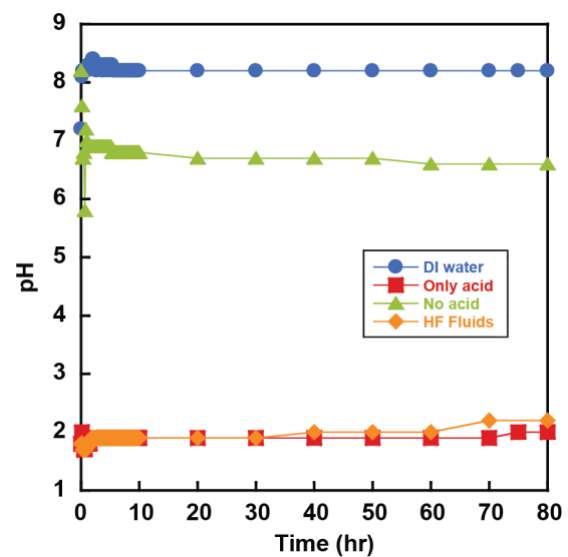


Figure A8-4: pH profile for Antrim experiments

A-9: Pyrite dissolution discussion

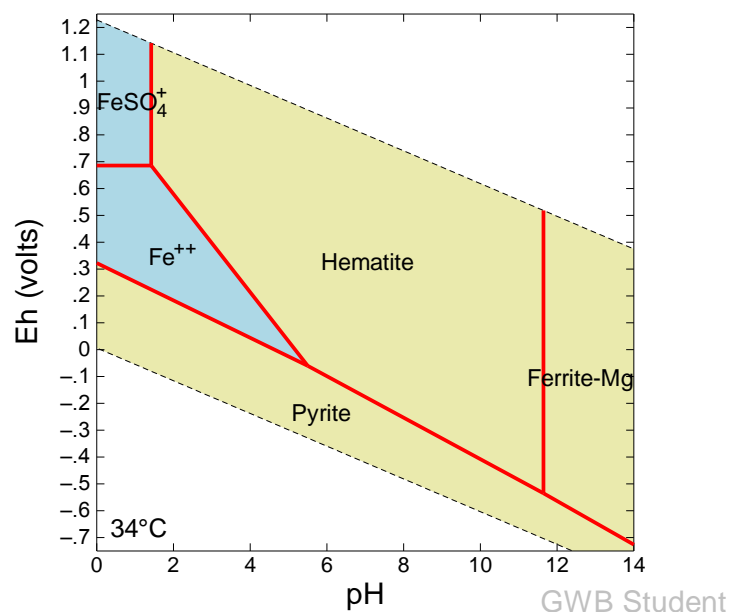
A9-1: Stability graph

Act2 in GWB student edition 11.0.3 has been adopted to construct Fe stability diagram for Antrim in contact with HF fluids under 1.0 km condition. The thermodynamic data named thermos is incorporate. Final concentrations of all major cations and anions shown in table A9-1 were put in to construct this eh-pH diagram (Figure A9-1). According to Figure A9-1, Fe^{2+} is the dominate species in batch system.

Table A9-1: Input water chemistry

	Concentration
Fe	0.001204 M
Na	0.000567 M
Mg	0.001032 M
K	0.0003158 M
Ca	0.001335 M
Sr	2.18036E-06 M
Ba	4.383E-07 M
Cl	0.040330905 M
SO ₄	0.002478536 M
pH	2.2
Eh (V)	0.62

Figure A9-1: Fe stability diagram for Antrim 1.0 km HF fluids



A9-2: Pyrite dissolution simulation

React in GWB student edition 11.0.3 has been applied to simulate pyrite dissolution.

The rate of mineral dissolution is described by a simple built-in rate law shown below:

$$r = A_s k_+ \prod (a_j | m_j)^{p_j} \left(1 - \frac{Q}{K} \right)$$

Where r is the mineral's dissolution rate (mol/s), A_s is the surface area of the mineral (cm^2), k_+ is the intrinsic rate constant (in $\text{mol}/(\text{cm}^2 \text{ s})$), Q and K are the activity product and equilibrium constant for the dissolution reaction, a_j , m_j = activity or concentration of promoting or inhibiting species, P_j = species' power (+ is promoting, - is inhibiting).

For the built-in law, specific surface area (cm^2/g) and rate constant ($\text{mol}/(\text{cm}^2\text{s})$) need to be put in as input for the simulation. The rate constants for all minerals are from previous investigation.⁶

i). Specific surface area analysis:

Pyrite grain's radius (R) is $\sim 0.5\text{-}5\mu\text{m}$ in Antrim samples (Figure A9-2). For this grain size, the specific surface (SSA) would range from $\sim 1200\text{-}12000 \text{ cm}^2/\text{g}$ according to equation below. $5000 \text{ cm}^2/\text{g}$ has been used as specific surface area.

$$SSA = \frac{Area}{Mass} = \frac{4\pi R^2}{\rho \times \frac{4\pi R^3}{3}} = \frac{3}{\rho R}$$

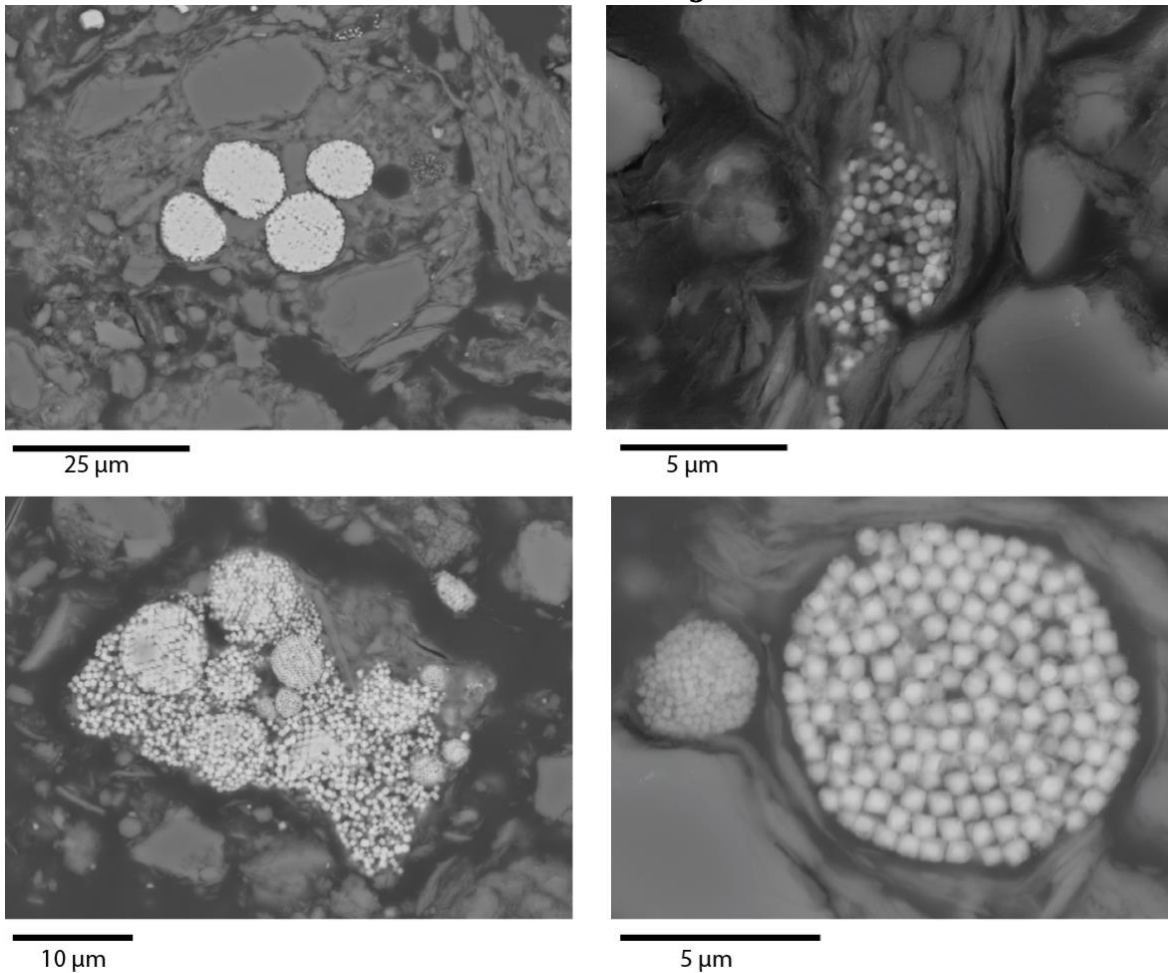


Figure A9-2: Scanning electron micrograph of Pyrite framboid in Antrim powder samples

ii). Simulation parameters:

Table A9-2 shows all parameters used in pyrite dissolution simulation.

Table A9-2: Simulation parameters

		SIMULATION
Fixed Eh (V)		0.6
Pyrite	surface area (cm ² /g)	5000
	Rate constant (mol/cm ² sec) ⁶	3.01995e-12
	Mass (% of 3 g shale)	2.8%
Ankerite	surface area (cm ² /g)	20000
	Rate constant (mol/cm ² sec) ⁶	6.45654E-08
	Mass (% of 3 g shale)	3% (by adding 0.5% MgFe(CO ₃) ₂ + 2.5% MgCO ₃)

iii). Simulation results:

[Fe²⁺] concentration profile in simulated as well as batch experiment is shown in Figure A9-3. The amount of pyrite dissolved is demonstrated in Figure A9-4. Carbonate minerals has been consumed within the first ~30 min (Figure A9-5). Fe speciation is illustrated in Figure A9-6. Fe²⁺ dominate the system and all other species are all below 0.0001 M.

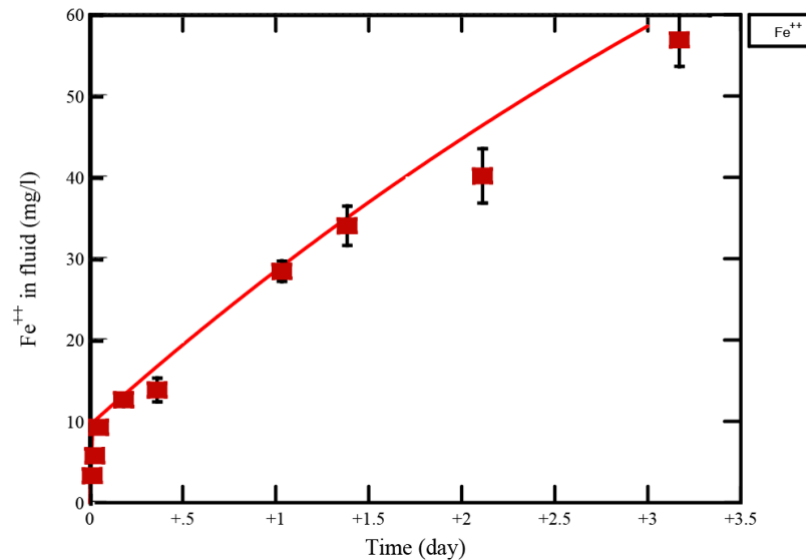


Figure A9-3: Comparison of [Fe²⁺] in batch experiment and simulation

Figure A9-4: Pyrite dissolution

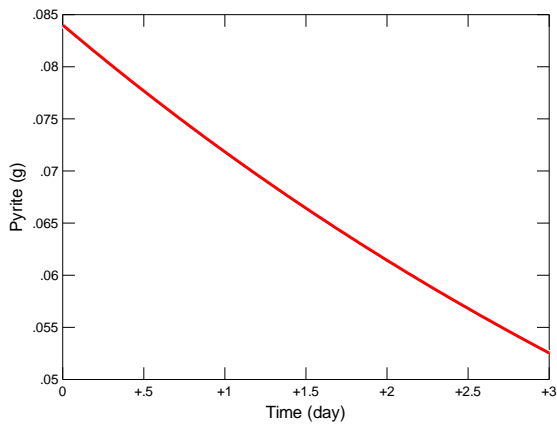


Figure A9-5: Carbonate dissolution

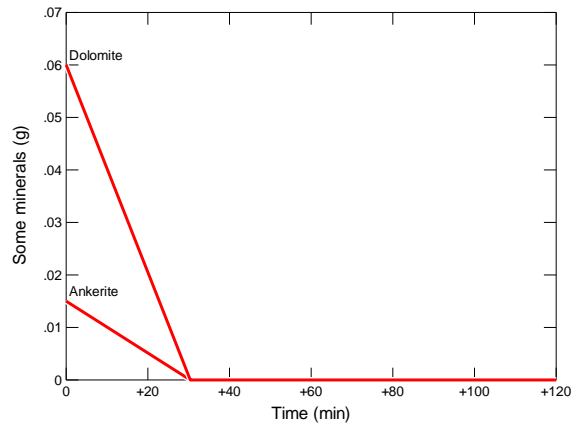
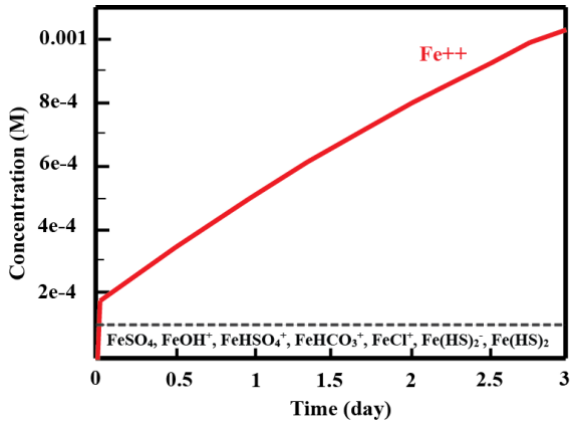


Figure A9-6: Fe speciation diagram



iv). Sensitivity analysis

Figure A9-7 and Figure A9-8 show simulated $[Fe^{2+}]$ at variable surface areas and initial pyrite amount. These figures demonstrate the sensitivity of two important parameters on the influence of pyrite dissolution.

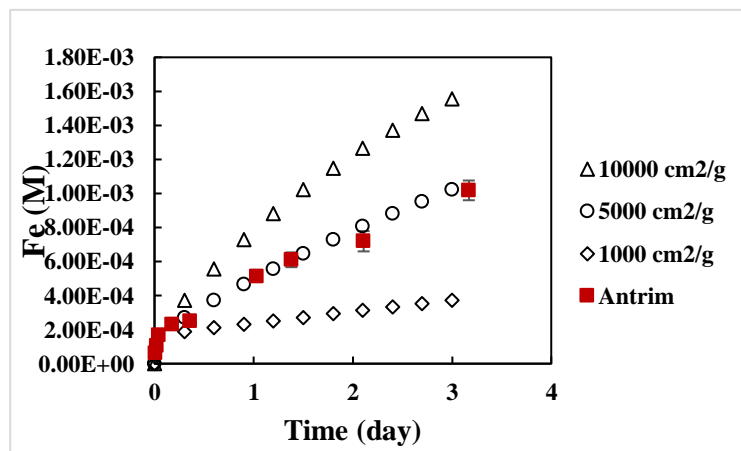


Figure A9-7: Simulated $[Fe^{2+}]$ under different surface areas.

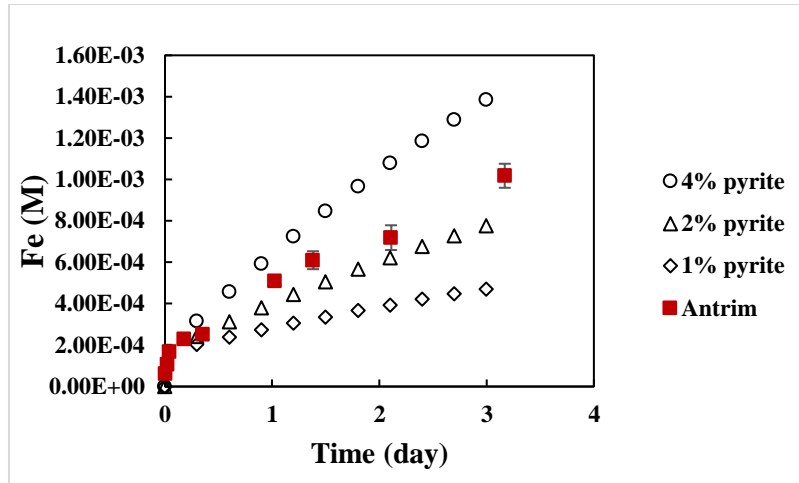


Figure A9-8: Simulated [Fe²⁺] under different initial pyrite amount

A-10: As vs. Fe correlation

Figure A10-1 show the correlation of [As] and [Fe] for Antrim shale reacting with only acid and HF fluids. This correlation proves that As is bounded to same minerals contain Fe like pyrite.

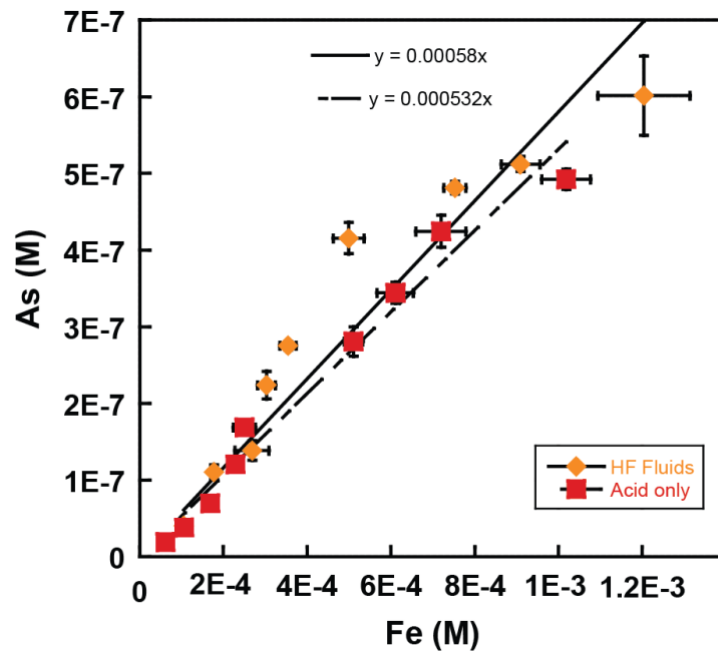


Figure A10-1: [As] vs. [Fe] for Antrim in contact with only acid (Acid only) and all four chemical additives (HF fluids)

A-11: Flowback water

The following table shows all major cations and anions measured in flowback water samples from a recently completed Utica-Collingwood well (State Beaver Creek 1-23 HD-1).

Table A11-1: Flowback water characterization

Time (day)	Na (mg/L)		Ca (mg/L)		Sr (mg/L)		Ba (mg/L)		Mg (mg/L)		Fe (mg/L)	
	Conc.	std	Conc.	std	Conc.	std	Conc.	std	Conc.	std	Conc.	std
0	33234	1322	65134	1887	3355	169	24	0.12	4476	153	756	24
0.94	31688	957	62807	1876	3556	71	22	0.50	4451	151	680	20
1.67	26149	1285	53028	1692	3159	154	20	0.27	3745	101	575	19
3.75	28443	1071	61675	3538	3810	110	23	2.47	4371	281	663	39
5.73	34640	1160	73982	1872	4499	152	29	0.29	5167	182	782	26
7.84	35110	938	73874	2200	4399	168	51	1.62	5146	169	785	23
12.74	38296	1811	80057	3583	4495	114	63	0.50	5532	292	867	42
18.82	37752	415	83348	2583	3818	23	76	1.52	5058	40	833	35
33.82	39843	598	83603	1003	3887	78	85	1.28	5179	165	836	31
47.71	39715	238	81605	979	4224	338	89	6.44	5626	483	816	30
70.68	41507	581	87943	264	4008	40	89	0.97	5387	87	879	39
Time (day)	Cl (mg/L)		Br (mg/L)		SO ₄ (mg/L)		Saturation Index for barite calculated from GWB	Ra-226 (pCi/L)		Ra-228 (pCi/L)		
	Conc.	std	Conc.	std	Conc.	std		Activity.	std	Activity.	std	
0	162389	37	3568	180	76	4	1.09	2207	99	2108	96	
0.94	155477	479	3022	114	94	7	1.12	1377	667	1503	71	
1.67	160975	129	3138	261	95	3	1.08	615	38	646	41	
3.75	155944	184	3146	209	78	1	1.04	816	45	1021	55	
5.73	171033	184	3640	105	47	11	1.00	1291	64	1358	68	
7.84	152087	105	3696	431	40	5	1.01	2331	105	2367	111	
12.74	202410	91	4822	452	37	6	1.29	2535	111	2284	108	
18.82	220592	1522	3152	1564				1761	84	1631	82	
33.82	219250	379	3416	280				1404	72	1203	57	
47.71	225935	864	3198	449				1294	67	1156	60	
70.68	230616	297	3764	391				1443	72	1203	59	

A-12: Ra estimation for batch experiment

According to previous digestion work, U and Th content in Collingwood and Utica is obtained and shown in Table A12-1. By using secular equilibrium theory, Ra-226 and Ra-228 content is estimated by applying equation (1) and (2). Then at 10g/L rock: HF fluid ratio and assume all Ra in rock entered water, the corresponding Ra activity end up in water is estimated (Table A12-1).

$$\frac{^{226}\text{Ra}}{^{238}\text{U}} \approx \frac{\lambda_{^{238}\text{U}}}{\lambda_{^{226}\text{Ra}}} = \frac{1.55125 \times 10^{-10} \text{ yr}^{-1}}{4.33 \times 10^{-4} \text{ yr}^{-1}}$$

$$\frac{^{228}\text{Ra}}{^{232}\text{Th}} \approx \frac{\lambda_{^{232}\text{Th}}}{\lambda_{^{228}\text{Ra}}} = \frac{4.948 \times 10^{-11} \text{ yr}^{-1}}{0.1203 \text{ yr}^{-1}}$$

$$[\text{Ra-226}] = 3.4\text{E-}7 * [\text{U-238}] \quad (1)$$

$$[\text{Ra-228}] = 4.04\text{E-}10 * [\text{Th-232}] \quad (2)$$

Table A12-1: Radium level estimation

		Collingwood	Utica	UC 1:1 mixture
U content (mg/kg)		3	3.5	
Th content (mg/kg)		4.6	10.5	
Ra-226 in rock (pCi/g)		1.02	1.19	
Ra-228 in rock (pCi/g)		0.57	1.3	
10 g/L rock: HF fluid ratio	Ra-226 (pCi/L)	10.2	11.9	11.05 (=0.011 ng/L)
	Ra-228 (pCi/L)	5.7	13	9.35 (=0.009 ng/L)

Reference:

- (1) What is Frac Sand? A Durable Sand for Hydraulic Fracturing
<http://geology.com/articles/frac-sand/>
- (2) Darrell Kirk Nordstrom; L. Niel Plummer; Donald Langmuir; Eurybiades Busenberg; Howard M. May; Blair F. Jones; David L. Parkhurst. Revised Chemical Equilibrium Data for Major Water?Mineral Reactions and Their Limitations. In *Chemical Modeling of Aqueous Systems II*; ACS Symposium Series; American Chemical Society, 1990; Vol. 416, pp 398–413.
- (3) Li, Y.-H.; Takahashi, T.; Broecker, W. S. Degree of saturation of CaCO₃ in the oceans. *J. Geophys. Res.* **1969**, 74 (23), 5507–5525.
- (4) Blount, C. W. Barite solubilities and thermodynamic quantities up to 300/sup 0/C and 1400 bars. *Am Miner. U. S.* **1977**, 62:9-10.
- (5) Hajnos, M. Buffer Capacity of Soils. In *Encyclopedia of Agrophysics*; Gliński, J., Horabik, J., Lipiec, J., Eds.; Encyclopedia of Earth Sciences Series; Springer Netherlands, 2014; pp 94–95.
- (6) Palandri, J. L.; Kharaka, Y. K. *A compilation of rate parameters of water-mineral interaction kinetics for application to geochemical modeling*; DTIC Document, 2004.

Appendix B
Supplemental data and figures for Chapter 3:

B-1: Sequential extraction results of Collingwood

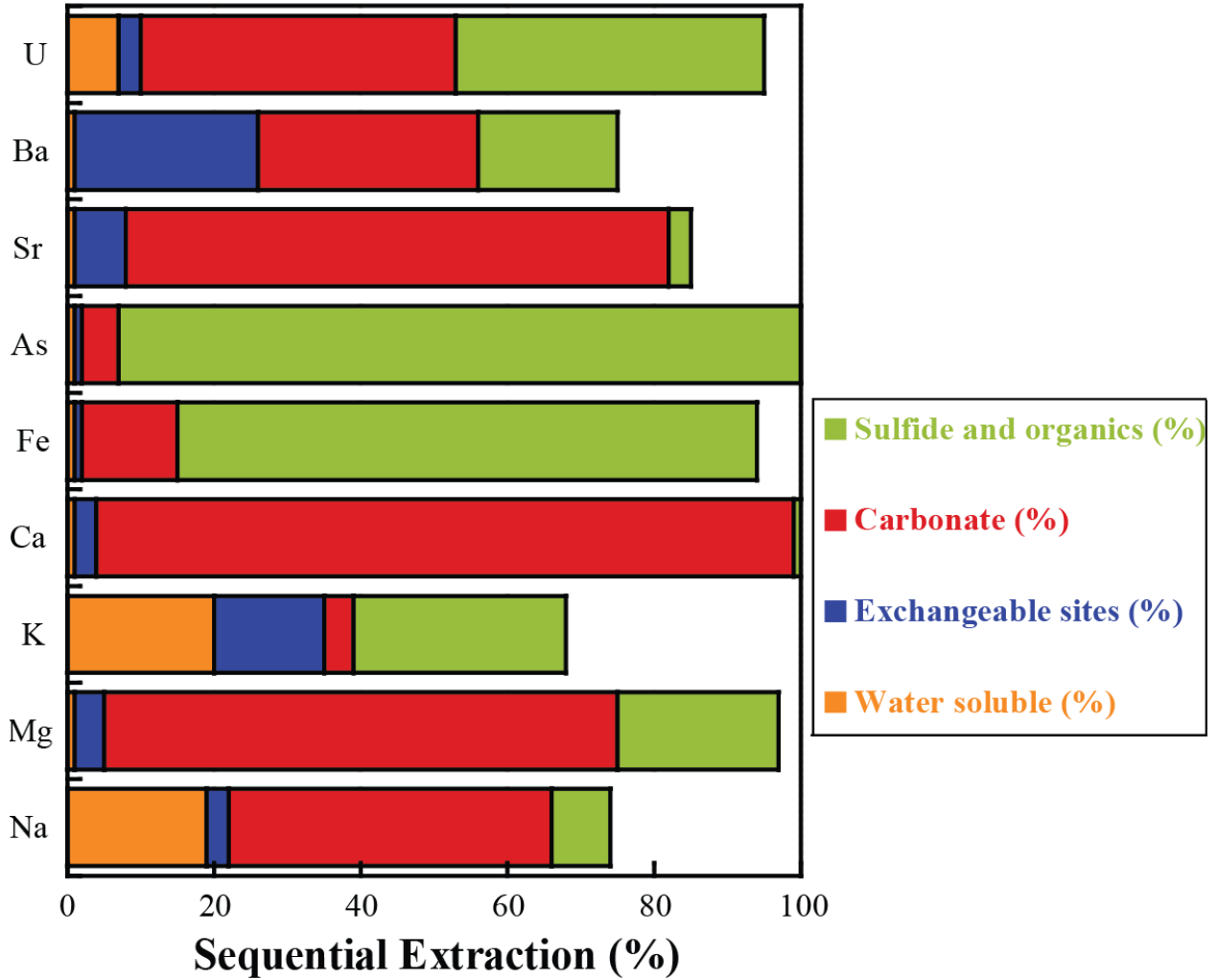


Figure B1: Sequential extraction results for proportioning of elements between exchangeable sites, water-soluble, carbonate and sulfide or organic phases for Collingwood.

B-2: Core characterization

(i). Element mapping to obtain mineral area fraction

Based on EDS results from three points in region (a) and two points in region (b), the average mineral fraction can be calculated and shown in Figure B2. There are two distinct regions shown in X-CT scan: region a) with darker grey color and region b) with lighter color. According to the quantitative results from element mapping and assume Sulphur represents pyrite, Calcium represents calcite, Aluminum represents clay; the mineral fraction can be calculated. Averaged results shown in Figure B2.

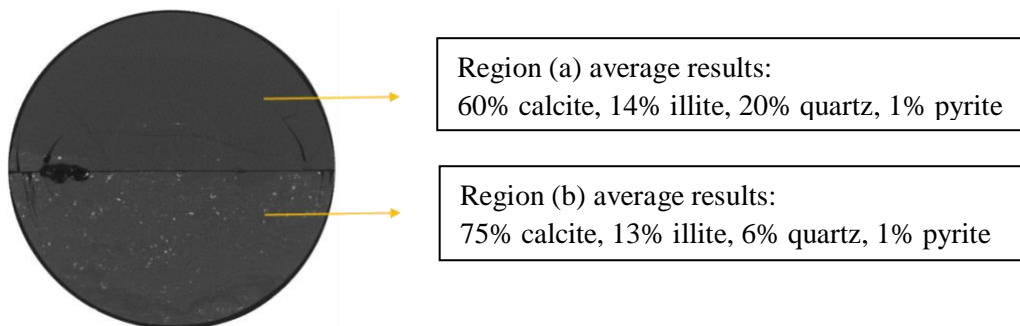


Figure B2: Averaged mineral fraction results.

(ii). Core section images together with EDS data

Shale heterogeneity demonstrates by image of the core intersection (1) shown in Figure B3. This figure shows the location of big pyrite grains. In addition, SEM images of the fracture in core section (1) as well as EDS results are demonstrated in Figure B4. In this figure, pyrite is embedded in calcite and clay matrix. Also, the clay matrix seems to surround the calcite and might inhibit calcite dissolution. Figure B5 demonstrates similar findings for core section (2), which is more close to inlet. More dissolved region area is expected.

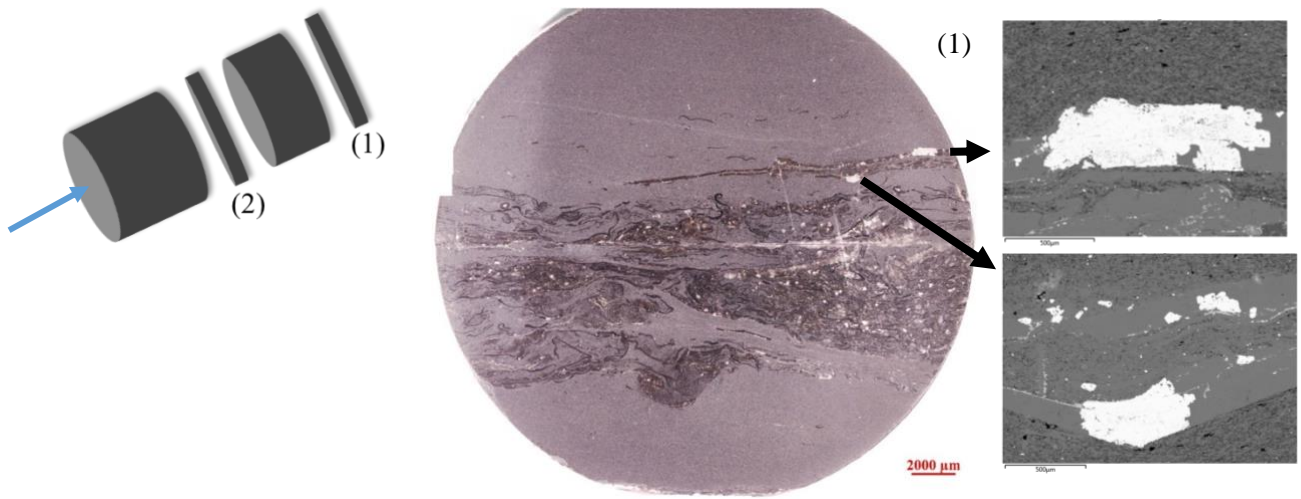


Figure B3: Core intersection (1) images and close-up of pyrite grains.

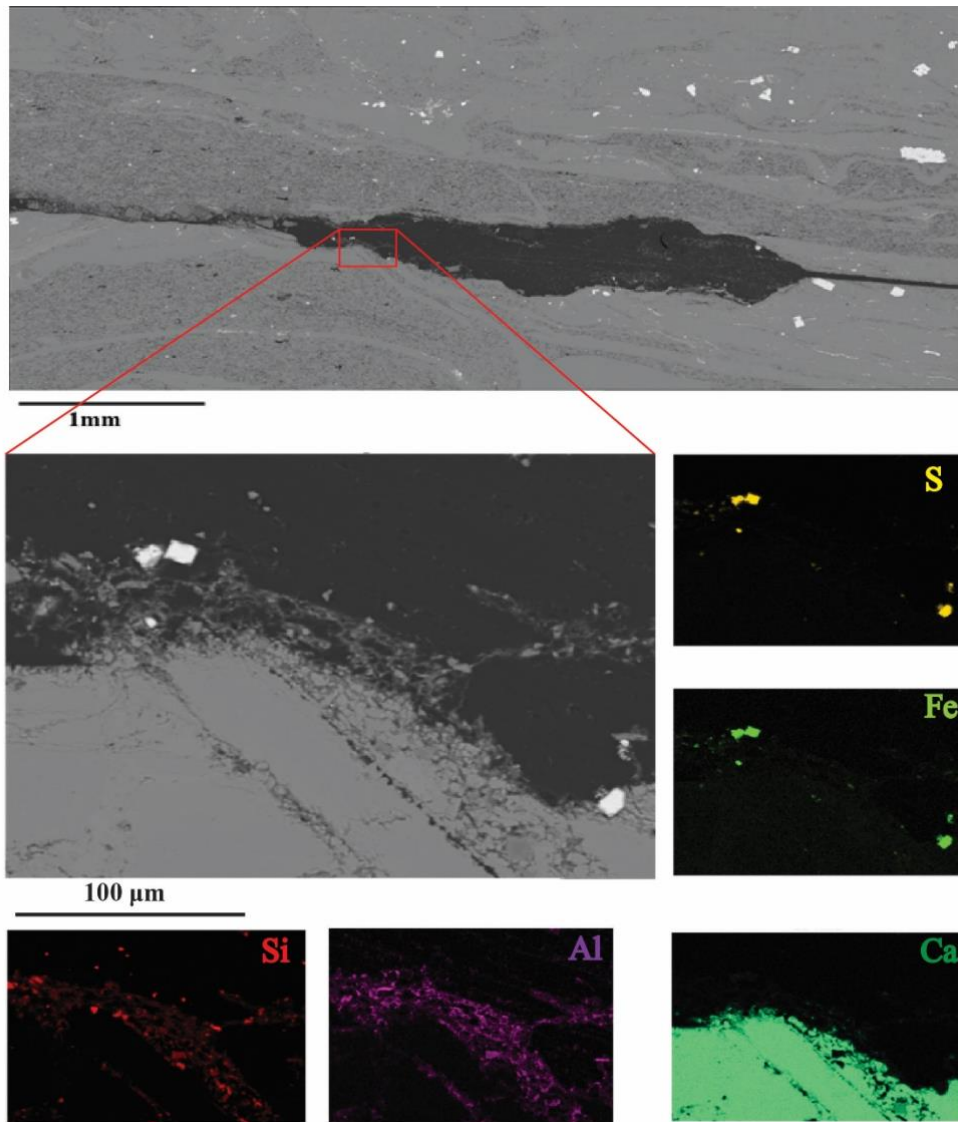


Figure B4: SEM images and EDS results in core fracture section (1).

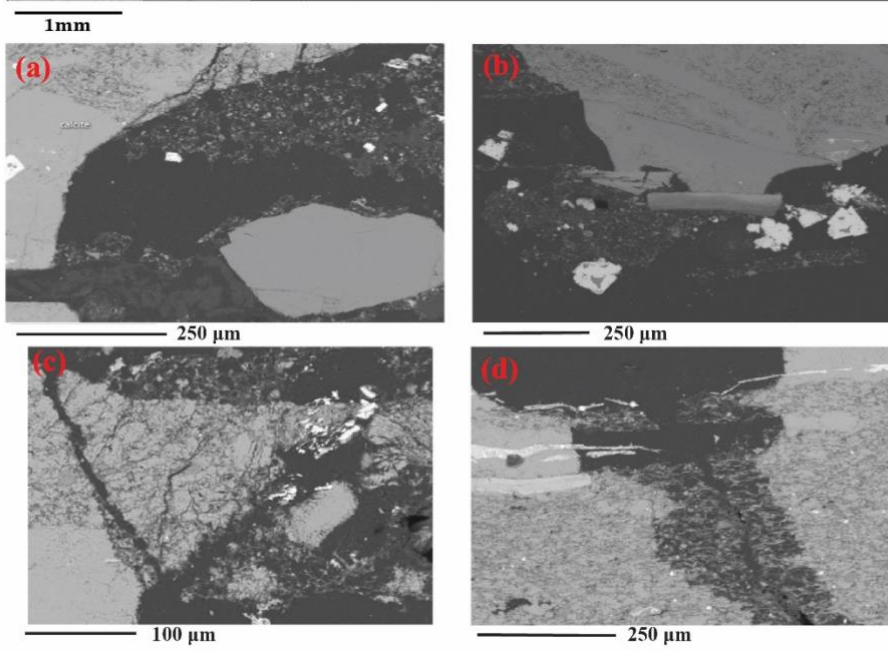
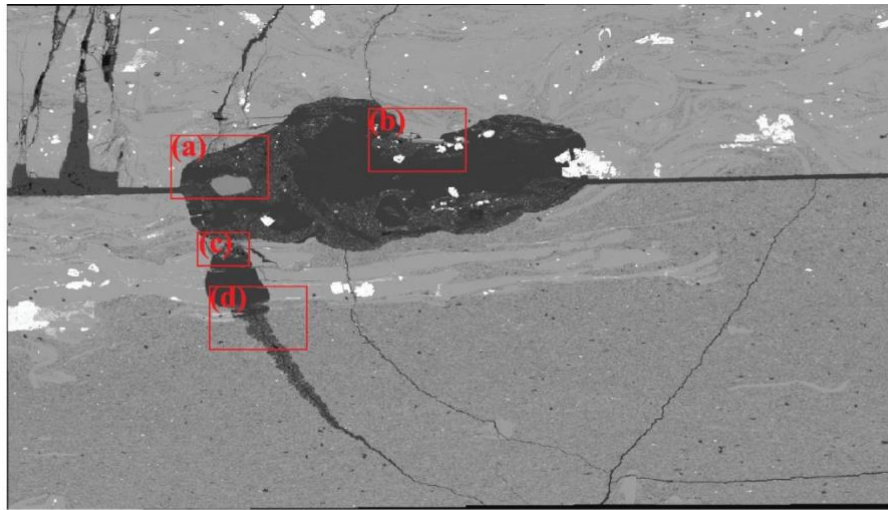


Figure B5: SEM images of core section (2).

(iii) Altered layer (L) formation

The altered layer formation have been observed in both in SEM images (Figure B4 B5) and post reaction XCT images in Figure B6.

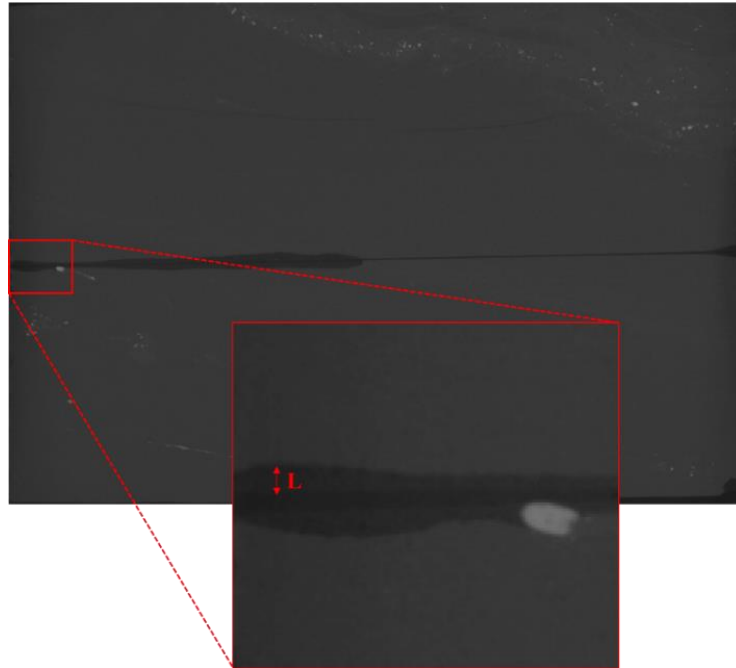


Figure B6: Formation of the altered layer (L).

B-3: Effluent pH, Ca, Fe, and As concentration profile for CW#1

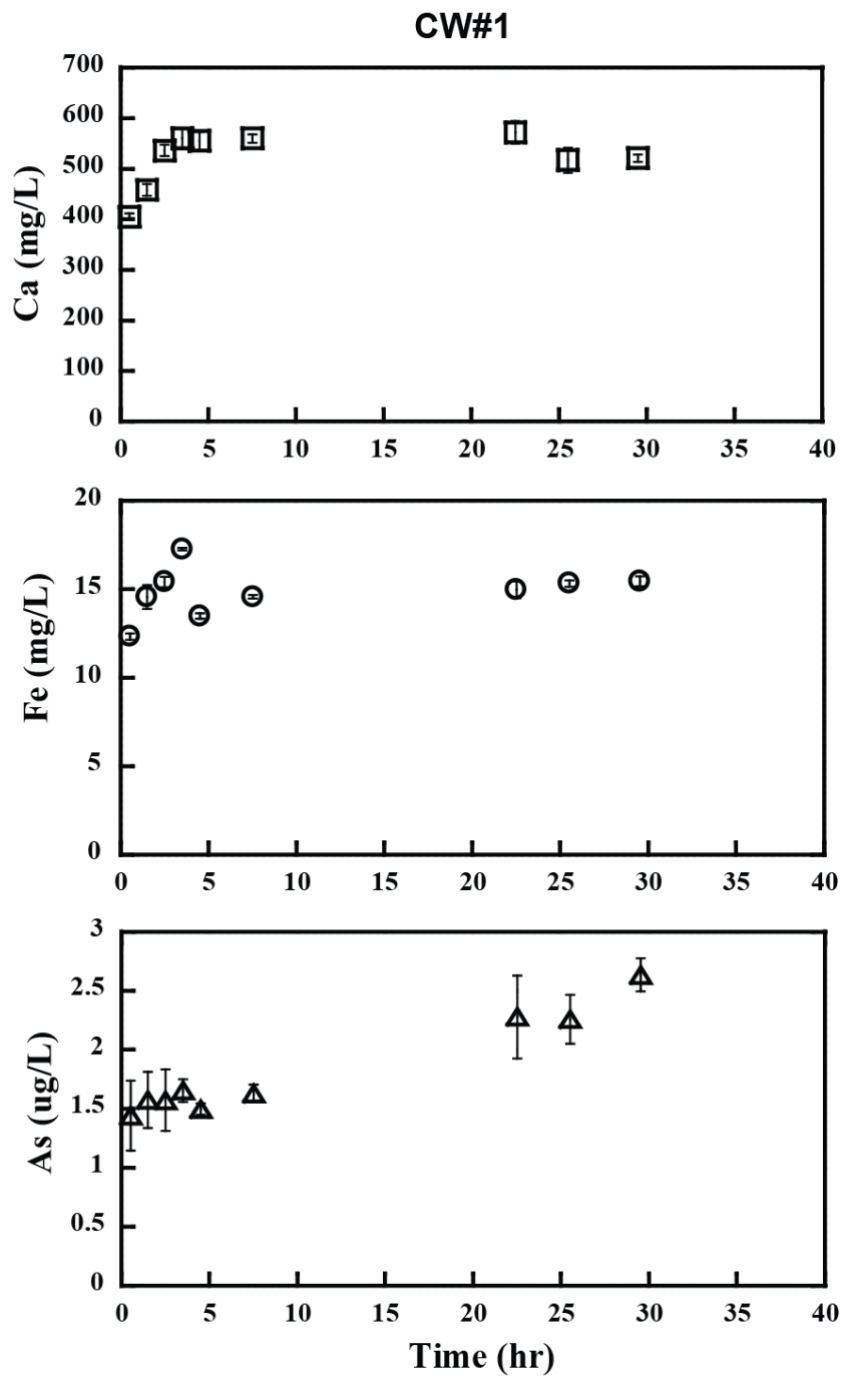
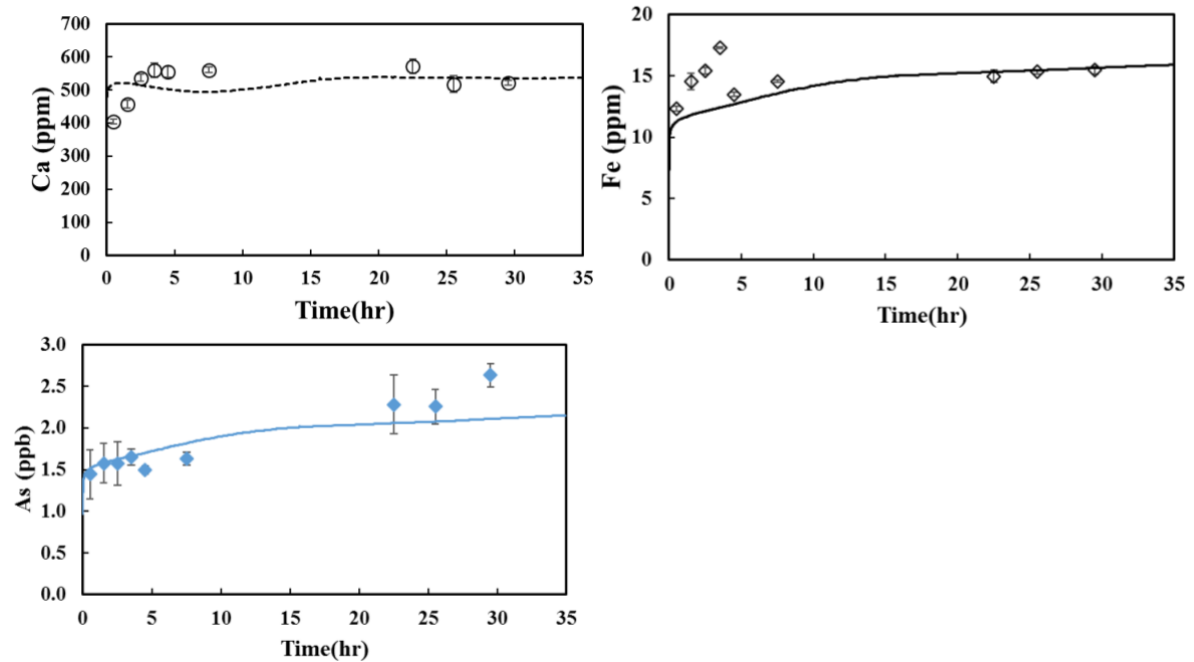


Figure B7: CW#1 experimental results.

B-4: Model calibration results

(a). CW#1



(b). CW#2

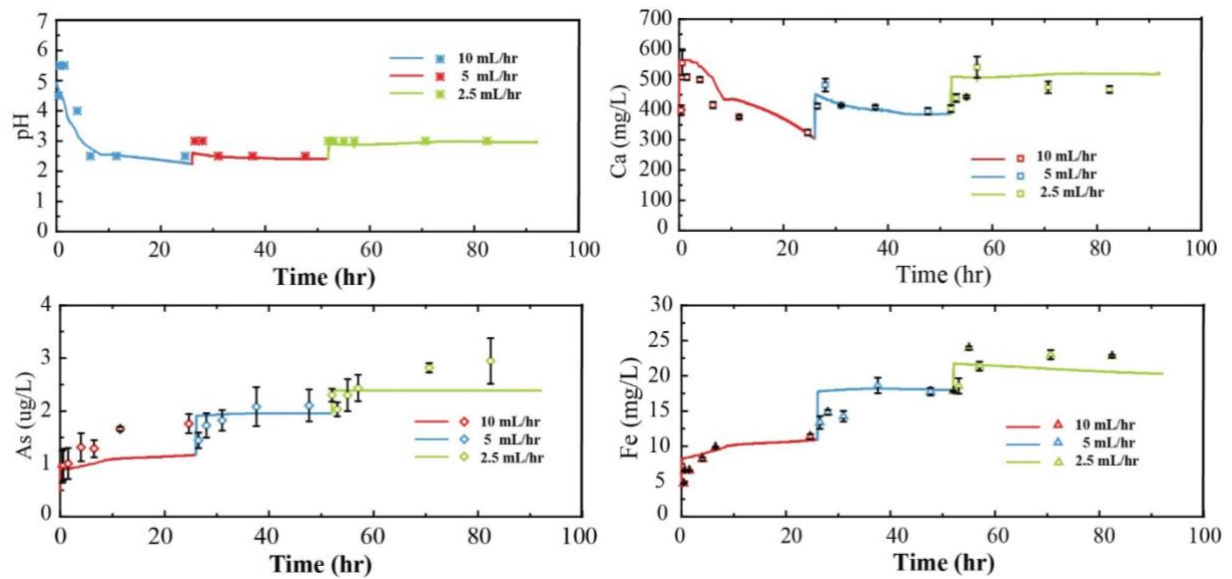
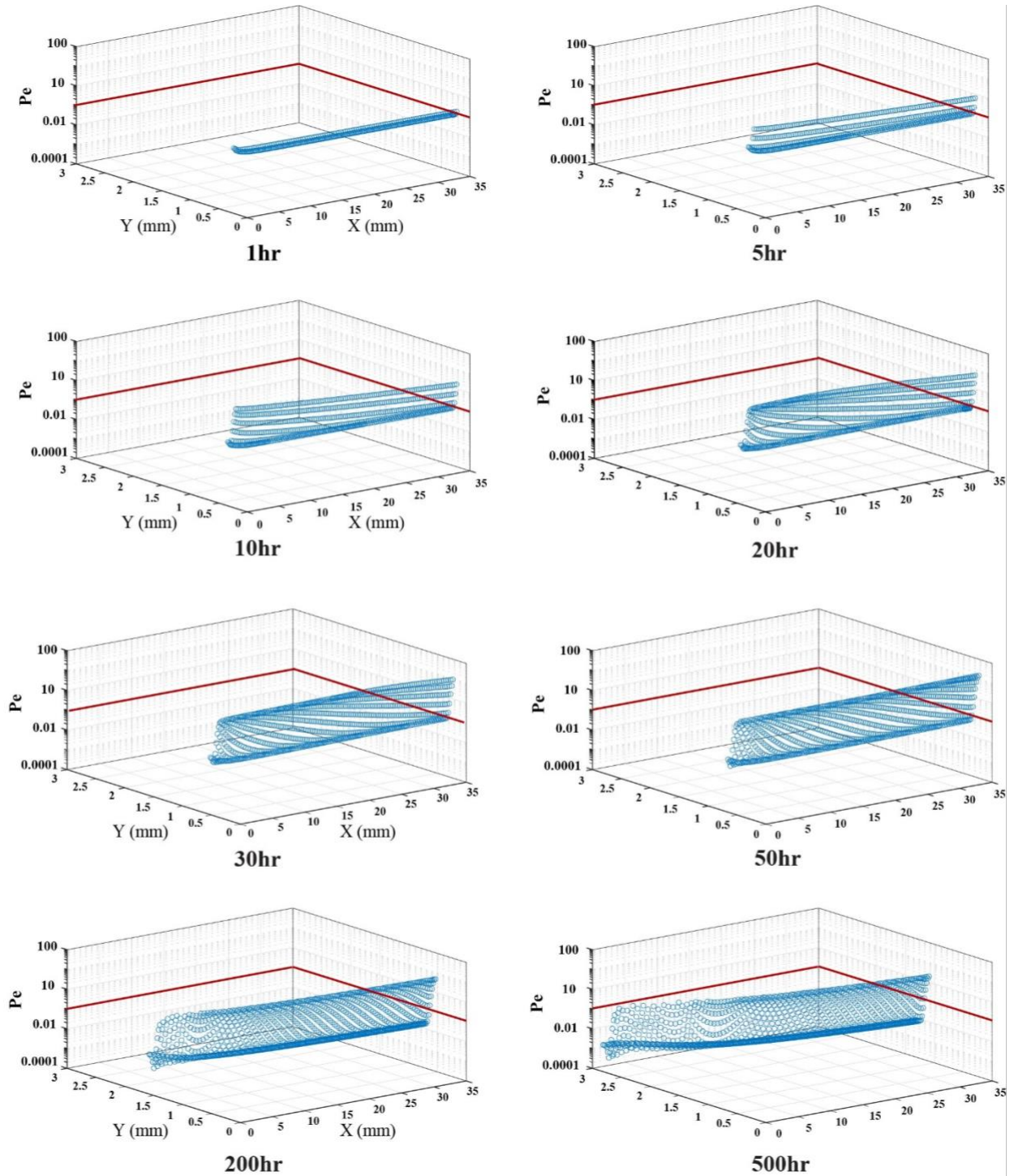


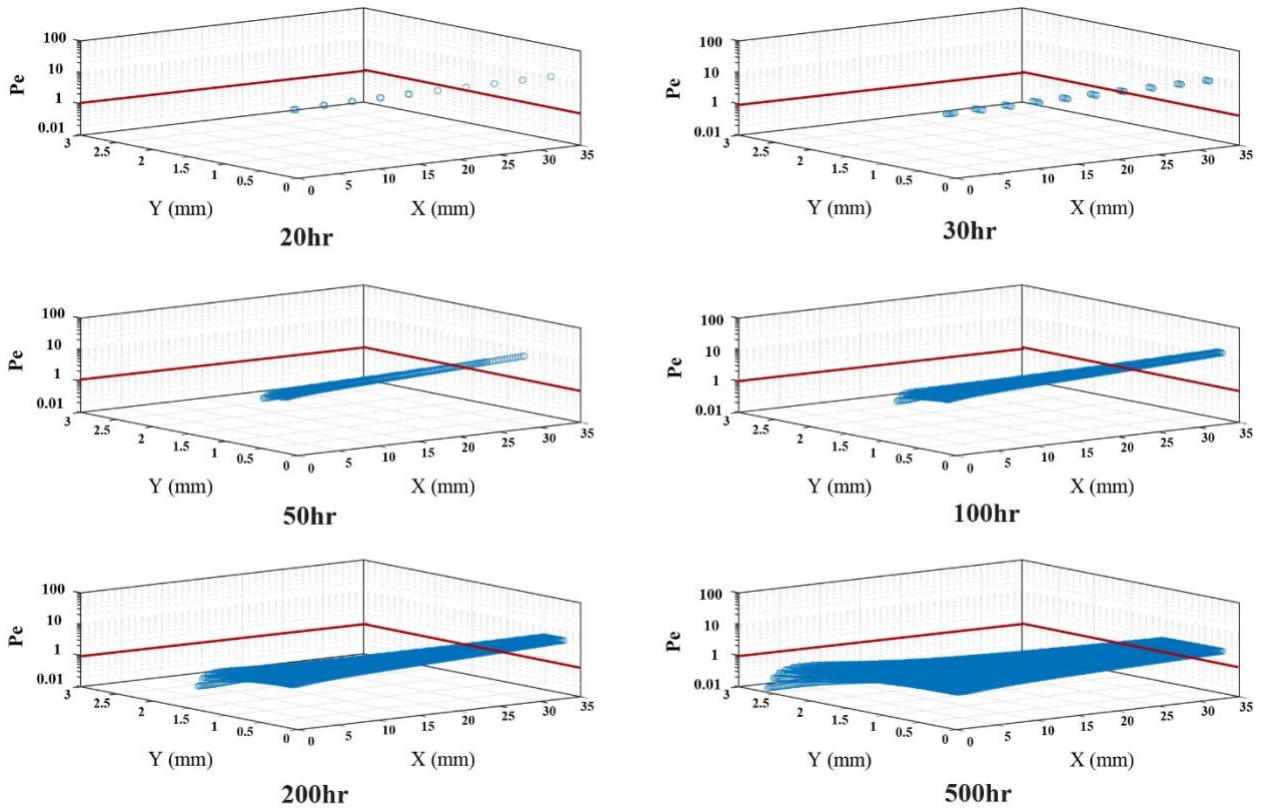
Figure B8: Effluent pH, calcium, iron and arsenic concentration as a function of time for the two flow-through experiments together with the modelling results. Black points are experimental results from CW#1 at 2.5 ml/hr. Blue, orange, and green dot represents experimental data from CW#2 at 10 ml/hr, 5 ml/hr, and 2.5 ml/hr, respectively.

B-5: Pe number

The trend of Pe number increase first and then decrease with time in layer i . While, Pe number overall keep decreasing with time in layer ii .



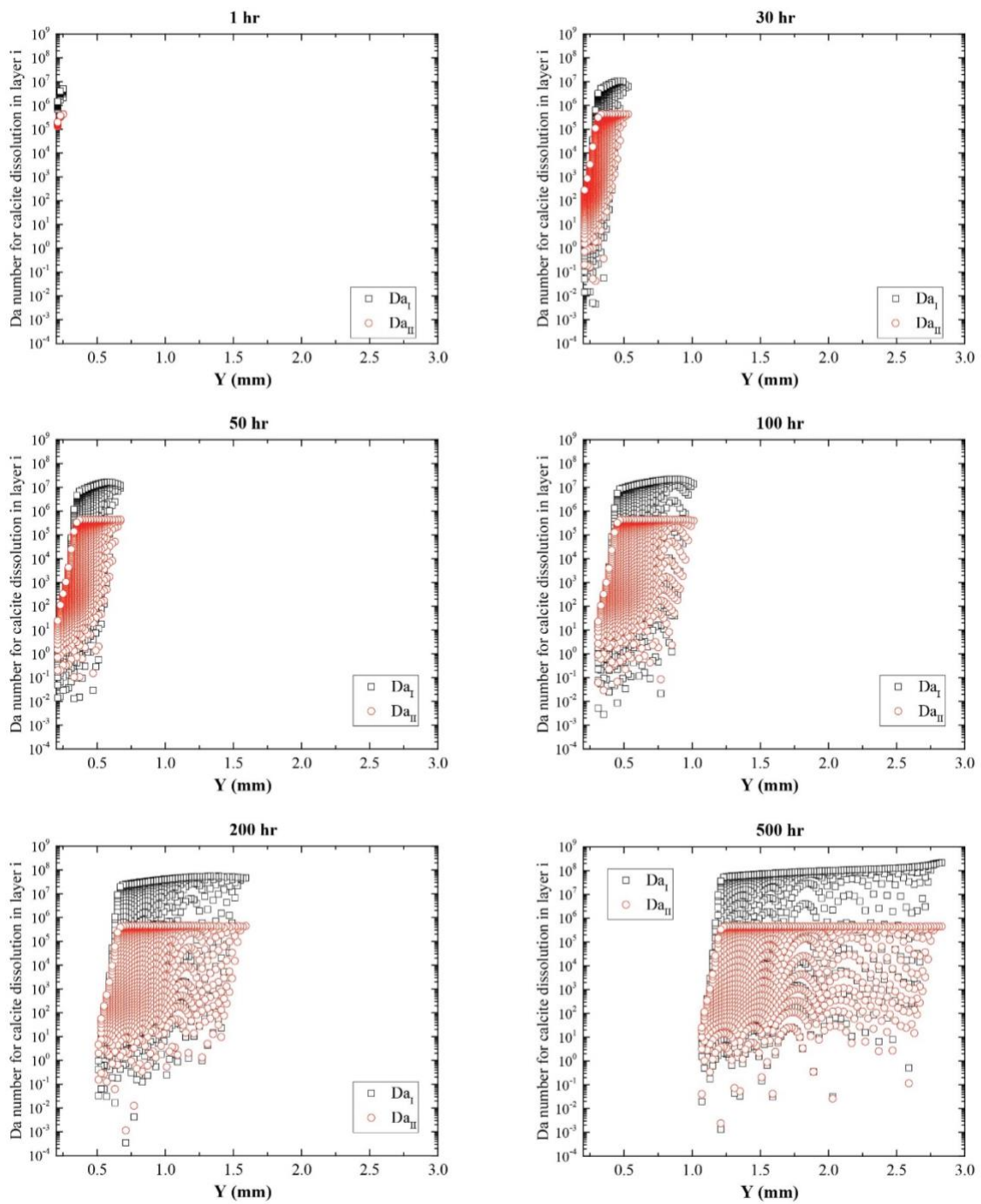
(a). Pe in layer i



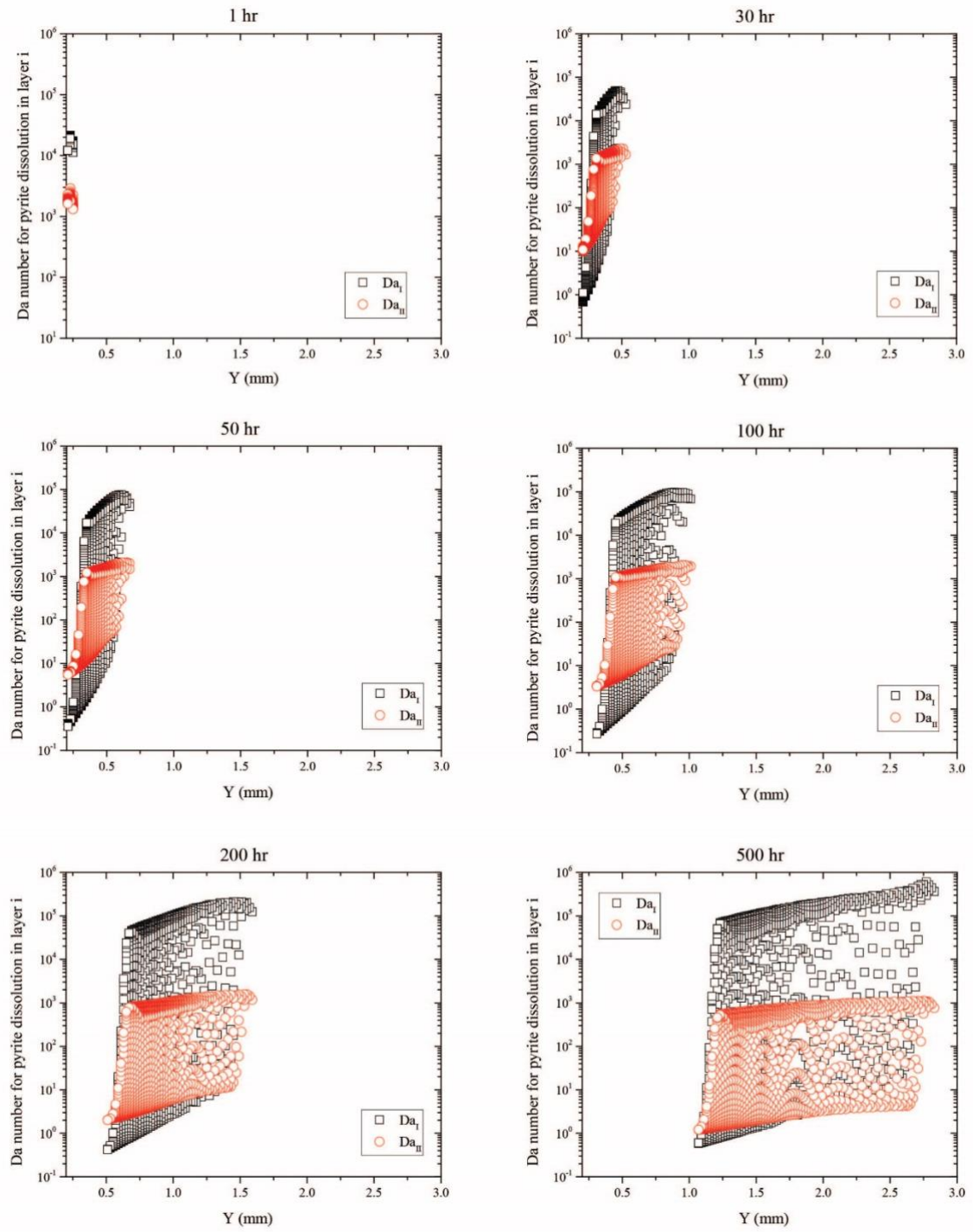
(b). Pe in layer *ii*

Figure B9: Pe number for individual grid.

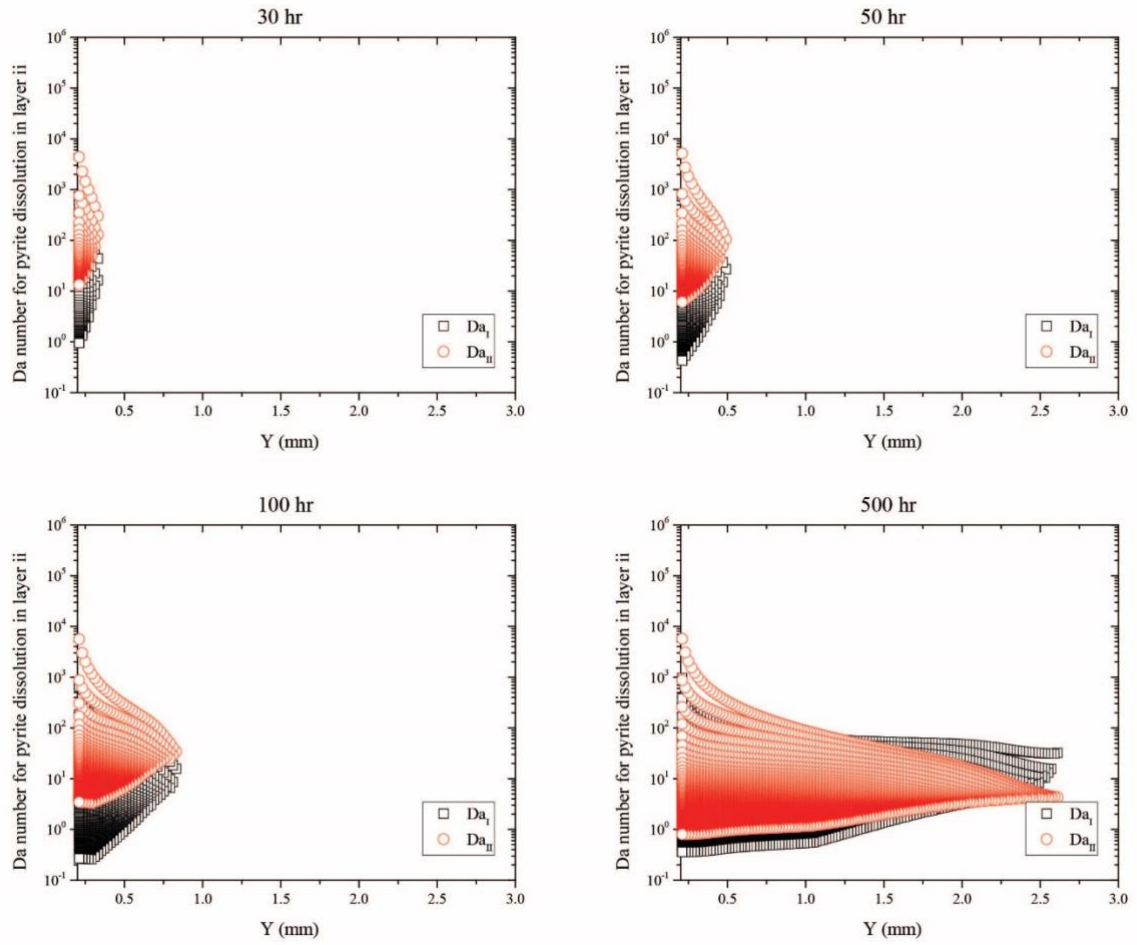
B-6: Da number



(a). Da numbers for calcite dissolution in layer i



(b). Da numbers for pyrite dissolution in layer i

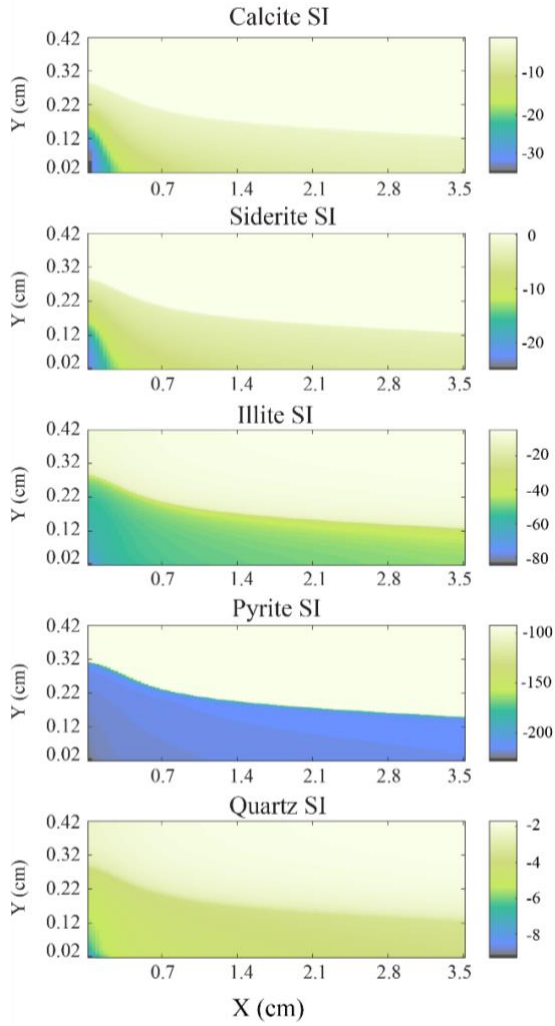


(c). Da numbers for pyrite dissolution in layer *ii*

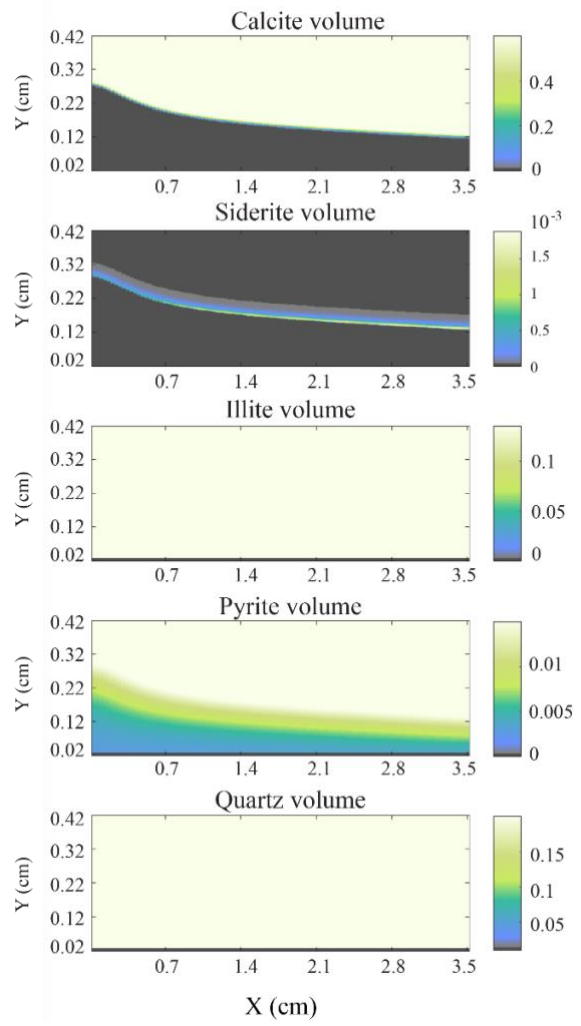
Figure B10: Da number for individual grid.

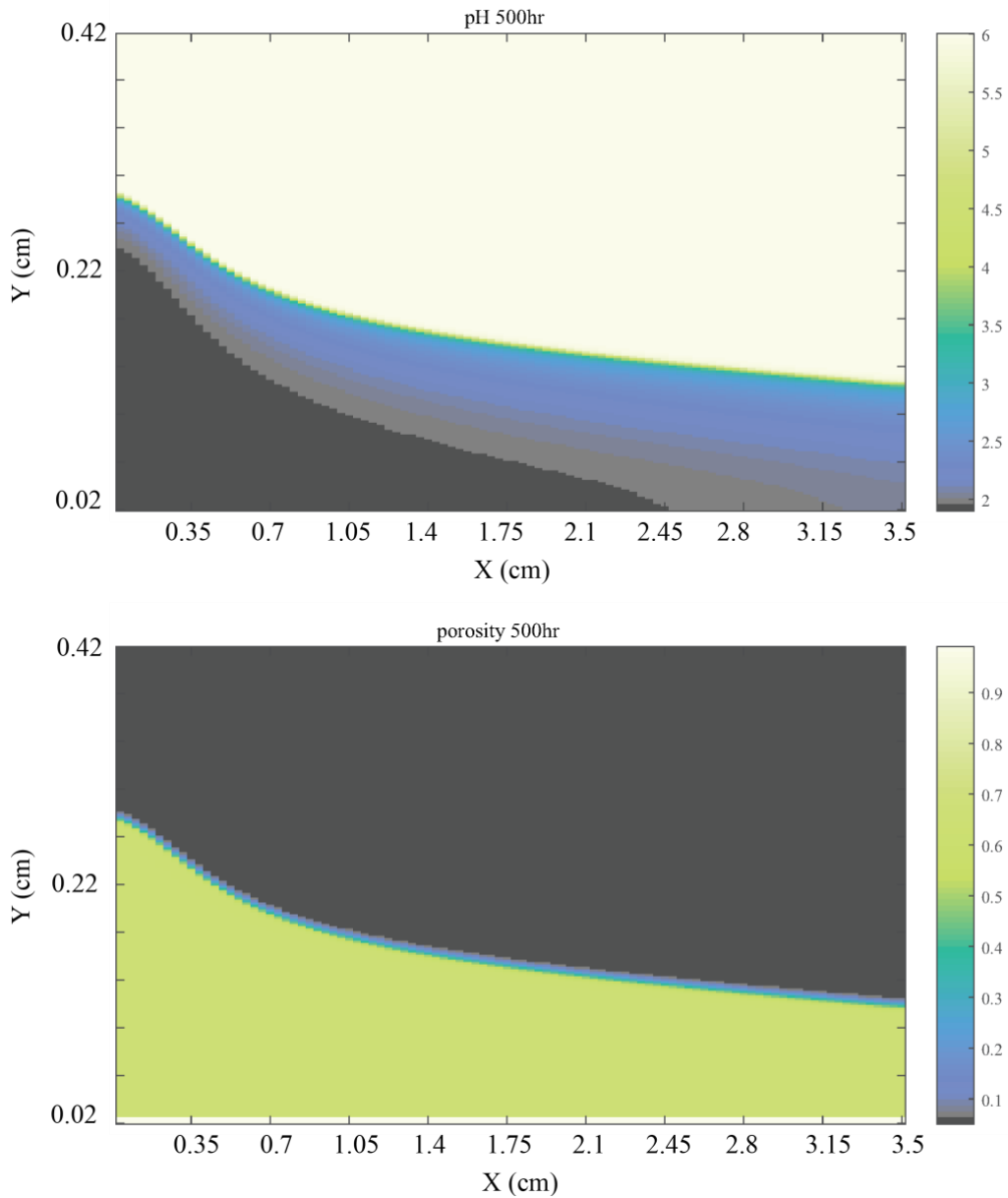
B-7: Model results under a flowrate of 10 ml/hr at 500 hr

(a). Saturation Index for different minerals



(b). Mineral Volumes





(c). pH and porosity

Figure B11: Model results (mineral saturation index, mineral volume, pH, and porosity) at 500 hr.

B-8: Model results for different calcite content

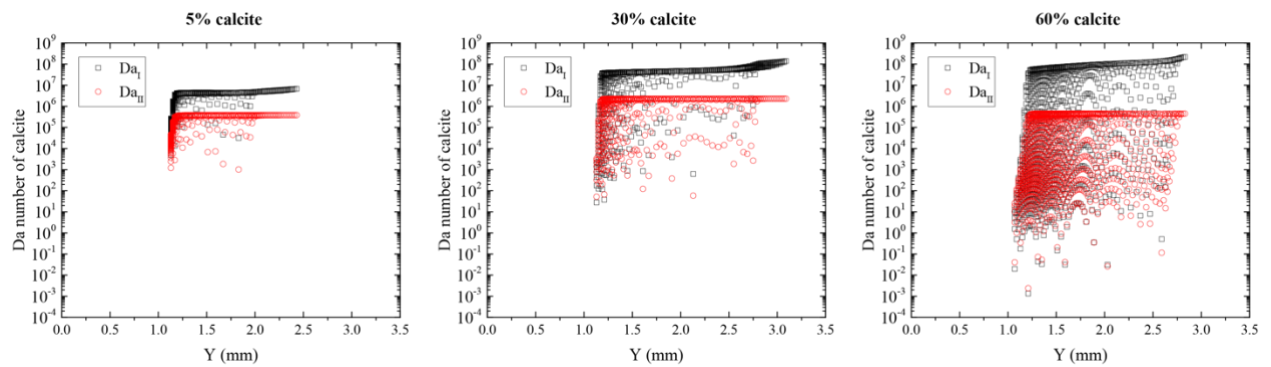


Figure B12: Model Damköhler numbers for calcite dissolution at variable calcite content (5%, 30%, 60%) in altered layer i at 500 hr simulation time.

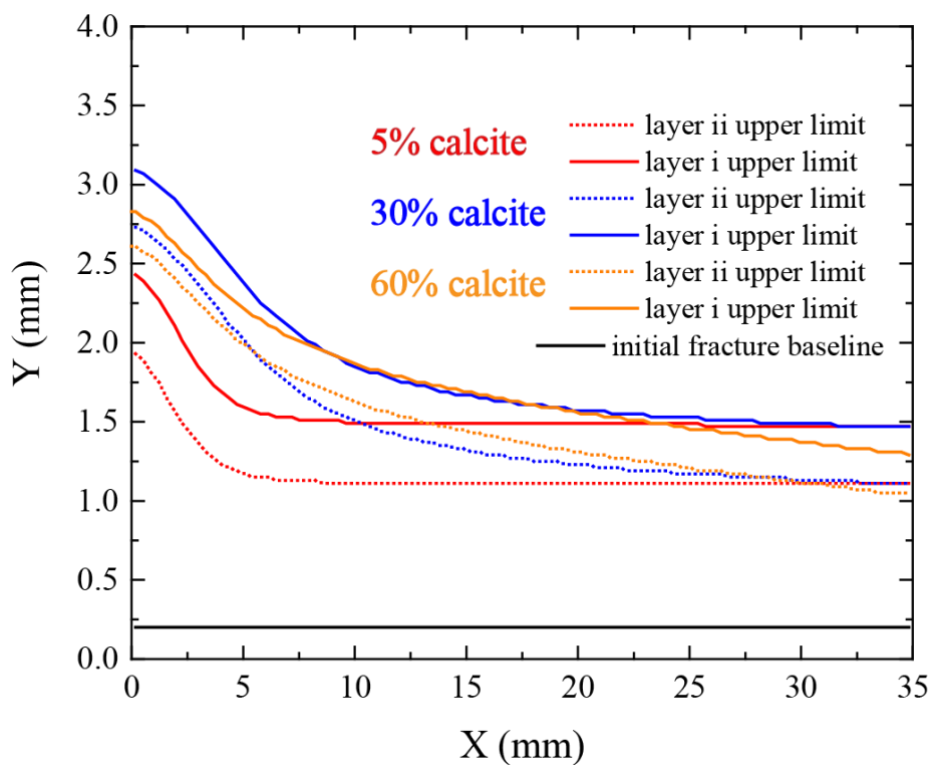


Figure B13: Model results of altered layer i and ii penetration depth into the core.

B-9: Model results for different pyrite content

Table B1: Averaged D_a for pyrite in layer \bar{u}

	Average D_{aI} for pyrite in layer \bar{u}	Average D_{aII} for pyrite in layer \bar{u}
1% pyrite	6.836	10.459
2% pyrite	6.595	9.987
3% pyrite	6.506	9.775

B-10: Heterogeneity and fractures

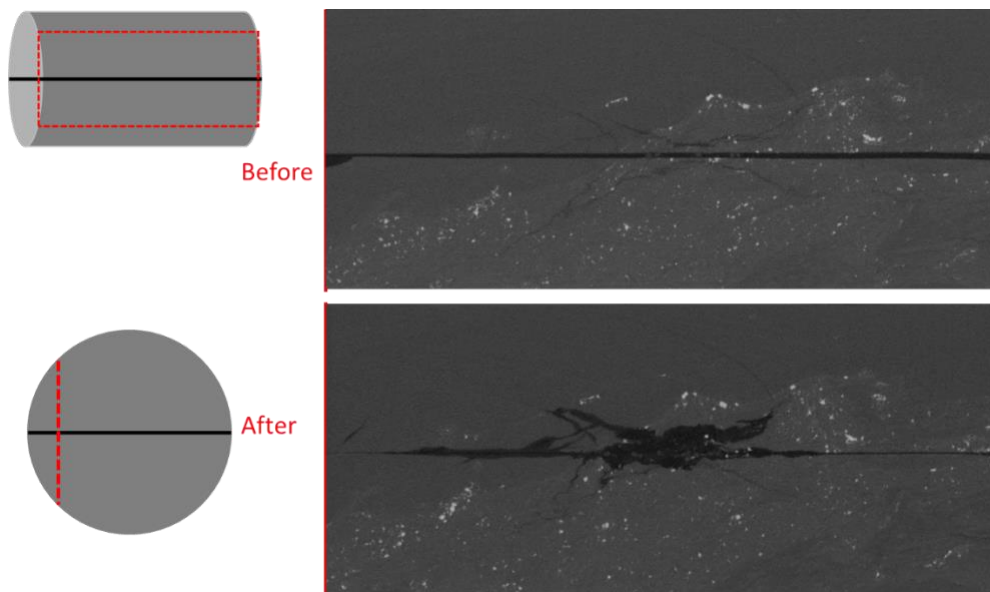


Figure B14: Reconstruction of the XCT scan before and after experiment CW#1.

Appendix C

Supplemental data and figures for Chapter 4:

C-1: Well logging introduction and rock/ water ratio estimation

Well logging is widely used to characterize subsurface formations to identify and evaluate potential of hydrocarbon bearing formations. So it can be utilized here as an effective way to obtain U and Th content. Normally the natural gamma radiation emitted by U and Th in formation rocks is used as an indicator of the presence of hydrocarbons by using geochemical logs, spectral gamma ray logs, neutron and resistivity logs.¹ The well logs are very important for oil and gas developer because it reflects shale characterization and provide well-to-well correlation. Gamma radiation, which is the only one of three identified nuclear radiation, can be used in well logging because it alone has sufficient penetrating power to go through the formation and the steel casing. Natural radiation is due to the disintegration of radioactive nuclei contained in the formation, which include K-40, U-238, and Th-232. The energy associated with each radiation is 1.46 MeV for K, 0.68 MeV for Th, and 1.12 and 0.98 MeV for U.² Radiation counts are directly proportional to the volume of material in the measurement area of the scintillation counters. Gamma ray logs are scaled in American Petroleum Institute (API) units. The gamma-ray API (GAPI) unit is defined as 1/200 of the difference between the count rate recorded by a logging tool in the middle of the radioactive bed and that recorded in the middle of the nonradioactive bed.³ Limestones have readings of 15–20 GAPI while shales vary from 75 to 150 GAPI, with maximum readings of about 300 GAPI for very radioactive shales.⁴ Unlike the conventional gamma-ray logs, spectral gamma-ray logs record the individual response to the different radioactive minerals and distinguished by the wavelengths of their characteristic gamma emissions. Thus the presence of K, U, and Th can be quantitatively evaluated. U and Th concentration in the formation is then obtained according to spectral gamma-ray well logs. Porosity as well as resistivity, density, water saturation can

also be acquired from well logging information. The equation C1 is applied to calculate rock: water ratio between formation water and shale reservoir. By applying this equation to the three formations in this study, the rock: water ratio was calculated and shown in Table C1. Collingwood -Utica data was obtained from well logs of State Beaver Creek 1-23 HD-1. Antrim data was acquired by combination of digestion and well logs; for the Marcellus formation, average data from literature was adopted for rock: water estimation.

$$\frac{rock(g)}{water(L)} = \frac{m_{rock}}{V_{water}} = \frac{\rho_{rock} \cdot V_{rock}}{V_{water}} = \rho_{rock} \left[\frac{1}{\Phi \cdot S_w} - 1 \right] \quad (C1)$$

S_w is water saturation. Φ is the bulk porosity of the rock and ρ_{rock} is the rock bulk density.

Table C1: Estimation of rock: water ratio for three formations

	Collingwood-Utica*	Antrim ^{&}	Marcellus
U (ppm)	3.2	19.8	26 ⁵
Th (ppm)	9.8	7.4	
Porosity (%)	5	20	6 ⁶
Water saturation (%)	34	15	25 ⁶
Ra228/226 (activity ratio)	0.84	0.10	
Original rock/water ratio (g/L)	150,000	87,623	177,957

*from well logs of State Beaver Creek 1-23 HD-1. [&] from digestion and well log data.

The predicted Ra-226 activity for U content range from 0 to 30 ppm at various rock/water ratio (10,000-200,000 g/L) as well as field samples is shown in Figure C1. In this figure, the reasonable range cannot account for the wide Ra-226 range of same formation.

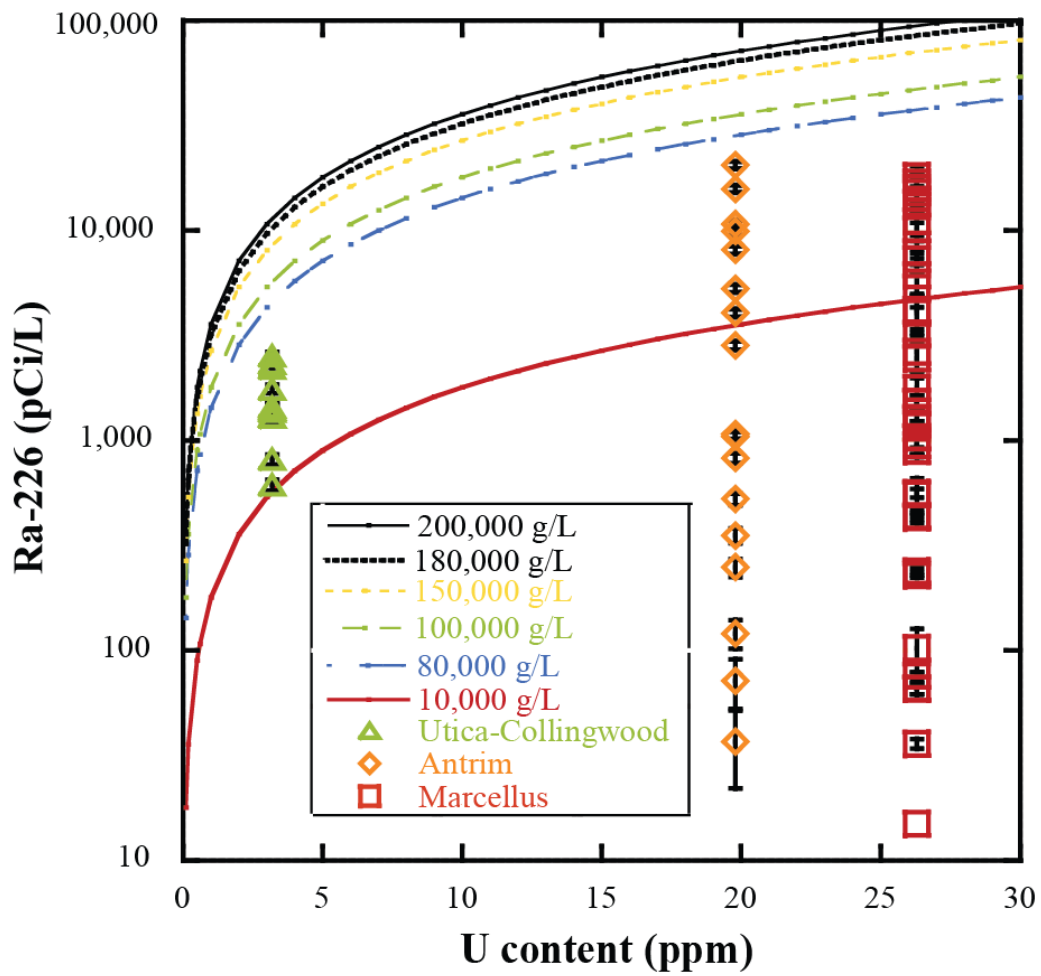


Figure C1: Predicted Ra-226 activity vs. U content from different rock/water ratio and field sample data from three formations.

C-2: Comparison of spectral gamma-ray well logs and digestion data for U and Th content

Spectral gamma-ray well logs data were used to obtain U and Th content in different depth within a well State Chester 18 (permit# 33875) targeting Antrim formation. Also, two samples during Antrim interval (458 m, 475 m) with higher U content as well as two sample not in Antrim interval (503 m, 506 m) in this well were chosen for whole digestion. Then data were gathered to compare to actual U and Th content obtained by whole digestion and also errors are shown in Table C2.

Table C2: Errors of Uranium and Thorium content from Antrim formation

Well depth (m)	U content			Th content		
	Actual (ppm)	well logs (ppm)	Error (%)	Actual (ppm)	well logs (ppm)	Error (%)
458	36.6	26	29	8.7	7.5	14
475	14.3	18	26	10.9	10	8
503	2.9	2.5	18	9.4	9	4
506	3.1	3	3	10.3	8	22

C-3: Ra measurements

Rapid ICP-MS method to measure Ra-226 is established by adding 100g/L Cl⁻ to all Ra-226 standard to match high salinity sample matrix. The average calibration curve with Ra (0.1 – 20 ppt) with the addition of 100g/L Cl⁻ is shown in Figure C2. The detection limit is 1.25 ppt (1250 pCi/L). Figure C3 presents Ra-226 as well as total Ra (Ra-228 and Ra-226) for 11 Collingwood flowback water samples from the State Beaver Creek 1-23 HD-1. This figure indicates that Ra reaches steady state after ~20 days, and also that Ra-226 has same trend with Ra-228.

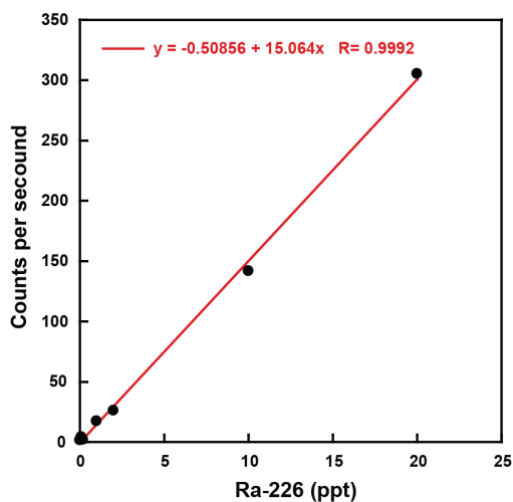


Figure C2: Average calibration curve with Ra (0.1 – 20 ppt) under 100g/L Cl⁻. The detection limit is 1.25 ppt which is 1250 pCi/L.

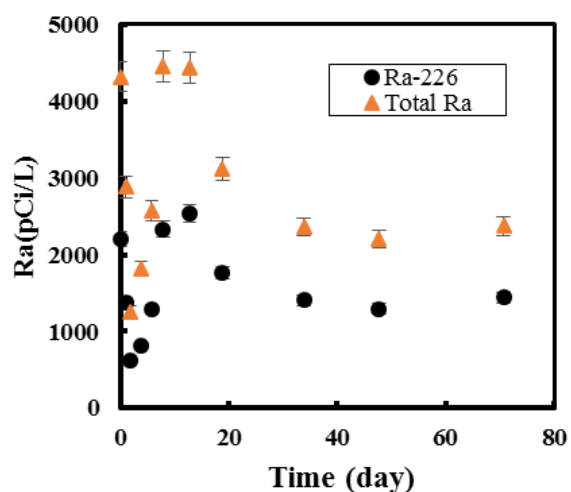


Figure C3: Ra-226 and total Ra activity in 11 Collingwood flowback water samples measured by HP-Ge gamma spectroscopy.

C-4: Secular equilibrium theory

The secular equilibrium is explained by Zhang's book⁷ and summarized here. The two decay chains are shown in Figure C4. Every decay reaction in the decay chain is a first-order reaction. The reaction rate law can be applied to solve for each species in the decay chain. U-238 decay chain is used as an example to solve Ra-226.

$$d^{238}\text{U}/t = -\lambda_{238\text{U}}^{238}\text{U} \quad (\text{C4.1})$$

$$d^{234}\text{Th}/t = \lambda_{238\text{U}}^{238}\text{U} - \lambda_{234\text{Th}}^{234}\text{Th} \quad (\text{C4.2})$$

...

$$d^{226}\text{Ra}/t = \lambda_{230\text{Th}}^{230}\text{Th} - \lambda_{226\text{Ra}}^{226}\text{Ra} \quad (\text{C4.6})$$

The above set of equations (C4.1-C4.6) can be solved to obtain [Ra-226] concentration. However, the progress and the result might be difficult and messy. Another way to solve this is to go step by step. The slowest step is the first step with several orders of magnitude slower. Equation C4.1 can be solved:

$$^{238}\text{U} = ^{238}\text{U}_0 e^{-\lambda_{238}t}$$

The activity of a radioactive nuclide is defined as the decay rate: $A_{^{238}\text{U}} = \lambda_{^{238}\text{U}}^{238}\text{U}$.

$$A_{^{238}\text{U}} = A_{^{238}\text{U}}^0 e^{-\lambda_{238}t}$$

Equation C4.2 can then be solved next:

$$^{234}\text{Th} = ^{234}\text{Th}_0 e^{-\lambda_{234\text{Th}}t} + \frac{\lambda_{238}^{238}\text{U}_0}{\lambda_{234\text{Th}} - \lambda_{238}} (e^{-\lambda_{238}t} - e^{-\lambda_{234}t})$$

Multiplying the above equation by $\lambda_{234\text{Th}}$,

$$A_{\text{Th}} = \left(A_{\text{Th}}^0 - \frac{\lambda_{234\text{Th}}}{\lambda_{234\text{Th}} - \lambda_{238\text{U}}} A_{\text{U}}^0 \right) e^{-\lambda_{234\text{Th}}t} + \frac{\lambda_{234\text{Th}}}{\lambda_{234\text{Th}} - \lambda_{238\text{U}}} A_{\text{U}}$$

$$\lambda_{234\text{Th}} - \lambda_{238\text{U}} \approx \lambda_{234\text{Th}}$$

$$A_{\text{Th}} \approx (A_{\text{Th}}^0 - A_{\text{U}}^0) e^{-\lambda_{234\text{Th}}t} + A_{\text{U}}$$

$$(A_{\text{Th}} - A_{\text{U}}) \approx (A_{\text{Th}}^0 - A_{\text{U}}^0) e^{-\lambda_{234\text{Th}}t}$$

When $\lambda_{234Th} \gg 1$, $A_{Th} \approx A_U$. If the time interval is longer than million years, steady state is then reached: $A_U = A_{Th} = A_{Pa} = A_{Ra} \dots$

The above condition of equal activity of all radioactive nuclides in a decay chain is known as secular equilibrium. The equation C4.7 and C4.8 are then obtained based on the equal activity theory. Equation C4.9, C4.10, and C4.11 are used to calculate Ra-226, Ra-228, and the activity ratio. The activity ratio of Collingwood flowback water and Antrim produced water samples are plotted in Figure C5. The dash line represents the calculated ratio based on equation C4.11.

$$\frac{226_{Ra}}{238U} \approx \frac{\lambda_{238U}}{\lambda_{226Ra}} = \frac{1.55125 \times 10^{-10} \text{ yr}^{-1}}{4.33 \times 10^{-4} \text{ yr}^{-1}} \quad (\text{C4.7})$$

$$\frac{228Ra}{232Th} \approx \frac{\lambda_{232Th}}{\lambda_{228Ra}} = \frac{4.948 \times 10^{-11} \text{ yr}^{-1}}{0.1203 \text{ yr}^{-1}} \quad (\text{C4.8})$$

$$[\text{Ra-226}] = 3.58\text{E-}7 * [\text{U-238}] \quad (\text{C4.9})$$

$$[\text{Ra-228}] = 4.11\text{E-}10 * [\text{Th-232}] \quad (\text{C4.10})$$

$$\frac{228Ra}{226Ra} \text{ activity ratio} = \frac{4.11\text{E-}10 * [232Th]}{3.58\text{E-}7 * [238U]} * 230 \quad (\text{C4.11})$$

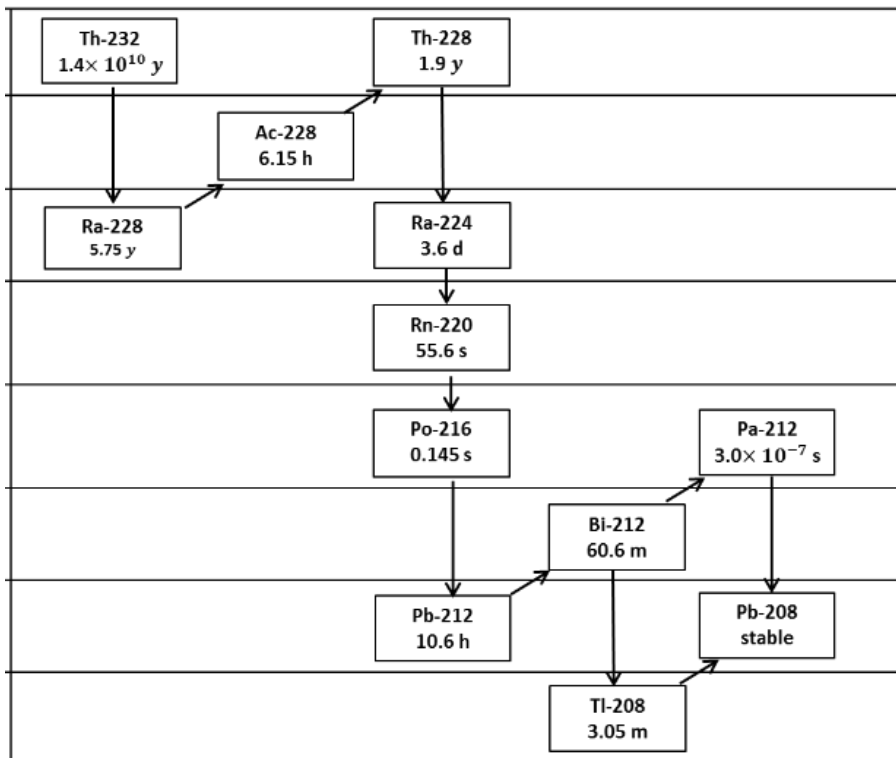
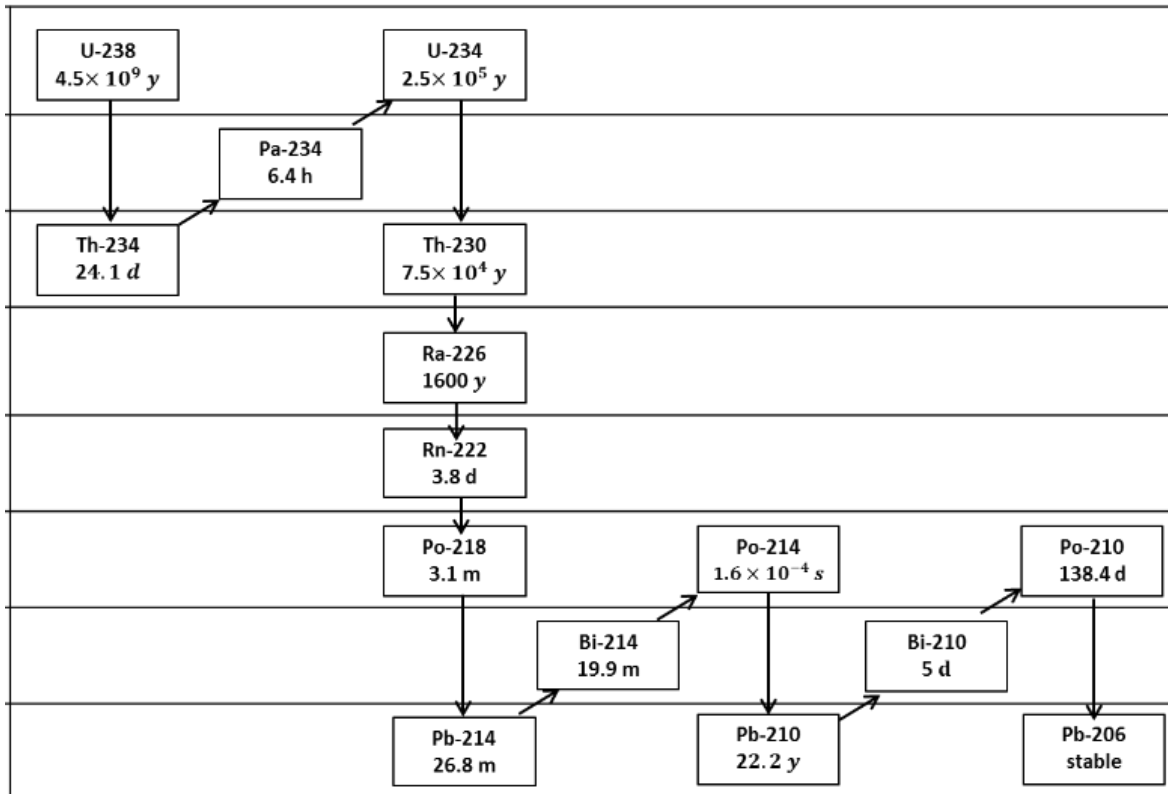
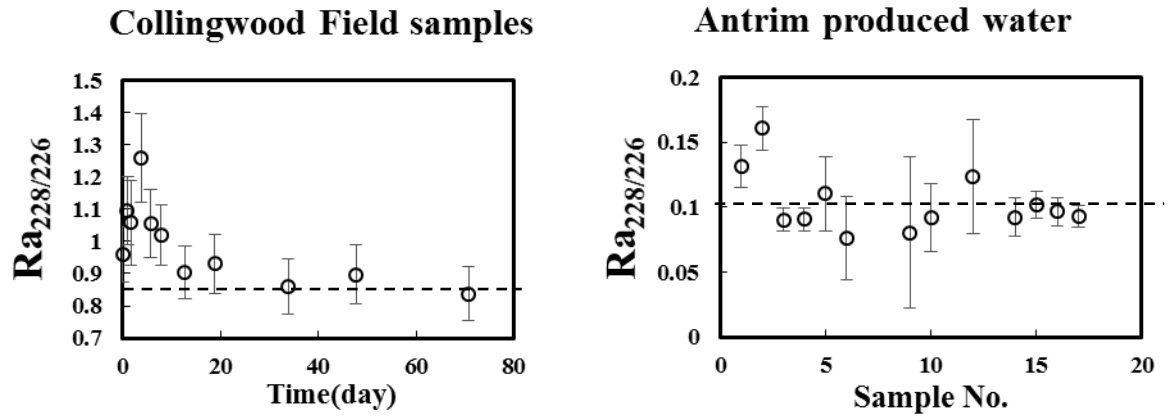


Figure C4: Decay chains of U-238 and Th-232.

Figure C5: Ra-228/Ra-226 activity ratio of Collingwood flowback and Antrim produced water.

The dash line represents the calculated ratio according to U/Th in each reservoir rock.



C-5: Shale XRD analysis results

The following table shows the quantitative XRD analysis results of all four shale samples. Average Marcellus shale sample results are also presented.

Table C3: XRD results of four shale samples in this study

Shale	Mineral (wt.%)	
Utica	Calcite (3%) Ankerite (8%) Illite (38%) Chlorite (8%)	Quartz (19%) Feldspar (19%) Pyrite (2%) Muscovite (3%)
Collingwood	Calcite (44%) Dolomite (5%) Ankerite (4%) Quartz (11%) Feldspar (5%)	Pyrite (1%) Muscovite (2%) Illite (26%) Chlorite (2%)
Antrim	Quartz (30%) Illite (20%) Chlorite (20%)	Feldspar (28%) Pyrite (2%)
Marcellus outcrop	Calcite (55%) Illite (2%) Montmorillonite (18%)	Pyrite (1.5%) Quartz (23.5%)
Marcellus ⁸ (average)	Quartz (20%) Illite-smectite Illite (35%) Pyrite (5%)	Chlorite (7.5%) (7.5%) Calcite (25%)

Table C4: Calculated CEC results.

	Clay type and content	calculated CEC from clay content (meq/100g)	CEC from Ba adsorption experiment (meq/100g)
Antrim	20 - 35% illite, 5 - 10% kaolinite, 0 - 5% chlorite	10	8.9
Average Marcellus ⁸	7.5% chlorite, 7.5% illite-smectite, 35% illite	14	
Marcellus outcrop	2% illite 18% Montmorillonite	11.4	2
Collingwood	2% muscovite, 26% Illite, 2% chlorite	6.5	3.3
Utica	38% illite, 3% muscovite, 8% chlorite	9.5	8.8

Table C5: Measured and reported U, Th, and Ba content, total organic content for shales

	Th (ppm)	U (ppm)	Ba (ppm)	TOC from literature	TOC measured in this study
Antrim	7.4	19.8	241	5-14%, with an average of 8% ^{7,8}	5.3%
Utica	10.5	3.5	322	2.5-6% ^{8,9}	0.5%
Collingwood	4.6	3	139	0.5-1.3% ^{8,9} , 2.215% ^{10,11}	3.4%
Marcellus			1314 ⁵	2-10% ⁶	2.3%

C-6: Antrim produced water analysis

Major anion (sulfate, chloride, barium) concentration and Ra activity are shown in the following table.

Table C6: Antrim produced water analysis

	SO4(ppm)		Cl(ppm)		Ba(ppm)		Ra-226 (pCi/L)		Ra-228 (pCi/L)	
A1	2.29	0.04	7823	221	217	0.2	4054	169.5	528.75	44.04
A2	n.a.		84900	359	124	0.7	5296	218	847.35	55.725
A3	n.a.		115904	42	202	0.5	15800	627.6	1421.5	87.115
A4	n.a.		126630	85	107	1.6	20500	811.4	1857.5	108.81
A5	62.3	0.55	129118	414	8	1.1	1049	53.25	114.25	24.17
A6	1.56	0.25	18382	25	22	0.9	824.8	45.04	61.465	23.33
A7	n.a.		561	2.2	0.22	1.2	37.4	14.81	\	
A8	4.36	0.39	4385	24	3	0.7	121	18.87	\	
A9	n.a.		7750	35	5.2	0.6	353	27.83	26.755	18.355
A10	n.a.		21786	156	26	1.5	1077	55.21	97.765	23.325
A11	1.39	0.19	4296	143	1.6	0.9	72	19.16	\	
A12	n.a.		13707	181	11	0.4	527.3	34.03	63.565	18.865
A13	n.a.		7384	65	5	1.9	248.8	24.74	\	
A14	n.a.		20095	300	25	1.3	2841	122.5	259.65	30.905
A15	n.a.		94955	574	41	0.6	9910	397.9	1005.3	62.055
A16	n.a.		89496	218	39	0.4	8102	327.33	779	53.875
A17	n.a.		97089	325	59	1.4	10723	429.83	992.9	52.31

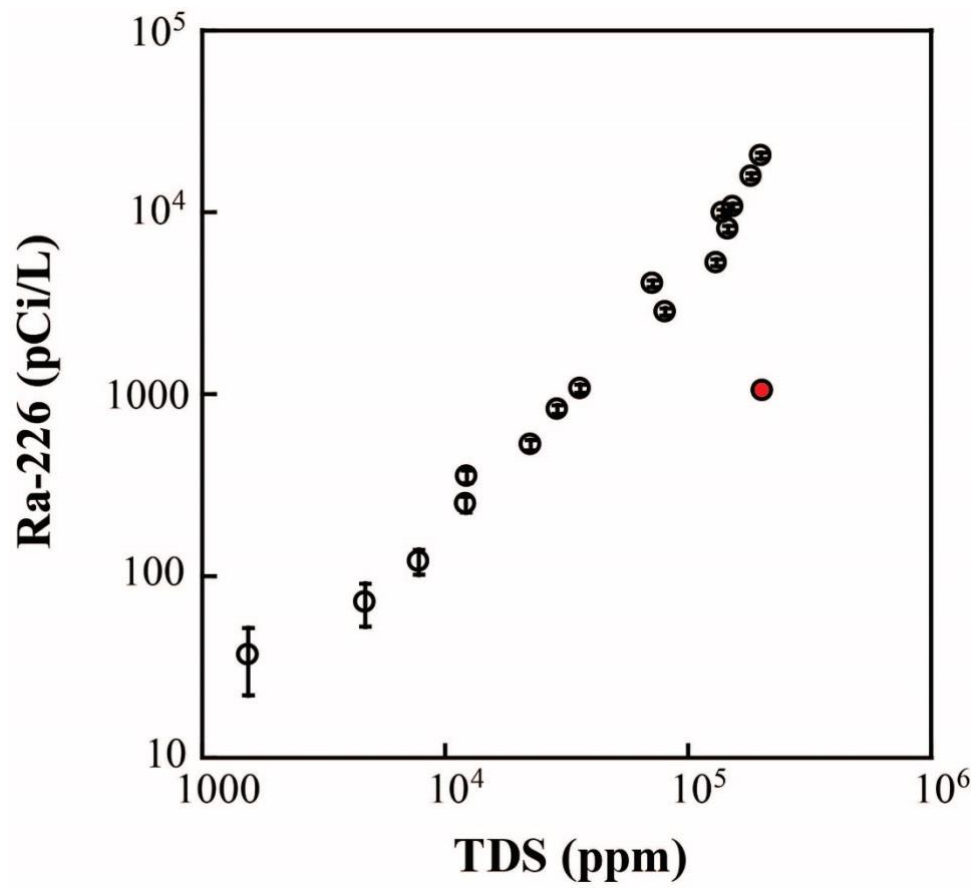


Figure C6: Ra-226 activity vs. TDS for Antrim produced water samples

Reference:

- (1) Nabhani, K. A.; Khan, F.; Yang, M. Technologically Enhanced Naturally Occurring Radioactive Materials in oil and gas production: A silent killer. *Process Saf. Environ. Prot.* **2016**, *99*, 237–247.
- (2) Desbrandes, R. *Encyclopedia of well logging*; Editions OPHRYS, 1985.
- (3) Belknap, W. B.; Dewan, J. T.; Kirkpatrick, C. V.; Mott, W. E.; Pearson, A. J.; Rabson, W. R. API Calibration Facility for Nuclear Logs; American Petroleum Institute, 1959.
- (4) Dewan, J. T. *Essentials of modern open-hole log interpretation*; PennWell Books, 1983.
- (5) Bank, T. L. Trace Metal Geochemistry and Mobility in the Marcellus Shale, 2013.
- (6) Bruner, K. R. *A comparative study of the Mississippian Barnett shale, Fort Worth basin, and Devonian Marcellus shale, Appalachian basin*; 2011.
- (7) Zhang, Y. *Geochemical Kinetics*; Princeton University Press, 2008.
- (8) Hosterman, J. W.; Whitlow, S. I. *Clay mineralogy of Devonian shales in the Appalachian Basin*; Professional Paper; USGS Numbered Series 1298; 1983.
- (9) Ruotsala, A. P. *Mineralogy of Antrim Shale, Michigan*; FE-2346-79; Dow Chemical Co., Midland, MI (USA), 1980.
- (10) William B. Harrison, III. The Collingwood/Utica Shale in Michigan.
- (11) Banas, R. M. *A geophysical and geological analysis of the Collingwood Member of the Trenton Formation*; Michigan Technological University, 2011.